

THE STARBURST-AGN CONNECTION. II. THE NATURE OF LUMINOUS INFRARED GALAXIES AS REVEALED BY VLBI, VLA, INFRARED, AND OPTICAL OBSERVATIONS¹

HARDING E. SMITH²

Center for Astrophysics and Space Sciences and Department of Physics, University of California at San Diego, La Jolla, CA 92093-0424; hsmith@ucsd.edu

COLIN J. LONSDALE

Haystack Observatory, Massachusetts Institute of Technology, Route 40, Westford, MA 01886; cjl@wells.haystack.edu

AND

CAROL J. LONSDALE

Infrared Processing and Analysis Center, California Institute of Technology, 100-22 Pasadena, CA 91125; cjl@ipac.caltech.edu

Received 1997 March 24; accepted 1997 August 13

ABSTRACT

We present here detailed results of an 18 cm VLBI survey of 31 luminous ($L_{\text{FIR}} > 10^{11.25} L_{\odot}$), radio-compact ($\theta \lesssim 0''.25$) infrared galaxies (LIGs). High-resolution VLA maps at 15 and 22 GHz are presented for 14 of these galaxies that exhibit compact milliarcsecond-scale emission, providing information about radio structure of LIGs on scales from $0''.004$ to $1''.0$. We also present new optical spectrophotometric observations. Over half the sample galaxies show high brightness temperature radio emission from the VLBI data, with $T_b > 10^5$ K and structure on scales of 5–150 mas, as previously reported in Lonsdale, Smith, & Lonsdale. The median VLBI power for detected sources is $\log P_{\text{VLBI}} = 22.0$ (W Hz⁻¹), and the mean ratio of VLBI to total 1.6 GHz flux density is $\langle S_{\text{VLBI}}/S_{\text{total}} \rangle = 0.12$. Further structure is observed on the larger VLA scales. No highly significant ($P < 1\%$) statistical correlations are found between the presence or strength of the VLBI emission and other observed quantities, including total radio power, radio spectral index, IR luminosity and colors, radio-infrared ratio, molecular gas mass, and optical excitation. Statistical analysis does suggest that the infrared luminosity, molecular gas emission, and radio emission on VLA and VLBI scales are physically related.

Previous work (Lonsdale, Smith, & Lonsdale) demonstrated that hidden (dust-enshrouded) active galactic nuclei (AGNs) are *capable* of powering LIGs and giving rise to the observed VLBI- and VLA-scale structures; here we investigate the complementary question of whether a starburst can completely explain the observed characteristics, including the high brightness temperature radio emission. Simple starburst models show that the far-infrared luminosity can be explained by starbursts in all cases except Mrk 231, although for some objects the constraints imposed on the initial mass function are severe. Using our starburst models we model the VLBI data for 11 galaxies with detailed radio structural information using complexes of radio supernovae. The required supernova rates are $v_{\text{sn}} \sim 0.1\text{--}2$ yr⁻¹, consistent with the rates derived from the starburst model to explain the observed far-infrared luminosities. However *in all cases* we require complexes of extremely luminous radio supernovae (RSNs) to explain the high- T_b emission. In some cases the RSN must have implausibly high radio powers, more than an order of magnitude larger than any previously reported RSNs; in our view these sources represent AGN radio cores. In most cases an acceptable fit requires that the RSN be clustered on parsec scales. Furthermore, only a few clumps may be active in the radio at a given time. Based on this analysis we conclude that 7/11 systems can be plausibly explained as starbursts. Four galaxies, UGC 2369, Mrk 231, UGC 5101, and NGC 7469, almost certainly house AGN radio cores. From our modeling, coupled with other recent VLBI and infrared evidence, we conclude that Arp 220 is dominated by a massive starburst at radio and infrared wavelengths.

Subject headings: galaxies: active — galaxies: starburst — radio continuum: galaxies

1. INTRODUCTION

Luminous infrared galaxies (LIGs) are characterized by extreme luminosities ($L \gtrsim 10^{11} L_{\odot}$) at mid- to far-infrared (FIR) wavelengths. Typically the far-infrared luminosity of LIGs exceeds the UV-optical radiation by an order of magnitude or more. At the most luminous end of the luminosity function ($L_{\text{FIR}} \gtrsim 10^{12} L_{\odot}$, $H = 75$ km s⁻¹ Mpc⁻¹), LIGs

may be the dominant galaxy population, outnumbering UV/optically selected and radio-selected QSOs (Soifer et al. 1989). In the most luminous LIGs the activity is highly concentrated toward the central few hundred parsecs, as shown by high-resolution VLA mapping in the radio continuum (Condon et al. 1991, hereafter CHYT), and high-resolution molecular line studies that show extremely high nuclear column densities, reaching $N_{\text{H}} = 10^{24}$ cm⁻² for Arp 220 (Scoville et al. 1991). A large fraction of LIGs are interacting or merger systems, and the fraction increases with luminosity (Sanders et al. 1988). At the highest luminosities essentially all LIGs are involved in advanced merger episodes. There is a consensus that LIGs are undergoing tran-

¹ Based on data obtained at the VLA of the National Radio Astronomy Observatory, which is operated by Associated Universities, Inc. under contract with the National Science Foundation.

² Also, Infrared Processing and Analysis Center, California Institute of Technology.

sient episodes, triggered when gaseous material is channeled into the central regions by the interaction event to feed either a nuclear starburst, a central compact object, or both (see Sanders & Mirabel 1996 for an excellent review). We seek to understand two fundamental questions:

1. What is the nature of the dominant energy source in LIGs?
2. What is the relationship between active galactic nucleus (AGN) and starburst activity in those systems in which the two phenomena coexist?

CHYT and others have argued that the FIR luminosity and the radio-continuum properties of these galaxies can be explained by very compact nuclear starburst events. Sanders et al. (1988), on the other hand, have concluded that LIGs are likely to be harboring dust-enshrouded AGNs that are responsible for their far-infrared emission, based on the similar space densities of LIGs and AGNs, and the fact that there is a trend amongst LIGs that the most luminous show the strongest evidence for AGN activity in their optical spectroscopic characteristics. Sanders et al. (1988) proposed an evolutionary sequence in which LIGs will evolve into optically dominated AGNs when the central concentration of dusty molecular material is blown away by the developing compact object, and attributed the FIR emission to a warped disk. Another possibility is that in the currently popular AGN unification models featuring a thick molecular torus, LIGs are the same population as FIR-luminous optically selected AGNs but viewed edge-on to the disk so that the active nucleus is obscured, and the FIR emission is due to a centrally heated torus (Pier & Krolik 1992, 1993; Granato & Danese 1994; Granato, Danese, & Franceschini 1996). In the model of Rowan-Robinson (1995) LIGs are composite objects in which a nuclear starburst is responsible for the longer wavelength ($\lambda \gtrsim 30 \mu\text{m}$) emission, and in 10%–20% of LIGs an AGN is also present and is responsible for additional midinfrared (10–30 μm) emission.

Lonsdale, Lonsdale, & Smith (1992, hereafter LLS92) and Lonsdale, Smith, & Lonsdale (1993, hereafter Paper I), have addressed the question of what fraction of LIGs possess a possible dust-obscured classical AGNs using centimeter-wavelength radio-continuum observations with global very long baseline arrays to penetrate the shroud of dust surrounding the nuclear energy source and to scrutinize them with milliarcsecond resolution. Given the large columns of dense material found in these galaxies ($N_{\text{H}} = 10^{21}\text{--}10^{24} \text{ cm}^{-2}$), only long-wavelength radio or hard X-ray photons may penetrate the material along the line of sight. Although the radio emission from these LIGs is a small fraction of the bolometric luminosity, and our VLBI detections are in most cases less than about 10% of the radio flux density, this emission represents a unique tracer of the physical processes in these compact, highly obscured nuclei; the detection of high brightness temperature, milliarcsecond VLBI emission was considered strong evidence for the presence of a classical AGN. In a pilot 18 cm VLBI search (LLS92) the efficacy of this technique was demonstrated in the detection of milliarcsecond-scale VLBI emission in $\frac{3}{5}$ infrared-bright galaxies, including the peculiar compact radio source Mrk 297A. This source provided a caution for interpretation of compact, high- T_b emission as it may represent the extreme member of a new class of exceptionally luminous radio supernovae (Yin & Heeschen 1991; LLS92; Wilkinson & de

Bruyn 1990), which may be common in starburst galaxies and may mimic the radio properties of low-power AGN radio cores.

In 1991 September we employed a global VLBI array at 18 cm to survey 31 compact, luminous $\log L_{\text{FIR}} \gtrsim 11.25$ (L_{\odot}) infrared galaxies from the IRAS bright galaxy sample (BGS; Soifer et al. 1989) that comprise part of a complete sample of 40 luminous IR galaxies observed at 8.44 GHz with the VLA by CHYT. The detection results from this survey were presented in Paper I; 17/31 galaxies show high brightness temperature emission with $T_b \geq 10^6$ K, which according to our axiom indicates the possible presence of an AGN core. Since this was a detection rather than an imaging experiment, full synthesized maps were not available. Our conclusion was that it is likely that most, possibly all, of the most luminous IR galaxies possess compact high- T_b radio emission. These were interpreted as obscured AGNs with a proviso that in some cases starburst-generated supernovae may be responsible for some or all of high brightness temperature emission.

Norris et al. (1990) have performed a similar experiment, using the Parkes-Tidbinbilla Interferometer (PTI) to survey an equatorial/southern sample of infrared galaxies, concluding that high- T_b cores are present only in high-excitation (Seyfert) infrared galaxies. Their experiment differs from ours in three principal respects: (1) the 275 km baseline of the PTI gives them a principal sensitivity to structure on scales of order 0".1 at 18 cm, whereas the VLBI baselines employed here give us sensitivity to structures down to a few milliarcseconds; (2) our experiment has a lower flux density limit; most of the sources detected in our study would fall below their sensitivity limit; and (3) their sample reaches to much lower FIR luminosity, $\log L_{\text{FIR}} \lesssim 10$ (L_{\odot}), with fewer than a quarter of their systems falling above our lower luminosity cutoff, $\log L_{\text{FIR}} \gtrsim 11.25$ (L_{\odot}). Their somewhat different conclusions can be understood in light of their different sample selection criteria and T_b sensitivity. For three galaxies in common (UGC 2369, NGC 2623, and NGC 7469), both surveys report detections at similar 18 cm flux density.

In a related work (Lonsdale, Smith, & Lonsdale 1995, hereafter LSL95), we posed the question: "If LIGs possess an AGN core, is that AGN capable of powering the observed FIR luminosity?" We compared the bolometric output of LIGs to that of radio-quiet QSOs (RQQs) of comparable radio core power, demonstrating that the milliarcsecond VLBI structures in luminous IR galaxies follow a common relation between compact radio power and bolometric luminosity with radio-quiet AGNs in the Palomar-Green bright quasar sample (BQS; Schmidt & Green 1983). Therefore, if they do possess a buried core, similar to that of RQQs, the obscured QSO is *capable* of generating the observed FIR luminosity. This result neither proves that a hidden QSO *does* provide a significant fraction of the observed far-infrared emission, nor rules out the presence of a starburst. Indeed, the VLBI-detected structure represents only 5%–10% of the total nuclear centimeter radio-continuum emission in LIGs, which is itself a tiny fraction of the bolometric luminosity. The origin of this emission, extended on scales of a few hundred parsecs, would still be uncertain even if the VLBI-scale emission is produced by AGN activity.

One of the most intriguing, and unexpected, results from this effort has been the detection of strong parsec-scale OH

maser emission in Arp 220, the prototype luminous infrared galaxy and megamaser (Lonsdale et al. 1994), implying that the bulk of megamaser emission in Arp 220 originates on scales of order 10 pc. We interpreted the compact OH masers as amplification of the VLBI core by a molecular region in Arp 220 that shares many characteristics in common with the putative molecular torus that distinguishes broad-line from narrow-line AGNs in unified AGN models. The pumping mechanism for the OH molecules has generally been ascribed to the high-FIR (55–120 μm) photon density that would then imply a very compact, luminous central-infrared source, further strengthening the case for the presence of a central engine. However, recent VLBI maser imaging experiments have shown that, while the bulk of maser emission in Arp 220 and III Zw 35 is indeed compact, the emission is concentrated in a series of structures that are spatially unrelated to the compact continuum (Diamond et al. 1989; Baan & Haschick 1996; Lonsdale et al. 1998a; Diamond et al. 1998).

In the present paper we present new high-resolution 15 and 22 GHz VLA A array imaging observations of 14 sources. Our goal is to study the connection between the compact VLBI components and the more diffuse emission seen in the 0".25 resolution studies of CHYT and further elucidate the relative importance of starburst and AGN emission. We also report full details of the VLBI survey observations of 31 luminous IR galaxies presented in Paper I, and combine the high-frequency VLA data with the VLBI data to derive a picture of the radio-continuum structure from 4 mas to 1". We compare the radio-continuum structure and power present on the various sized scales to that expected for a starburst-supernova model and to AGNs. In addition, we present new optical spectrophotometry of sample galaxies that, combined with data from the literature, allow quantitative excitation measures to be obtained for the entire sample. These data are combined with other data from the literature to examine the relationships between the VLBI compact structure and other radio, infrared, and optical characteristics.

In § 2 we describe our LIG sample selection, and in § 3 we describe the new high-resolution VLA observations and provide full details of the 18 cm VLBI sample of Paper I. We also present the available literature data. Section 3.3 describes our new optical spectrophotometry. In § 4 we investigate statistical relationships among VLBI, VLA-scale radio, infrared, and optical characteristics using survival analysis techniques, as appropriate for this censored data set. In § 5 we describe simple model starburst calculations that we employ for further discussion of the radio structure in LIGs. In § 6 we present the starburst and AGN models for the radio-continuum visibility functions. Our conclusions are presented in § 7.

2. THE LUMINOUS IR GALAXY SAMPLE

A complete sample of the 40 most luminous members of the *IRAS* bright galaxy sample (BGS; Soifer et al. 1989) with $S_{60\ \mu\text{m}} > 5.24$ Jy, such that $\log(L_{\text{FIR}}/L_{\odot}) \geq 11.25$, was constructed by CHYT for observation with the VLA A array at 8.4 GHz. The observations were made with angular resolution typically about 0".25 and rms background noise levels of approximately 0.03 mJy. These luminous IR galaxies are, as a class, extremely compact; most of the 8.4 GHz images show nuclear features of angular extent comparable to or smaller than the 0".25 restoring beam. The

extreme compactness implied by the deconvolved sizes calculated by CHYT is of considerable significance to the interpretation of luminous IR galaxies as starbursts. CHYT model these systems as luminous starbursts with thermal dust emission at $T \approx 60\text{--}80$ K that are so dense as to be optically thick to free-free absorption at 1.5 GHz and to dust extinction at 25 μm .

We list the galaxies from the CHYT LIG sample in Table 1. The system name from the catalog that we have deemed to be most common usage is listed in column (1). Columns (2) and (3) list the 1950 radio positions of radio components associated with each system. The positions generally refer to compact 8.4 GHz components detected by CHYT and considered as possible VLBI targets, with the exception of NGC 1614 where the 1.49 GHz position is taken from Condon, Anderson, & Helou (1991a). Note that the individual components for multiple sources are listed not in the conventional R.A. order, but rather in order of estimated maximum VLBI flux density and thus VLBI detectability (see §2.1 below). Columns (4)–(12) list, respectively, the system distance, assuming $H_0 = 75$ km s⁻¹ Mpc⁻¹, the molecular gas mass, M_{H_2} , principally from CO observations by Sanders, Scoville, & Soifer (1991), FIR luminosity, *IRAS* flux densities from Soifer et al. (1989), and 1.5 GHz radio flux density and 1.5–8.4 GHz spectral index from CHYT.

2.1. The VLBI Subsample

Although CHYT were able to resolve nearly all of the nuclear features at 8.4 GHz, deriving deconvolved sizes by assuming elliptical Gaussian brightness distributions, the degree of resolution is typically small, and the data are generally consistent with a large fraction of the flux density in these features originating in regions much smaller than the deconvolved Gaussian sizes quoted. This suggests that the CHYT sample is an ideal sample for investigation with VLBI techniques. In order to estimate the prospects of success and to create a subsample for actual observation, we calculated for each source the maximum possible 18 cm flux density present on scales smaller than 0".05, taking the peak flux density on the published image, frequency corrected from 8.4 to 1.6 GHz using the integrated radio spectral index quoted by CHYT. The resulting value is a strict upper limit, unless the nuclear spectral index is steeper than that of the entire galaxy, a most unlikely circumstance given the nuclear concentration of energy generation and concomitant particle acceleration. If the nuclear spectral index is flatter than the integrated emission, or if there are significant contributions to the peak flux density from extended features, these values will be reduced. In some cases, the presence of significant extended emission in the published image and the fitted component size in Table 2 of CHYT prompted the use of significantly lower values on the basis that extended emission contributes the major part of the peak flux density. These estimated maximum flux densities, $S_{\text{VLBI}}^{\text{max}}$, are listed in column (13) of Table 1.

We compared our derived maximum possible compact 18 cm flux densities to the detection thresholds on the most sensitive VLBI baselines accessible to each source, and included in our sample only those for which the flux density exceeded the detection threshold by at least a factor of 2. The resulting source list comprises 31 sources that are listed in Table 2. The VLBI-detectability criterion is primarily a radio flux density limit because detectable compact structure could not be excluded for any object purely on the

TABLE 1
LUMINOUS FIR GALAXY SAMPLE

SYSTEM (1)	RADIO POSITION (1950)		D (Mpc)	$\log M_{\text{H}_2}^a$ (M_\odot)	$\log L_{\text{FIR}}$ (L_\odot)	IRAS DATA				RADIO DATA		
	α (2)	δ (3)				S_{12} (Jy)	S_{25} (Jy)	S_{60} (Jy)	S_{100} (Jy)	$S_{1.49}$ (mJy)	$\alpha_{1.49}^{8.44}$ (12)	$S_{\text{VLBI}}^{\text{max}}$ (mJy)
Mrk 938	00 08 33.40	-12 23 08.9	77	9.46 ^b	11.28	0.36	2.38	16.08	16.97	58.7	0.78	21.3
IC 1623 ^c	01 05 19.9	-17 46 26	71	10.44	11.39	0.98	3.43	22.19	30.32	211	...	4.7
01076-1707	01 07 41.22	-17 07 07.3	131	10.30 ^d	11.42	0.47	0.88	6.76	10.20	41.9	0.70	1.2
01173+1405	01 17 23.17	+14 05 58.7	124	...	11.54	0.27	1.41	10.72	9.60	43.1	0.70	8.4
01364-1042	01 36 24.27	-10 42 24.3	187	10.18 ^d	11.67	<0.15	0.43	6.53	7.00	17.0	0.42	12.7
III Zw 035	01 41 47.91	+16 51 06.3	109	9.84	11.46	<0.10	1.00	11.86	13.75	39.3	0.40	26.3
NGC 695	01 48 27.85	+22 20 06.9	130	10.34	11.51	0.49	0.81	7.61	13.80	67.6	[0.88]	1.2
UGC 2369	02 51 15.92	+14 46 03.9	124	...	11.42	0.22	1.75	7.68	11.10	42.7	0.67	11.3
03359+1523	03 35 58.33	+15 23 09.4	140	10.37	11.37	<0.12	0.57	5.77	6.53	18.9	0.31	8.8
04191-1855	04 19 06.95	-18 55 41.9	123	...	11.34	0.23	0.55	5.84	10.04	27.3	0.65	14.7
	04 19 07.1	-18 56 00										
NGC 1614 ^e	04 31 35.7	-08 40 57.2	61	10.03	11.39	1.44	7.82	33.12	36.19	107	[1.05]	...
05189-2524	05 18 58.88	-25 24 39.4	166	10.37	11.91	0.74	3.50	13.95	12.52	28.1	0.52	18.9
NGC 2623	08 35 25.27	+25 55 50.2	76	9.77	11.47	0.24	1.85	25.72	27.36	97.8	0.58	31.8
08572+3915	08 57 12.96	+39 15 38.9	236	9.78 ^f	11.96	0.34	1.84	7.66	5.06	6.5	0.27	5.6
UGC 4881	09 12 38.43	+44 32 29.2	163	10.46	11.61	0.16	0.62	6.53	10.21	29.0	0.69	13.8
UGC 5101	09 32 04.78	+61 34 37.0	164	10.32 ^f	11.93	0.26	1.08	13.03	21.25	146	0.59	85.1
10173+0828	10 17 22.26	+08 28 39.7	194	10.35	11.70	<0.11	0.67	6.08	5.97	8.8	0.28	7.7
10566+2448	10 56 36.17	+24 48 39.9	170	10.34	11.90	0.21	1.21	12.53	16.06	46.1	0.68	7.8
11010+4107	11 01 05.81	+41 07 10.5	142	10.18	11.52	0.12	0.37	6.95	10.99	28.0	0.55	13.7
UGC 6436	11 23 08.6	+14 57 06	139	10.26	11.44	<0.13	0.58	5.60	9.80	22.0	(0.82)	3.8
	11 23 13.1	+14 56 37										
Mrk 171 ^g	11 25 44.19	+58 50 18.2	48	10.06	11.74	3.90	24.14	122	122	658	[0.67]	86.2
	11 25 41.53	+58 50 12.4										
12112+0305	12 11 12.48	+03 05 22.1	292	10.62	12.18	<0.14	0.52	8.39	9.10	22.6	0.47	13.5
	12 11 12.37	+03 05 19										
Mrk 231	12 54 05.01	+57 08 38.2	173	10.19	12.35	1.93	8.80	35.40	32.28	240	-0.06	225
Arp 238	13 13 41.83	+62 23 17.9	130	10.13	11.62	0.35	1.96	12.01	12.92	51.2	0.64	8.2
	13 13 37.5	+62 23 35										
13183+3424	13 18 17.01	+34 24 04.7	97	9.87	11.51	0.26	1.37	13.69	24.90	106	0.64	13.3
Mrk 266	13 36 15.01	+48 31 54.1	116	10.15	11.34	0.28	1.13	7.19	10.35	98.8	0.64	11.9
	13 36 14.46	+48 31 45										
	13 36 14.8	+48 31 49										
NGC 5257	13 37 19.6	+01 05 35	95	...	11.37	0.62	1.47	10.68	18.69	47.8	...	1.2
NGC 5258	13 37 19.64	+01 05 23.3										
Mrk 273	13 42 51.71	+56 08 14.3	157	10.24	12.04	0.23	2.30	22.09	22.44	130	0.63	56.5
	13 42 51.76	+56 08 13										
14348-1447	14 34 53.30	-14 47 26.1	326	10.78	12.17	<0.12	0.56	6.46	6.92	33.2	0.71	13.6
UGC 9618	14 54 48.24	+24 49 03.9	140	...	11.58	0.36	0.47	6.68	14.54	68.8	[0.60]	1.9
Mrk 848	15 16 19.30	+42 55 38.3	166	10.27	11.72	0.22	1.40	9.15	10.04	46.8	0.78	14.9
	15 16 19.51	+42 55 31										
15250+3608	15 25 03.72	+36 09 01.0	219	...	11.88	0.12	1.28	7.20	5.78	12.8	0.11	11.6
Arp 220	15 32 46.88	+23 40 07.9	78	10.28	12.11	0.64	7.92	103	114	301	0.41	91.2
	15 32 46.95	+23 40 07										
NGC 6090	16 10 24.58	+52 35 05.4	122	10.15	11.33	0.29	1.22	6.25	9.34	48.3	...	1.2
NGC 6286 ^h	16 57 44.99	+59 00 41.7	80	9.97	11.27	0.50	0.64	9.87	22.01	142	[0.84]	22.7
17132+5313	17 13 13.49	+53 13 49.3	208	10.55	11.79	0.12	0.66	6.35	8.44	28.4	0.67	5.4
22491-1808	22 49 09.09	-18 08 20.6	302	10.43	12.02	<0.09	0.56	5.28	4.58	6.1	0.41	5.1
NGC 7469	23 00 44.41	+08 36 15.8	66	9.96	11.41	1.60	5.84	27.68	34.91	183	0.68	36.3
Zw 475.056	23 13 33.13	+25 17 01.6	111	9.98	11.37	0.32	1.88	8.75	11.64	26.0	0.67	11.3
Mrk 331	23 48 54.03	+20 18 29.2	72	10.11	11.27	0.51	2.56	17.32	20.86	67.5	0.66	20.5

NOTE.—Units of right ascension are hours, minutes, and seconds, and units of declination are degrees, arcminutes, and arcseconds.

^a Molecular hydrogen masses are from CO observations by Sanders et al. 1991.

^b H_2 mass from Chini, Krugel, & Steppe 1992.

^c The companion, IC 1622, 3' SW, accounts for less than 3% of the radio flux density at 1.49 GHz (Condon et al. 1991a) suggesting that IC 1623 dominates the IRAS infrared measures.

^d H_2 mass from Mirabel et al. 1990.

^e Radio position at 1.49 GHz; Condon et al. 1991a.

^f H_2 mass from Solomon et al. 1997.

^g Mrk 171 = NGC 3690/IC 694. Sources D and B from Condon et al. 1991a, corresponding to the nuclei of IC 694 and NGC 3690, respectively.

^h The IRAS position agrees with the position of NGC 6586 from the interacting pair Arp 293 = NGC 6285/6. Surace et al. 1993, have deconvolved the pair at 12, 25, and 60 μm , showing that the bulk of the FIR flux density originates from NGC 6586, as does over 90% of the 1.49 GHz flux density. This source is incorrectly listed as NGC 6285 in Paper I.

TABLE 2
VLBI RESULTS

Source (1)	$S_{1.49}$ (mJy) (2)	$\log P_{1.49}$ (W Hz ⁻¹) (3)	q (4)	S_{VLBI} (mJy) (5)	$\log P_{VLBI}$ (W Hz ⁻¹) (6)	$\log T_b$ (K) (7)
Mrk 938	58.7	22.62	2.52	<2.5	<21.25	5.0 ^a
01173+1405	43.1	22.93	2.46	7.0	22.11	≥7 ^b
01364–1042	17.0	22.85	2.67	<2.0	<21.92	<5
III Zw 035	39.3	22.74	2.57	<1.0	<21.15	5.4 ^a
UGC 2369	42.7	22.89	2.38	15	22.44	≥7 ^b
03359+1523	18.9	22.64	2.58	3.0	21.85	≥7 ^c
04191–1855	27.3	22.69	2.49	<2.5	<21.65	<5
05189–2524	28.1	22.96	2.76	<3.0	<21.99	<5
NGC 2623	97.8	22.83	2.50	9.0	21.79	≥7 ^b
08572+3915	6.5	22.64	3.10	<1.5	<22.00	<5
UGC 4881	29.0	22.96	2.49	4.0	22.10	≥7 ^c
UGC 5101	146	23.66	2.10	28	22.95	≥7 ^b
10173+0828	8.8	22.60	2.91	3.6	22.21	6.1 ^a
11010+4107	28.0	22.83	2.54	<1.5	<21.56	5.1 ^a
Mrk 171D	658	23.25	2.34	1.5	20.61	≥7 ^c
12112+0305	22.6	23.36	2.66	<1.3	<22.12	<5
Mrk 231	240	23.93	2.23	115	23.61	≥7 ^b
Arp 238	51.2	23.01	2.45	<1.5	<21.48	<5
13183+3424	106	23.07	2.28	<0.9	<21.00	<5
Mrk 266	98.8	23.20	1.99	4.5	21.86	6.4 ^c
Mrk 273	130	23.58	2.31	16.0	22.67	≥7 ^b
14348–1447	33.2	23.62	2.37	<2.5	<22.50	<5
Mrk 848	46.8	23.18	2.38	3.5	22.06	7.5 ^c
15250+3608	12.8	22.86	2.80	6.5	22.57	6.2 ^c
Arp 220	301	23.34	2.62	10.5	21.88	≥7 ^b
NGC 6286	142	23.03	2.05	13.0	22.00	7.0 ^b
17132+5313	28.4	23.17	2.46	<1.5	<21.89	<5
22491–1808	6.1	22.85	2.90	<4.0	<22.64	5.2 ^a
NGC 7469	183	22.98	2.29	12.0	21.79	≥7 ^b
Zw 475.056	26.0	22.58	2.64	<0.8	<21.07	<5
Mrk 331	67.5	22.62	2.51	7.5	21.67	≥7 ^b

^a Single baseline detection.
^b Complex structure in visibility plot.
^c Simple structure in visibility plot.

basis of resolved appearance on the CHYT image. It is almost certainly valid to consider systems excluded from the sample as nondetections at the detection threshold used to determine sample membership for that galaxy.

3. OBSERVATIONS

3.1. Eighteen Centimeter VLBI Survey Observations

The VLBI observations were performed on 1991 September 29, under the auspices of the US and European VLBI networks, project code GL5. In addition to the most sensitive antennas available, namely, Effelsberg (Germany), phased VLA (New Mexico), Greenbank (West Virginia), and Arecibo (Puerto Rico), we used the southwestern US VLBA antennas Pietown and Los Alamos (New Mexico), Kitt Peak (Arizona), and Fort Davis (Texas), together with the Westerbork tied array (Netherlands) and the Jodrell Bank MkIA telescope (UK) to provide a number of relatively short baselines. Data reduction has been described previously in Paper I.

In all, 21 sources exhibited significant correlated flux density on one or more baselines, with detection thresholds as low as 1 mJy on the most sensitive baselines. Visibility plots (correlated flux density versus baseline length) were constructed for all sources detected on any baseline(s). The results of our global VLBI survey are graphically illustrated in Figure 1, which shows these visibility plots for the 16 sources with detections on multiple baselines and with implied source brightness temperature in excess of 10⁶ K.

Plotted for reference on each source plot is the expected behavior for a single, Gaussian source with $T_b = 10^5$ K (*solid line*), 10⁶ K (*dashed line*), and 10⁷ K (*dotted line*) at the scale of the appropriate baseline. A single detection along one of the plotted curves sets a lower limit to the source brightness temperature under the assumption that the source is a circularly symmetric Gaussian source. Such a Gaussian source would have an angular size, FWHM = 0.5 times the fringe spacing for the appropriate baseline and a flux density 2.5 times the observed value at that baseline. The expected maximum brightness temperature is $T_b = 10^5$ K, assuming a thermal (H II) bremsstrahlung source with $T_e \approx 10^4$ K contributing 10% of the radio emission and with 90% coming from supernova produced synchrotron plasma (Condon & Yin 1990),

$$T_b(*b) \lesssim T_e \left[1 + 10 \left(\frac{v}{1 \text{ GHz}} \right)^{0.1-\alpha} \right] \lesssim 10^5 \text{ K} . \quad (1)$$

The solid line thus represents a fiducial for sources that merit further scrutiny as possible AGN cores.

The results of the VLBI experiment are summarized in Table 2, which is an updated version of data presented in Paper I. Columns (1) and (2) repeat the source name and 1.49 GHz flux density as given in Table 1. Column (3) gives the 1.49 GHz radio power and column (4) the infrared-to-radio ratio, “ q ” (Condon et al. 1991a). Note that the data in columns (2)–(4) refer to source properties *integrated over the entire system*. Columns (5)–(7) give the VLBI data. Columns

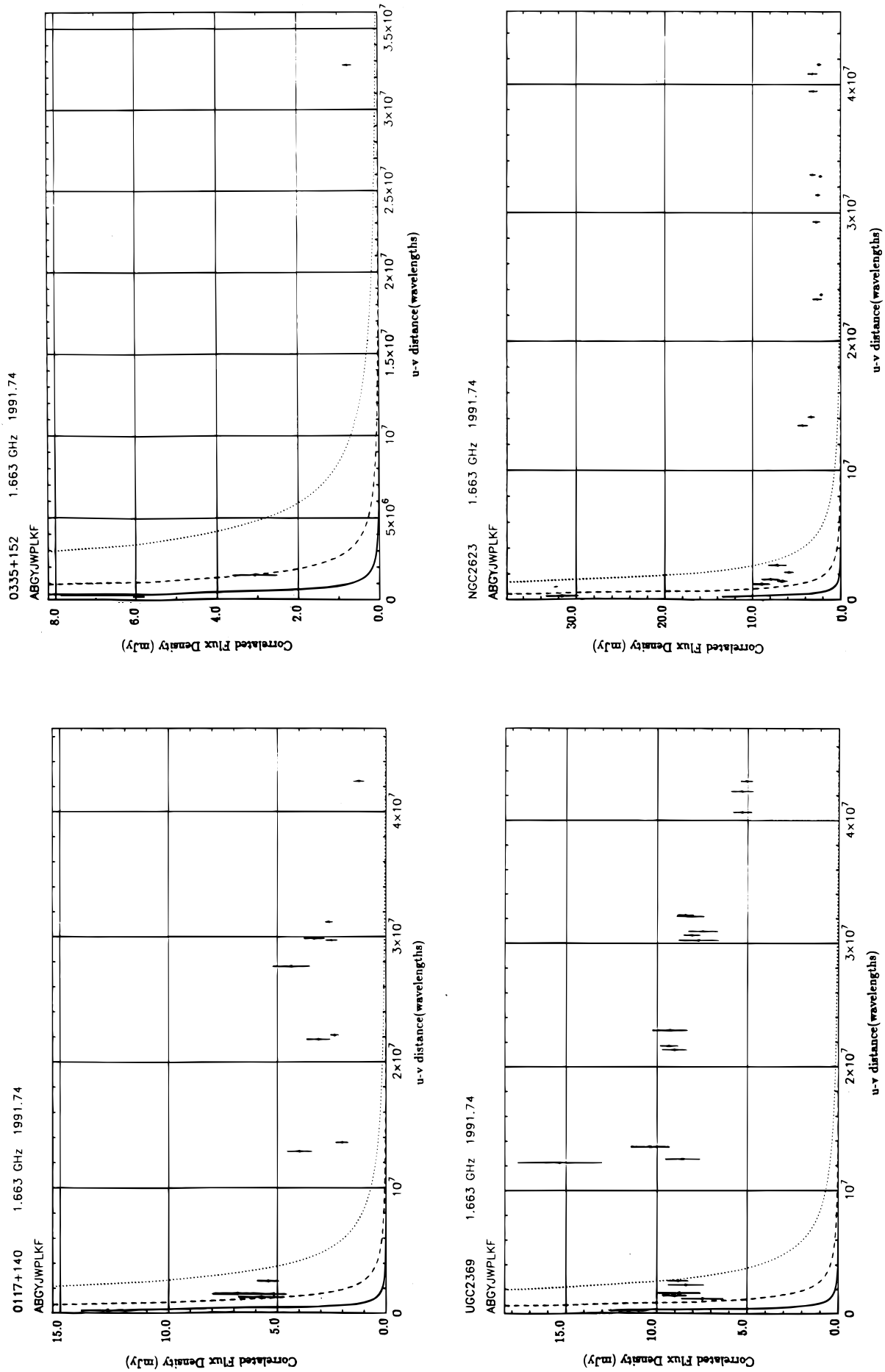


FIG. 1.—Visibility plots for the 16 sources with detections on at least two VLBI baselines and estimated $T_b \gtrsim 10^6$ K. Error bars are 1σ representing a combination of thermal noise and estimated calibration error. The three curves 10^5 K, 10^6 K, and 10^7 K (solid, dashed, and dotted lines, respectively) represent the correlated flux density for a source of the given brightness temperature, assuming a circular Gaussian source shape with FWHM 0.5 times the fringe spacing.

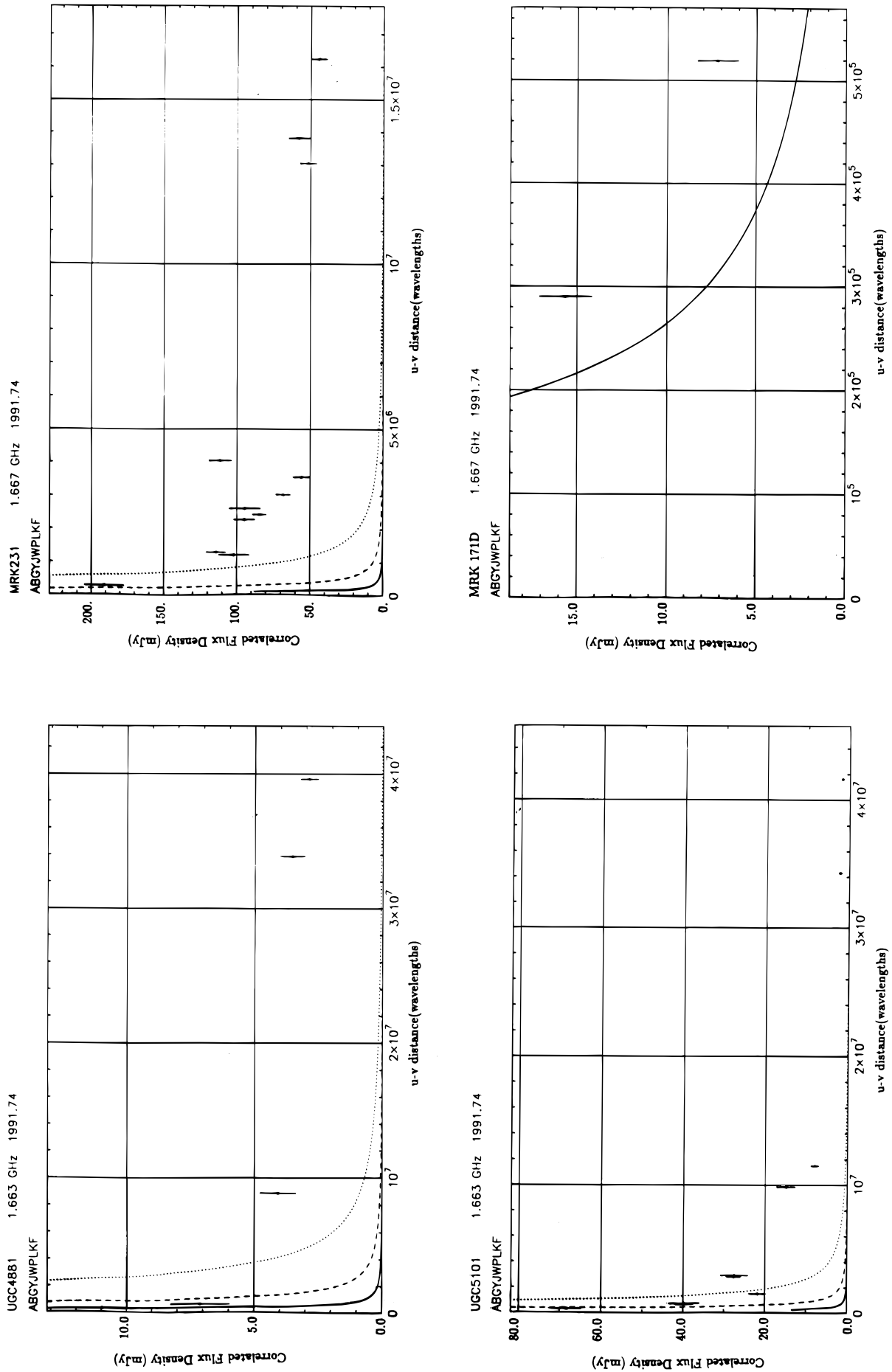


FIG. 1—Continued

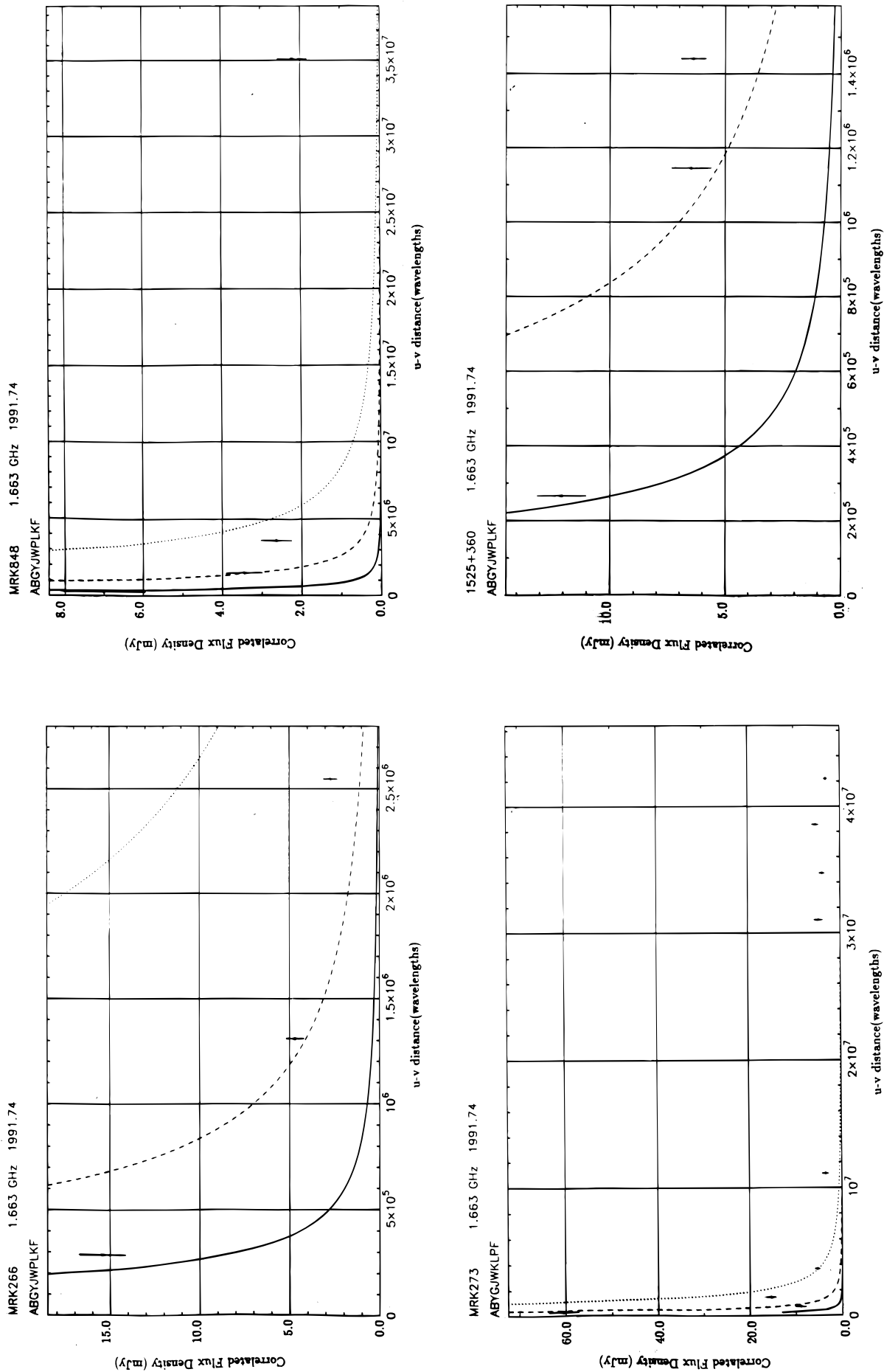


FIG. 1—Continued

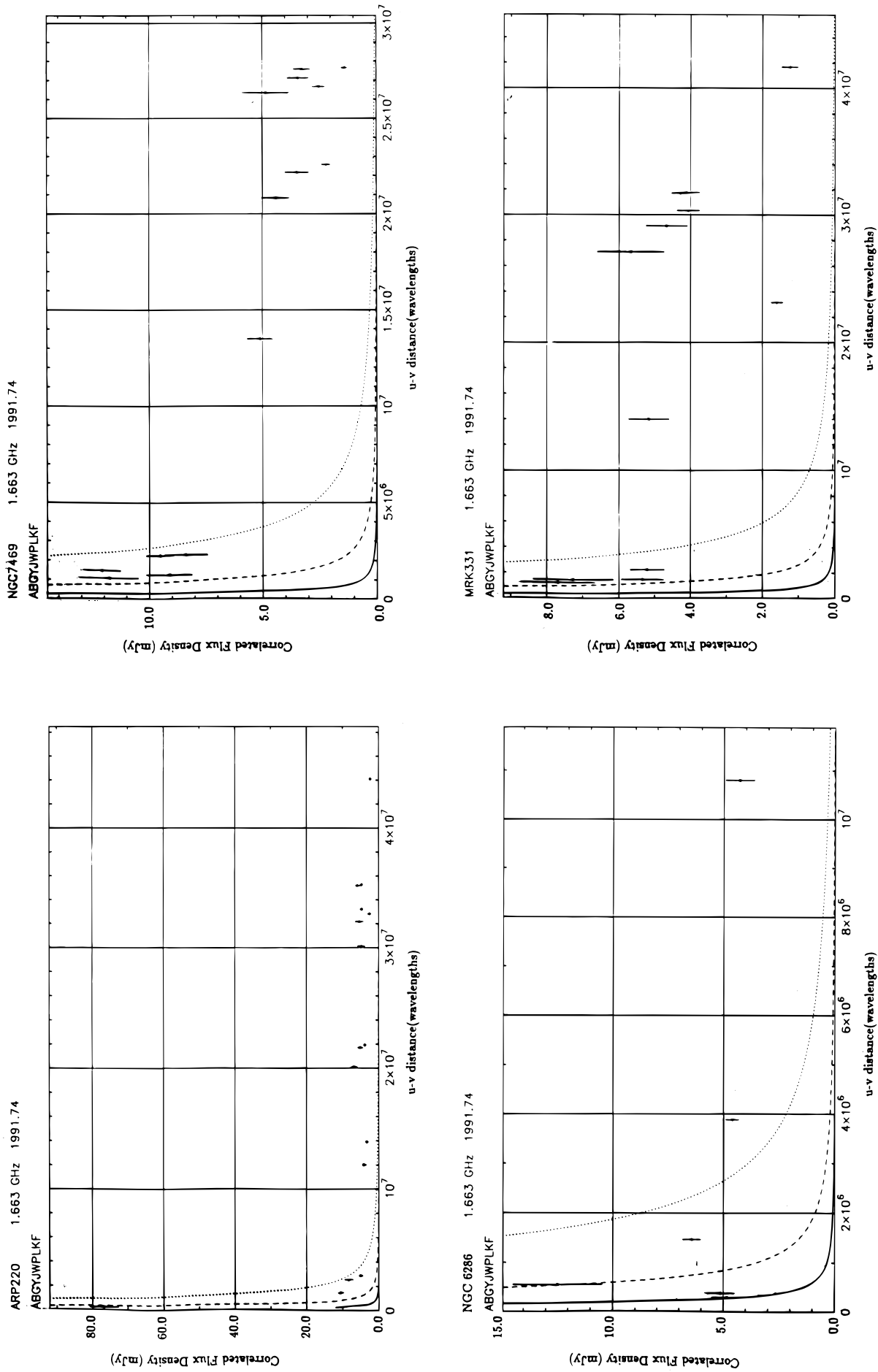


FIG. 1—Continued

(5) and (6) list the maximum correlated flux density and power at 18 cm on baselines of projected length $\geq 10^6 \lambda$. Column (7) provides an estimate of the source brightness temperature, determined by modeling the emission as a circular Gaussian component of angular size approximately 0.5 times the fringe spacing, and flux density 2.5 times the correlated flux density. This is the minimum brightness temperature for a Gaussian component fitting the measurement; in general we cannot rule out regions with T_b significantly higher than quoted. For a few sources the visibility functions are fitted adequately by a single Gaussian component, and we quote the T_b corresponding to this component. For single baseline detections we also quote the T_b for a Gaussian component with the appropriate correlated flux density on the baseline detected. For the current data, meaningful estimates of T_b above about 10^7 K cannot be made, and in cases of substantial correlated flux density on very long baselines we have tabulated $T_b \gg 10^7$ K (note that this does not imply pointlike, unresolved structure).

The median VLBI core power on baselines longer than $10^6 \lambda$ is $\log P_{\text{VLBI}}(\text{median}) = 22.06$ (W Hz^{-1}) for detected sources, with a median ratio of core to total 1.6 GHz radio power of 12%. Figure 2 shows the histograms of the VLBI core power and core fraction *limits* for detected and undetected sources. The two histograms are quite comparable, with median values $\log P_{\text{VLBI}} \lesssim 21.8$ (W Hz^{-1}) and core fraction $\lesssim 6\%$, respectively. We caution that the flux density limits for undetected sources were typically determined on longer baselines than the maximum core flux density measurements for the detected sources. Nonetheless, our results are clearly consistent with the presence of compact high- T_b emission in all of our sample galaxies and in the majority of the CHYT complete sample, at a power level of $\log P_{\text{VLBI}} \gtrsim 20.5$ (W Hz^{-1}), which falls below the typical detection threshold.

All 17 sources with measured S_{VLBI} values listed in Table 2 have detectable compact emission substantially (i.e., more than a factor of 10) in excess of the starburst limit of 10^5 K given by equation (1). Three additional sources showed emission with $5.0 \lesssim \log T_b \lesssim 5.4$, only marginally above this limit. As anticipated from the CHYT images, most sources showed evidence for considerable emission on the shortest baselines (scales of $0''.05$ and greater).

In column (7) of Table 2 we classify the VLBI structure as “simple” or “complex” based upon the visibility functions and closure phase data. Simple sources are those that have monotonically declining or flat visibility curves and are *consistent* with a single, circularly symmetric (e.g., Gaussian) compact source. Complex sources do not appear to have circular symmetry, and the visibility functions suggest the presence of multiple components at the resolution of the observations. Such classification was not possible for all detected sources, owing to the paucity of data. It should be emphasized that future, more extensive observations may detect complex structure for sources classified here as “simple,” and this classification should not be taken as proof of pointlike structure. A designation of “complex” in Table 2, however, precludes the possibility that the detected emission originates in a single pointlike source.

3.2. High-Resolution VLA Observations

In order to probe the structure of the intermediate-scale radio emission and determine its relationship, if any, to the VLBI-scale emission, we used the VLA at its maximum

angular resolution on 16 of the sources that showed 18 cm VLBI-scale emission above a brightness temperature of 10^5 K. Three sources were omitted because they could not be conveniently observed in the scheduled time allocation, and Mrk 231 was omitted on the basis that the bulk of the emission originates in an unresolved core component.

The observations were conducted during a 12 hr period on 1994 March 26 and 27, in the A array of the VLA. Data were taken for each of the 16 target sources at both *K* band (22 GHz) and *U* band (15 GHz). An aggressive strategy for phase calibration, using nearby reference sources for each target, was employed. This involved rapid switching between calibrator and target, with 90 s on the calibrator and 150 s on the target, inclusive of slewing time, for a total cycle time of 4 minutes. The sources were divided into two groups for scheduling, designated strong and weak on the basis of the anticipated correlated flux density, and estimated using the CHYT images and our 18 cm VLBI data with assumed spectral indices. The weak sources were allocated roughly 21 minutes of on-source integration time at *K* band, and 13 minutes at *U* band, compared to 8 minutes and 4 minutes, respectively, for the strong sources. The anticipated final map rms noise levels ranged from 0.15 to 0.5 mJy beam $^{-1}$.

The weather was poor during the observations, with moderate cloud cover and intermittent snow showers. Phase stability was poor during the first hour or so, and snow accumulation in the dishes effectively destroyed the final 90 minutes of the run. The data for two sources, Arp 220 and NGC 6286, were useless. The data were reduced using the NRAO Astronomical Image Processing System (AIPS) software package at Haystack Observatory. Several phase calibration methods and many diagnostics were employed to maximize and measure the quality of the final phase calibration; a simple two-point interpolation scheme using adjacent calibrator scans was found to be optimal. In a few cases, reliable self-calibration of the target source was possible; this allowed us to accurately assess the quality of the external phase calibration in those cases. For most of the sources, the loss of peak intensity due to phase errors is thought to be less than 10% at *U* band and 20% at *K* band, with higher values possible toward the beginning and end of the run. The majority of the images presented here are noise limited, and cases in which there is doubt about the image fidelity are discussed individually. The overall flux density scale was fixed using observations of 3C 286 during the run, in the standard manner. The images were produced using the CLEAN algorithm. In cases where self-calibration was possible, a single cycle of phase-only self-calibration with a short solution interval was employed.

It is evident from these observations, as with the VLBI visibility data, that structure typically exists on a range of size scales. However, owing to generally low-image SNRs, it is impossible to represent the detected structure on the highest spatial scales simultaneously with the lowest surface brightness extended emission. We have therefore chosen to present in Figure 3 the data for each source using an array of four images of decreasing angular resolution, but increasing sensitivity: 22 GHz uniform weighting, 22 GHz natural weighting, 15 GHz uniform weighting, and 15 GHz natural or tapered. For each source we also present the VLA restoring beam and the FWHM ellipse of the deconvolved Gaussian fitted by CHYT for that source to indicate graphically the extent of the substructure detected in our higher

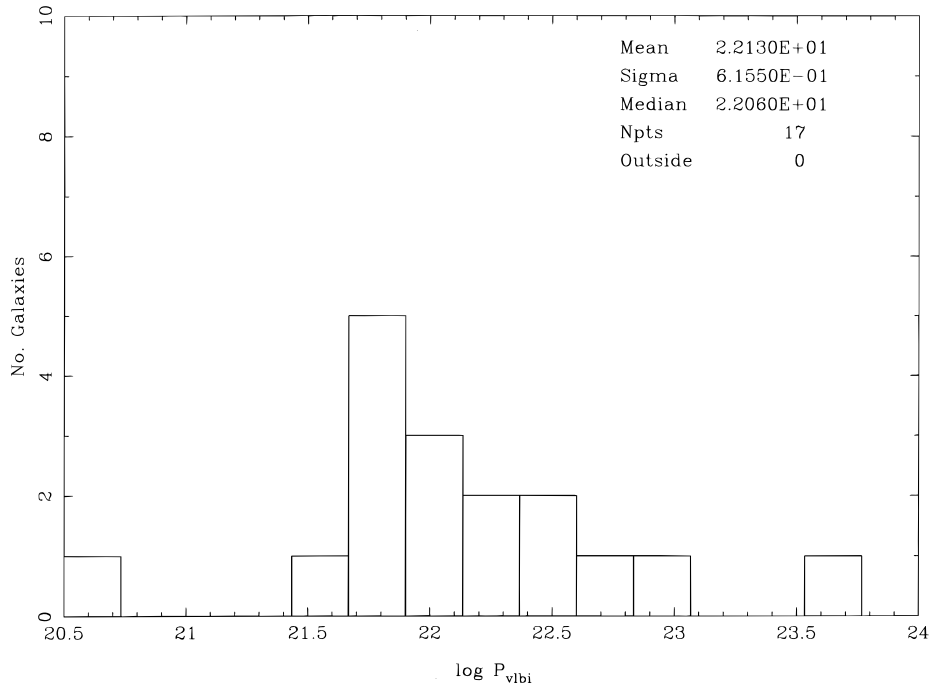


FIG. 2a

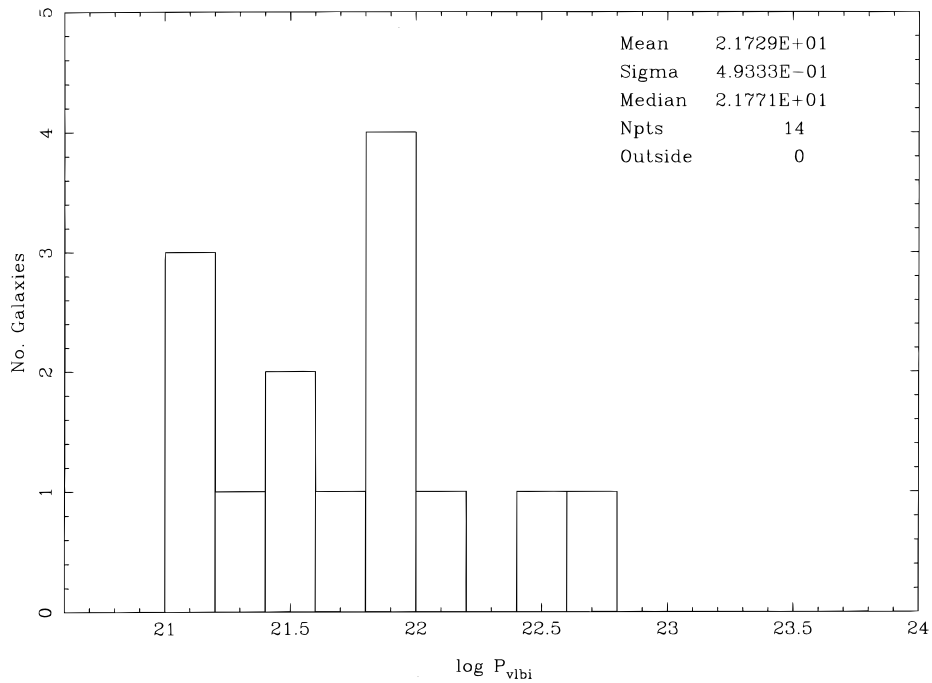


FIG. 2b

FIG. 2.—Histograms of VLBI power and VLBI fraction ($P_{\text{VLBI}}/P_{1.49}$) for the 17 detected and 14 nondetected galaxies in our LIG sample. (a, b) VLBI power histograms for the detections and upper limits, respectively. (c, d) VLBI fraction histograms.

resolution observations.

3.3. Optical Spectrophotometry

New optical observations for several of our sample galaxies that have no previously published quantitative optical spectrophotometry were obtained in 1992 and 1993 using the Kast double CCD spectrograph on the 3 m Shane telescope of UC's Lick Observatory. The optical data were reduced using the NOAO IRAF reduction package at the Infrared Processing and Analysis Center (IPAC). The

spectra were extracted using IRAF's optimal extraction procedure with windows typically $7''$ – $10''$ perpendicular to the dispersion. Sky was taken well away from the galaxy nucleus, typically further than $15''$, but in most cases may still contain some residual emission. The wavelength calibration was initially performed using calibration lamp observations from the beginning and/or end of the night, but the individual spectra were recalibrated using the extracted night sky spectrum for each object, resulting in a wavelength accuracy of approximately 0.5 \AA . A variety of

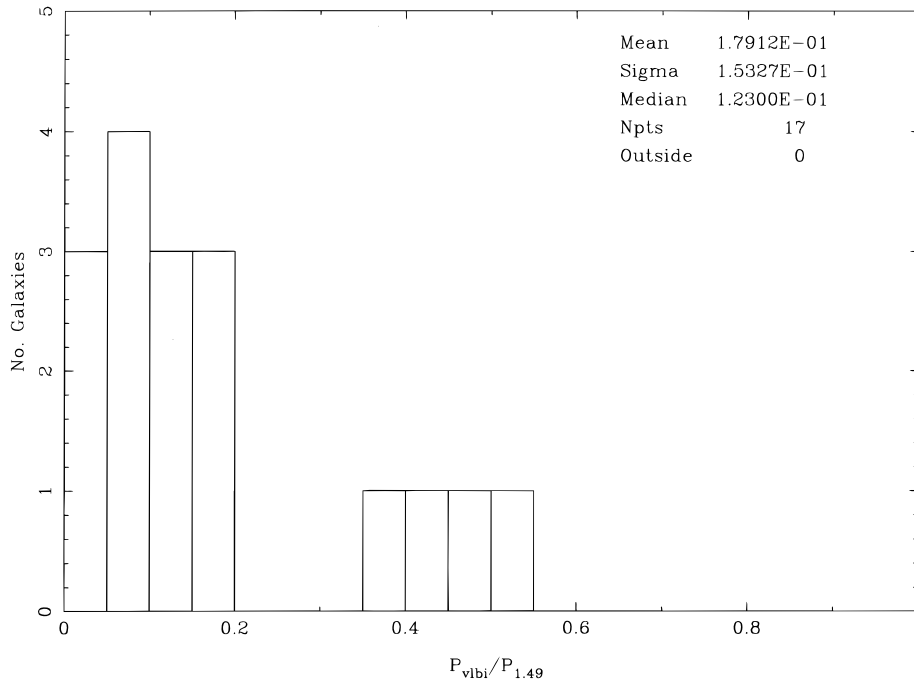


FIG. 2c

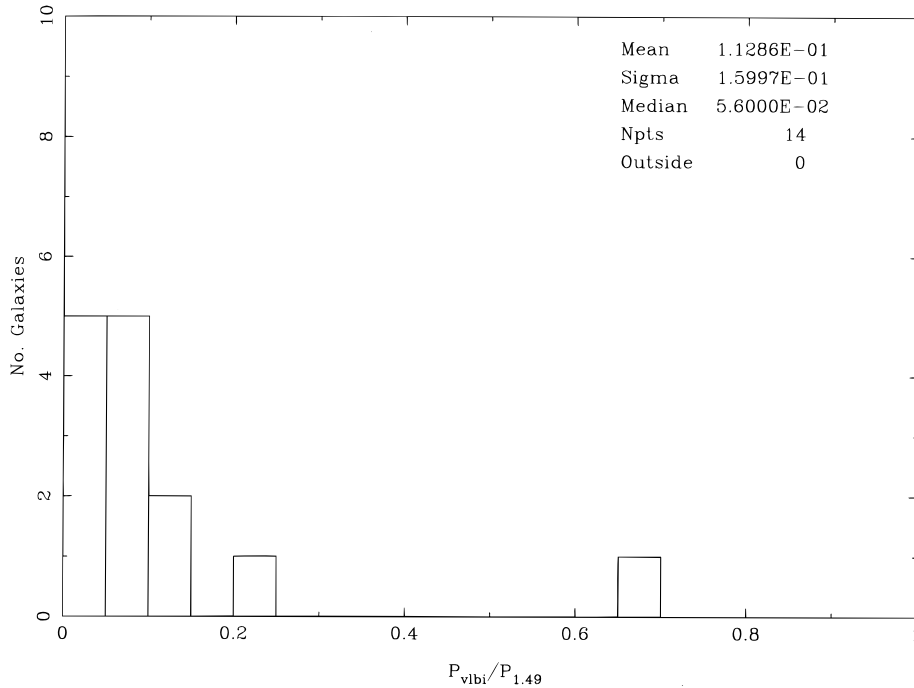
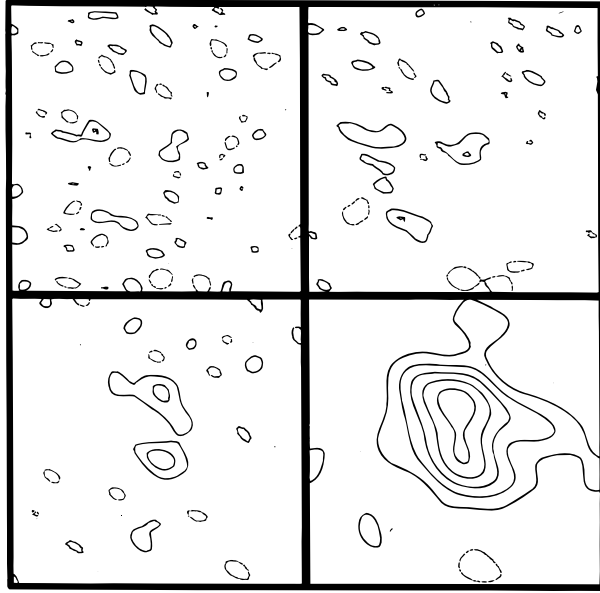


FIG. 2d

IRAF procedures were used to estimate line fluxes; blended features were separated using IRAF's Gaussian spectral fitting routine. Except where noted, uncertainties in the relative line fluxes are estimated to be about 10%.

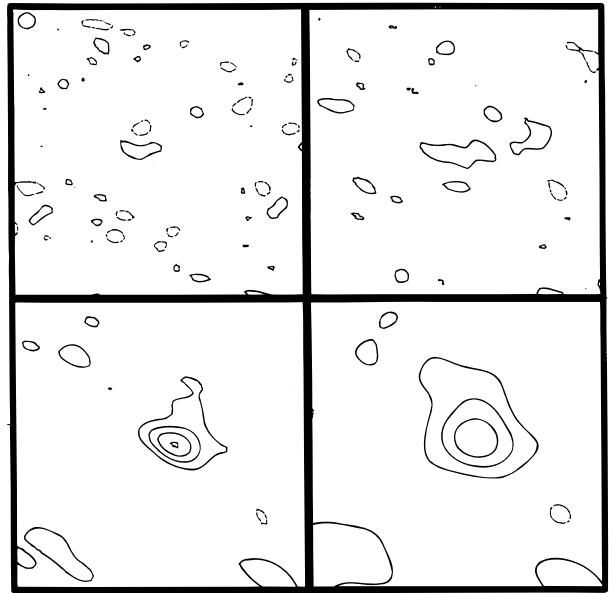
Veilleux et al. (1995) have recently published an extensive spectrophotometric survey of luminous and warm *IRAS* galaxies, which contains many of the systems in our sample. Along with previously published data from Armus, Heckman, & Miley (1989), we now have high-quality quantitative measures for all but one system in the LIG sample. In Table 3 we list the red ($\lambda \approx 4800\text{--}7200 \text{ \AA}$) spectro-

photometric data for our sample galaxies in terms of reddening corrected ratios of the principal excitation-sensitive features: $[\text{O III}] \lambda 5007/\text{H}\beta$, $[\text{N II}] \lambda 6583/\text{H}\alpha$, $[\text{S II}] \lambda 6717 + \lambda 6730/\text{H}\alpha$, and $[\text{O I}] \lambda 6300/\text{H}\alpha$. We include in Table 3 the data from Veilleux et al. (1995) and from Armus, Heckman, & Miley (1989) for comparison. Extinction corrections for all three data sets were made using the observed Balmer decrement with the standard (Galactic) extinction curve (Savage & Mathis 1979). We did not attempt absolute spectrophotometry so that $\text{H}\alpha$ luminosities are entirely from wide-slit spectrophotometry by Veilleux et al. (1995)



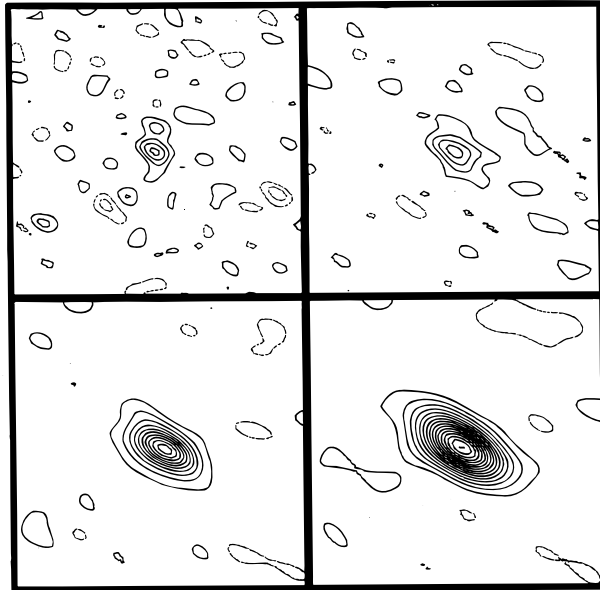
22GHz Uniform 122 x 86, 66° C.I. 0.8mJy	22GHz Natural 177 x 105, 60° C.I. 0.5mJy
15GHz Uniform 199 x 117, 61° C.I. 0.5mJy	15GHz Tapered 349 x 249, 60° C.I. 0.3mJy

0117+140
Field center at:
01^h 17^m 23^s.170, +14° 05' 58".68



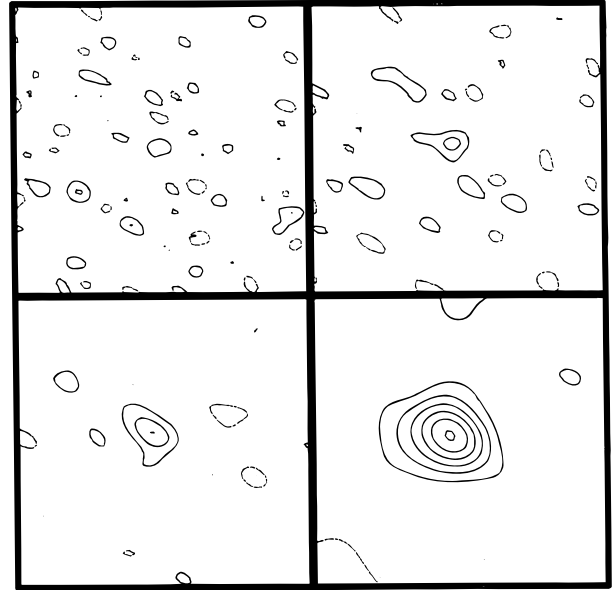
22GHz Uniform 111 x 86, 67° C.I. 1.0mJy	22GHz Natural 159 x 106, 60° C.I. 0.6mJy
15GHz Natural 259 x 147, 59° C.I. 0.4mJy	15GHz Tapered 340 x 249, 60° C.I. 0.4mJy

UGC 2369
Field center at:
02^h 51^m 15^s.938, +14° 46' 04".00



22GHz Uniform 137 x 89, 65° C.I. 1.0mJy	22GHz Natural 184 x 105, 62° C.I. 0.8mJy
15GHz Uniform 245 x 117, 62° C.I. 0.7mJy	15GHz Natural 300 x 143, 61° C.I. 0.5mJy

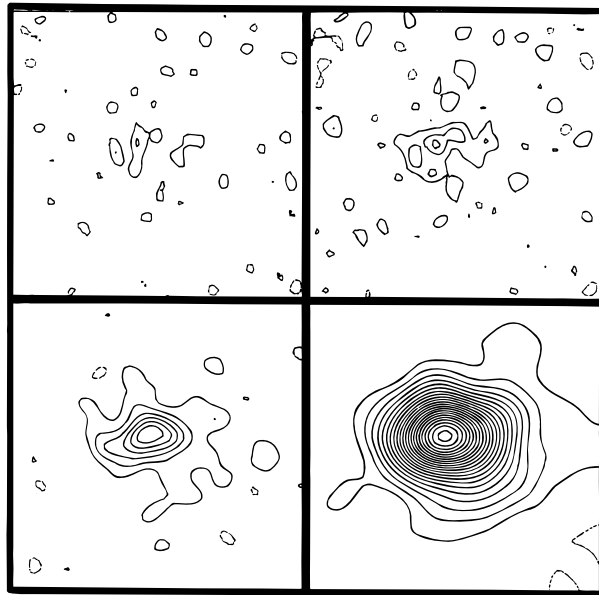
III Zw 035
Field center at:
01^h 41^m 47^s.920, +16° 51' 06".28



22GHz Uniform 120 x 85, 66° C.I. 0.8mJy	22GHz Natural 169 x 105, 61° C.I. 0.5mJy
15GHz Uniform 197 x 114, 62° C.I. 0.7mJy	15GHz Tapered 353 x 248, 60° C.I. 0.4mJy

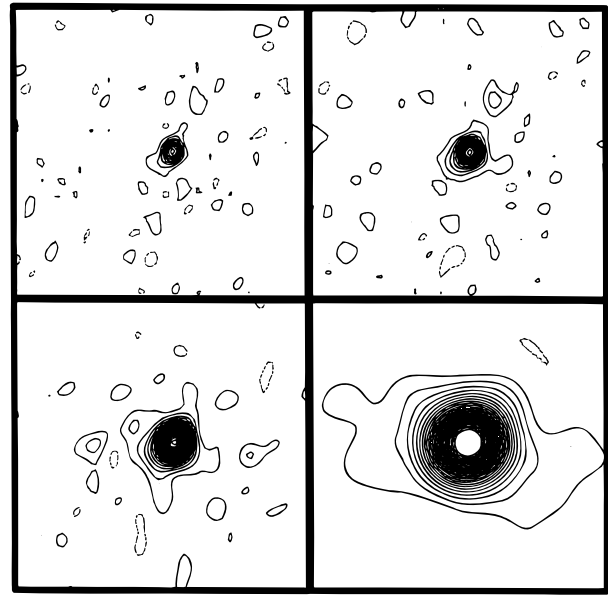
0335+152
Field center at:
03^h 35^m 58^s.334, +15° 23' 09".38

FIG. 3.—Images from the A Array of the VLA at 22 GHz and 15 GHz for 14 luminous infrared galaxies. Each source is displayed in four panels with varying angular resolution and sensitivity resulting from differing $u-v$ weighting methods. Each panel is $1''.4$ on a side. Below each set of four panels is a set of minipanel, in each of which are listed the key parameters of the corresponding image. On the first line, a K indicates 22 GHz, and U indicates 15 GHz. The $u-v$ plane weighting method used is uniform (highest resolution, inferior sensitivity), natural (lower resolution, maximum sensitivity), and tapered (much lower resolution, better surface brightness sensitivity). The restoring beam size in milliarcseconds and the position angle of its major axis are given on the next line, and on the last line the contour interval is given in megajanskys. The B1950.0 coordinates of the field center are given to the right of the minipanel. Also to the right of the minipanel are two ellipses. The open ellipse is the FWHM of the CHYT restoring beam for that source, and the solid ellipse is the deconvolved size derived by CHYT, with position angle estimated from the 8.4 GHz images, both on the same angular scale as our K and U band images. This is intended to provide a point of reference for assessing the substructure revealed by our images.



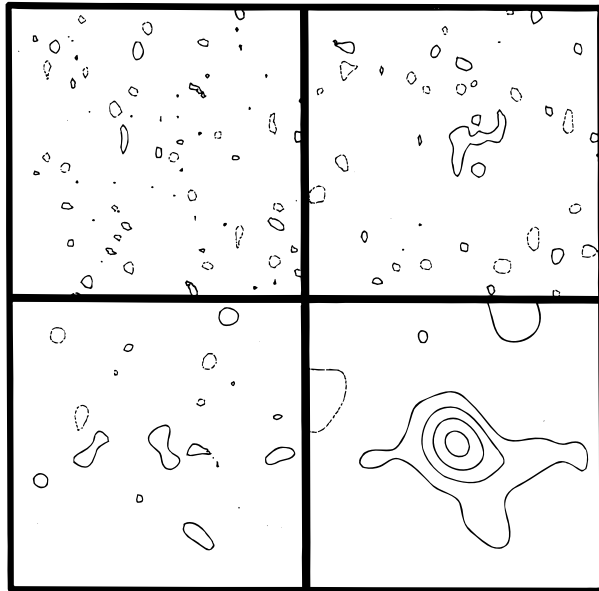
22GHz Uniform 85 x 72, 1° C.I. 1.0mJy	22GHz Natural 103 x 88, -7° C.I. 0.7mJy
15GHz Uniform 125 x 119, 8° C.I. 0.6mJy	15GHz Tapered 267 x 257, -57° C.I. 0.4mJy

NGC 2623
Field center at:
08^h 35^m 25^s.270, +25° 55' 50".18



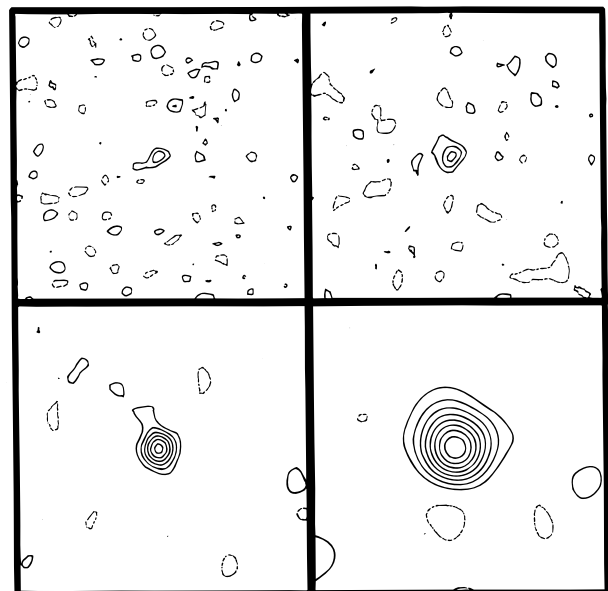
22GHz Uniform 93 x 69, -7° C.I. 1.0mJy	22GHz Natural 111 x 88, -9° C.I. 0.7mJy
15GHz Uniform 141 x 113, -14° C.I. 0.7mJy	15GHz Tapered 272 x 259, -32° C.I. 0.7mJy

UGC 5101
Field center at:
09^h 32^m 04^s.780, +61° 34' 36".90



22GHz Uniform 77 x 67, 0° C.I. 0.8mJy	22GHz Natural 100 x 87, -11° C.I. 0.5mJy
15GHz Uniform 118 x 104, -6° C.I. 0.6mJy	15GHz Tapered 267 x 258, -54° C.I. 0.4mJy

UGC 4881
Field center at:
09^h 12^m 38^s.430, +44° 32' 29".18



22GHz Uniform 80 x 74, -26° C.I. 0.8mJy	22GHz Natural 110 x 89, -2° C.I. 0.5mJy
15GHz Uniform 125 x 114, -18° C.I. 0.5mJy	15GHz Tapered 268 x 258, -13° C.I. 0.4mJy

1017+082
Field center at:
10^h 17^m 22^s.257, +08° 28' 39".64

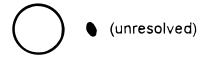
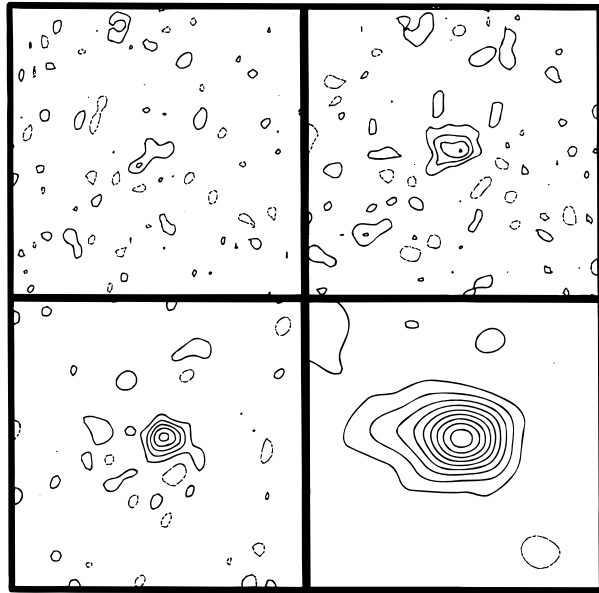


FIG. 3—Continued

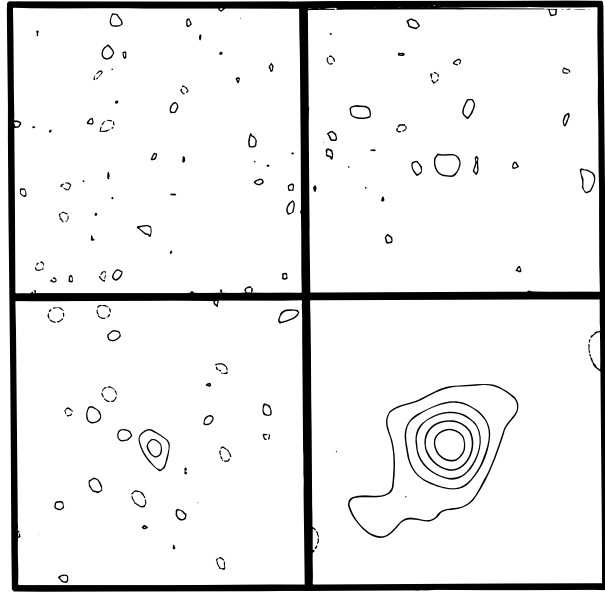
or Armus, Heckman, & Miley (1989), as noted in the table. No correction is made for emission falling outside the slit; thus these are *nuclear* line ratios and luminosities, excluding contribution from extended star formation in the LIG disks.

The emission-line ratios have been used to calculate optical spectroscopic excitation values following the scheme first suggested by Baldwin, Phillips, & Terlevich (1981). In Figure 4, we plot the excitation of the sample members from



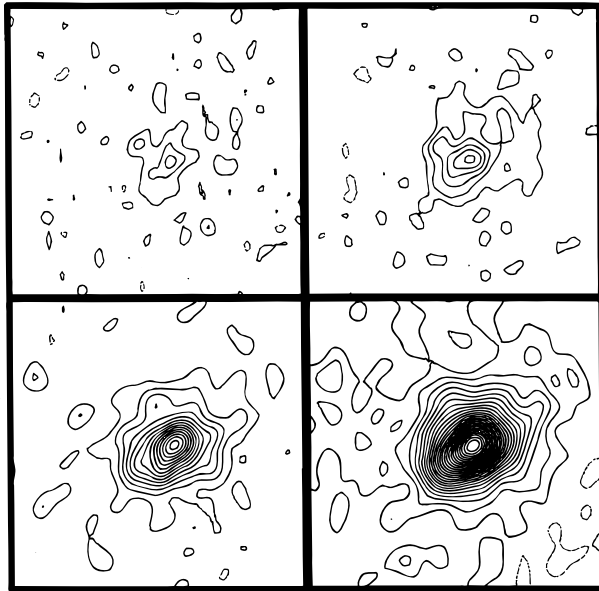
22GHz Uniform 82 x 69, -27° C.I. 0.8mJy	22GHz Natural 100 x 91, -24° C.I. 0.5mJy
15GHz Uniform 123 x 103, -34° C.I. 0.5mJy	15GHz Tapered 269 x 257, -78° C.I. 0.4mJy

1101+410
Field center at:
11^h01^m05^s.810, +41° 07' 10".48



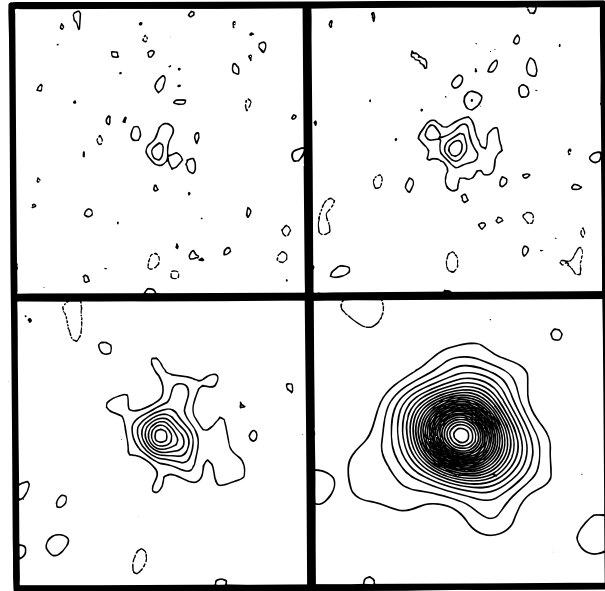
22GHz Uniform 79 x 67, -5° C.I. 1.0mJy	22GHz Natural 102 x 89, -6° C.I. 0.7mJy
15GHz Uniform 119 x 102, -8° C.I. 0.6mJy	15GHz Tapered 267 x 259, -55° C.I. 0.4mJy

MRK 266
Field center at:
13^h36^m15^s.010, +48° 31' 54".08



22GHz Uniform 89 x 68, -3° C.I. 1.3mJy	22GHz Natural 109 x 88, -4° C.I. 1.0mJy
15GHz Uniform 137 x 114, -9° C.I. 0.8mJy	15GHz Natural 162 x 139, -9° C.I. 0.5mJy

MRK 171D
Field center at:
11^h25^m44^s.190, +58° 50' 18".18



22GHz Uniform 90 x 70, -17° C.I. 1.2mJy	22GHz Natural 107 x 89, -14° C.I. 0.8mJy
15GHz Uniform 139 x 115, -19° C.I. 0.8mJy	15GHz Tapered 270 x 258, -48° C.I. 0.5mJy

MRK 273
Field center at:
13^h42^m51^s.710, +56° 08' 14".28

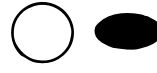


FIG. 3—Continued

the [O III]/H β versus [N II]/H α relation, where each galaxy is plotted with a symbol indicating T_b . The H II/AGN boundary follows the version of this scheme of Veilleux & Osterbrock (1987). This diagram is the basis for the optical

spectral classification listed in Table 3. Although the spectral types would appear to be evenly mixed between H II and AGN classification, we note, as originally emphasized by Sanders et al. (1988), that the H II galaxies all lie very

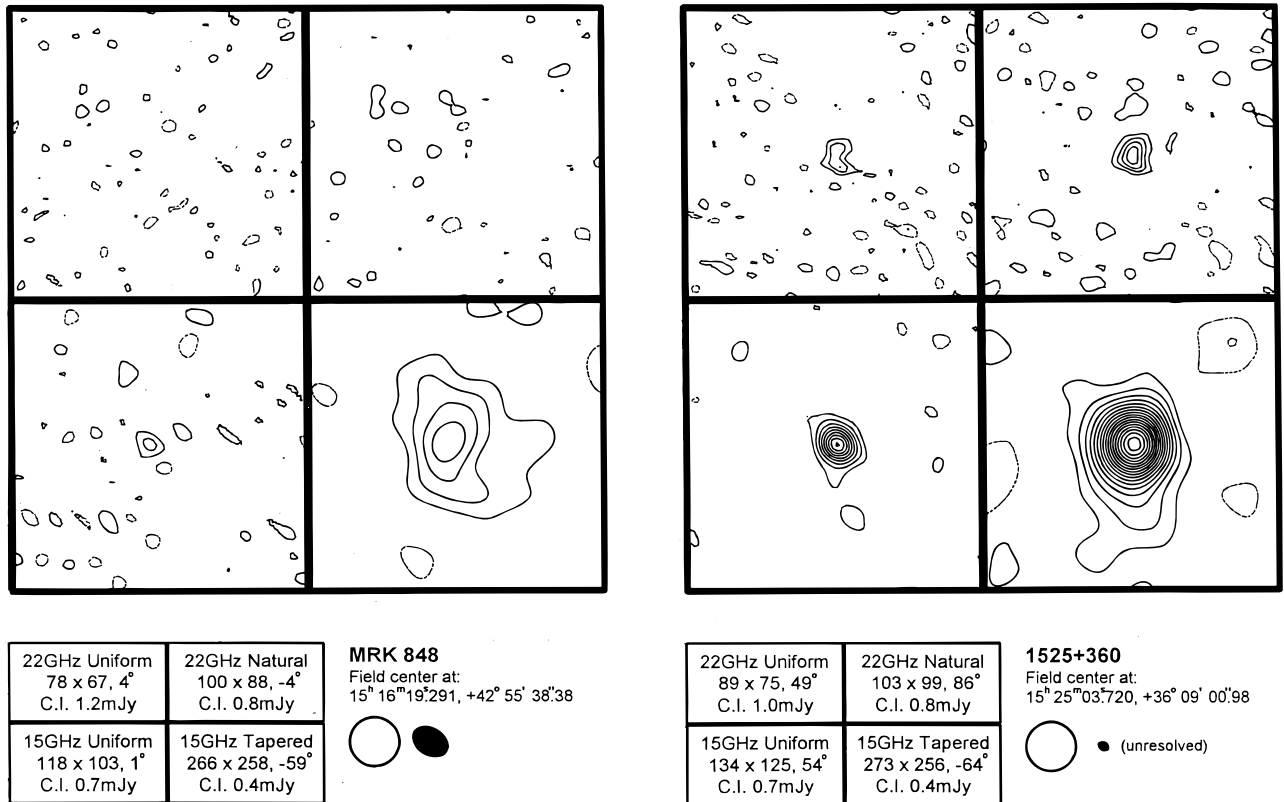


FIG. 3—Continued

close to the H II/AGN boundary, with much higher excitation than typical galactic H II regions and well above the locus of H II models. On the other hand, the majority of AGN systems are, in fact, LINERS (Veilleux et al. 1995), rather than exhibiting classical Seyfert/QSO excitation.

We are, unfortunately, unable to draw firm conclusions based on the optical spectra of our sample. The systems are high excitation for star-forming systems, but low excitation for AGNs. Of particular note is the fact that the emission-line spectrum yields few, if any, clues to the existence of VLBI-scale radio emission. In Figure 4 it is apparent that the distributions of the high- T_b , intermediate- T_b , and undetected sources are not significantly different. Given the amount of obscuring material estimated to be present in the LIG nuclei, it is hardly surprising that physical relationships are also obscured. Infrared spectrophotometric observations (e.g., Spinoglio & Malkan 1992; Voit 1992) may potentially provide a more conclusive discriminant, as, for example in the case of recent *Infrared Space Observatory* (ISO) observations of Arp 220 (Sturm et al. 1996) that show no high-excitation midinfrared features, suggesting a stellar ionizing radiation field in that object.

4. STATISTICAL ANALYSIS

We have used survival analysis (Isobe, Feigelson, & Nelson 1986) statistical techniques to compare the compact VLBI flux densities S_{VLBI} , VLBI powers P_{VLBI} , and 1.5 GHz core fractions $P_{\text{VLBI}}/P_{\text{total}}$, with the other known radio, infrared and optical characteristics of our sample galaxies listed in Tables 1–3. We restrict this analysis to the 31 galaxies in our VLBI experiment so that for most tests there are 17 detections and 14 limits to VLBI power and core fraction. The presence of radio upper limits dictates the use

of survival analysis and we have employed two correlation tests: Cox's Hazard test (parametric, assuming a Gaussian error distribution) and the generalized Kendall's tau nonparametric test, with equivalent results. Table 4 lists the results of the Cox-Hazard correlation test, which provides the familiar χ^2 statistic as estimator of the correlation strength. Potential correlations between VLBI properties and several other observables were examined. These include: far-infrared (FIR) flux density and luminosity, ($25 \mu/60 \mu$) color, ($60 \mu/100 \mu$) color, $60 \mu\text{m}$ spectral shape, $C_{60 \mu} = \alpha(25 \mu\text{m}, 60 \mu\text{m}) - \alpha(60 \mu\text{m}, 100 \mu\text{m})$, FIR-to-radio ratio q , radio spectral index $\alpha_{1.49}^{8.44}$, H_2 gas mass inferred from CO observations, and FIR-to- M_{H_2} ratio (sometimes called the "star formation efficiency").

None of the above correlations are sufficiently strong to provide a compelling case for a physical relationship. We examine briefly those correlations with probability $P \leq 0.10$, smaller than 10% for a chance occurrence. Seventeen basic relationships are tested; we would thus expect there to be a couple of chance correlations among unrelated parameters, of which there are five: (1) VLBI power with infrared luminosity, (2) VLBI power with total 1.49 GHz radio power, (3) VLBI power with molecular gas mass (CO luminosity), (4) VLBI power with radio spectral index, and (5) VLBI fraction with spectral index. In Figure 5 we display the plots for these apparent correlations between VLBI characteristics and other physical parameters. We emphasize that the weaker of these correlations are marginal, at best, and that we fully expect that some are purely by chance. Furthermore, these correlations may not be fundamental, because there are significant correlations among the other parameters tested (e.g., radio-optical correlation). Nonetheless, we explore possible physical origins for these

TABLE 3
SPECTROPHOTOMETRIC DATA

Object (1)	$\log L_{\text{H}\alpha}$ (ergs s^{-1}) (2)	[O III]/H β (3)	[N II]/H α (4)	[S II]/H α (5)	[O I]/H α (6)	Spectral Type (7)	Reference (8)
Mrk 938	42.93	0.50	0.10	-0.33	-0.93	Seyfert 2	1
IC 1623N	41.43	0.10	-0.56	-0.59	-1.43	H II	1
IC 1623SE	41.72	0.36	-0.67	-0.63	-1.66	H II	1
01076-1707	42.48	-0.42	-0.29	-0.66	-1.61	H II	1
01173+1405	0.05	-0.43	-0.47	-1.22	H II	2
01173+1405	42.02	-0.06	-0.41	-0.54	-1.36	H II	1
01364-1042	-0.04	-0.11	-0.66	AGN	2
01364-1042	41.22	0.21:	-0.02:	-0.23:	-0.46:	Liner	1
III Zw 035S	0.05	-0.08	-0.74	AGN	2
III Zw 035S	41.36	0.07:	0.01	-0.31	-0.68	Liner	1
III Zw 035N	0.31	-0.78	-0.49	-1.51	H II	2
III Zw 035N	40.70	0.28	-0.72	-0.52	-1.33	H II	1
NGC 695	41.88	-0.55	-0.35	-0.80	-1.23	H II	1
UGC 2369	42.26	-0.40	-0.28	-0.67	-1.65	H II	1
03359+1523	41.97	0.03	-0.46	-0.72	-1.70	H II	1
04191-1855S(a)	41.51	-0.51	-0.11	-0.45	-1.11	Liner:	1
04191-1855N(b)	41.48	-0.22	-0.20	-0.44	-0.98	Liner	1
NGC 1614	42.67	-0.17	-0.22	-0.72	-1.73	H II	1
05189-2524	42.94	1.5:	0.03	-0.72	-1.12	Seyfert 2	1
NGC 2623	40.73 ^a	...	-0.01	-0.22	-0.99	AGN	1
08572+3915	40.88	0.25	-0.38	...	-1.13	H II	3
08572+3915	41.29	0.31	-0.38	-0.39	-1.28	Liner:	1
UGC 4881NE(b)	0:	-0.16	-0.22	...	H II	2
UGC 4881NE(b)	42.21	-0.55:	-0.15	-0.56	-1.24	H II:	1
UGC 4881SW(a)	-0.20	-0.36	...	H II	2
UGC 4881SW(a)	42.53	-0.33	-0.20	-0.54	-1.26	H II:	1
UGC 5101	43.10	0.36	0.12	-0.45	-0.95	Liner	1
10173+0828	39.93	3
10566+2448	43.05	-0.30	-0.32	-0.59	-1.38	H II	1
11010+4107	0.0	-0.34	-0.46	-1.17	H II	2
UGC 6436NW(a)	42.74	-0.53	-0.32	-0.74	-1.54	H II	1
UGC 6436SE(b)	42.59	...	-0.24	-0.69	-1.55:	AGN	1
Mrk 171D	-0.05	-0.34	-0.50	-1.24	H II	4
12112+0305	40.84	0.28	-0.30	-0.30	-0.95	H II	3
Mrk 231	42.30	Seyfert 1	...
Arp 238	41.7	0.04	-0.38	-0.67	-1.49	H II	1
Arp 238SE(b)	42.33	-0.01	-0.39	-0.67	-1.45	H II	1
Arp 238NW(a)	41.68	0.11	-0.34	-0.46	-1.22	H II:	1
13183+3424	0.24:	-0.18	-0.34	-0.83	AGN	2
13183+3424	41.82	-0.16	-0.18	-0.40	-0.94	Liner	1
Mrk 266	0.15	-0.22	H II	3
Mrk 266NE(c)	41.77	0.62	-0.25	-0.44	-1.25	Seyfert 2	1
Mrk 266SW(a)	41.45	0.14	-0.20	-0.33	-0.91	Liner	1
NGC 5257	40.65	-0.12	-0.46	-0.57	-1.67	H II	1
NGC 5258	-0.25	1
Mrk 273	41.64	0.64	-0.06	-0.29	-0.90	AGN	3
Mrk 273	42.37	0.45	0.01	-0.24	-0.85	Liner	1
14348-1447	0	-0.25	-0.39	-1.26	AGN	3
14348-1447SW(a)	42.74	0.13	-0.23	-0.48	-1.02	Liner	1
14348-1447NE(b)	41.88	0.09	-0.21	-0.51	-0.85	Liner:	1
UGC 9618	40.94	-0.06	-0.09	-0.46	-1.10	Liner	1
Mrk 848N(a)	-0.03	-0.33	-0.59	-1.41	H II	2
Mrk 848N(a)	42.44	-0.04	-0.26	-0.59	-1.42	H II	1
Mrk 848S(b)	-0.01	-0.17	-0.35	-0.95	Liner	1
Mrk 848S(b)	42.32	-0.06	-0.12	-0.35	-1.07	Liner	1
15250+3608	41.03	0.79	-0.32	-0.39	-1.04	AGN	3
15250+3608	41.82	0.11	-0.33	-0.45	-1.13	Liner:	1
Arp 220	40.53	0.20	0.36	-0.13	-0.79	AGN	3
Arp 220W	0.29	-0.04	-0.70	AGN	1
Arp 220E	0.79	0.22	-0.16	-0.62	Seyfert 2	1
NGC 6090NW	42.29	-0.35	-0.48	-0.79	-1.74	H II	1
NGC 6090SE	41.72	0.08	-0.46	-0.65	-1.73	Liner	1
NGC 6285	41.12	-0.33	-0.32	-0.29	-1.24	H II	1
NGC 6286	40.91	-0.25	-0.08	-0.18	-0.81	Liner	1
NGC 6285	-0.24	-0.39	-0.48	-1.35	H II	2
17132+5313W	0.05	-0.17	-0.99	AGN	b
17132+5313E	41.59	-0.37	-0.37	-0.62	-1.41	H II	2
17132+5313W	-0.47	-0.22	1
17132+5313E	41.59	-0.38	-0.35	-0.50	-1.63	H II	1
22491-1808	42.29	-0.19	-0.37	-0.62	-1.24	H II	1

TABLE 3—Continued

Object (1)	$\log L_{\text{H}\alpha}$ (ergs s ⁻¹) (2)	[O III]/H β (3)	[N II]/H α (4)	[S II]/H α (5)	[O I]/H α (6)	Spectral Type (7)	Reference (8)
NGC 7469	42.17	-0.28	-0.74	-1.34	-2.02	Seyfert 1	1
Zw 475.056	0.38	-0.02	AGN	2
Zw 475.056	42.02	0.62	-0.02	-0.59	-1.26	Seyfert 2	1
Mrk 331	-0.34	-0.24	-0.65	-1.54	H II	2
Mrk 331	42.15	-0.46	-0.27	-0.60	-1.55	H II	1

REFERENCES.—(1) Veilleux et al. 1995; (2) this work; (3) Armus et al. 1989; (4) LSL95.

relationships in hopes that they may shed some illumination on the questions that we raise here.

In a previous paper (LSL95) we examined the relationship between far-infrared luminosity and VLBI core

power. While this relationship is not highly significant ($P = 8\%$), LSL95 showed that there is a common relationship between luminosity and VLBI power for LIGs and radio-quiet quasars, suggesting a possible physical relationship. Unfortunately, this relationship is not a discriminator between AGN and starburst models. If the compact, high- T_b emission in LIGs comes from starburst-generated radio supernovae (RSNs), then the supernova rate, and therefore the compact radio emission, should scale directly with the star formation rate, as does the infrared luminosity. The second observed correlation, between total radio power and VLBI power ($P = 1\%$), is also present, though at lower significance ($P = 9\%$), in the total flux versus VLBI flux relationship, and suggests that there is a physical relationship between the mechanisms producing the compact and extended radio power. The presence of the third correlation, between the mass of molecular gas, inferred from CO observations, and VLBI power ($P = 5\%$), is to be expected if starburst-generated RSNs produce the VLBI-scale emission, or, in hybrid starburst/AGN models, if starburst-related winds or supernovae provide the fuel for accretion onto a compact object in the AGN core (Norman & Scoville 1988; Perry & Dyson 1985).

The radio spectral index may be expected to have a value, $\alpha_{1.49}^{8.44} \approx 0.7$, appropriate for optically thin synchrotron emission, which may then be “flattened” by free-free absorption or by the presence of multiple, compact, self-absorbed synchrotron components. CHYT interpreted these galaxies as ultracompact starbursts with thermal dust emission at $T \approx 60\text{--}80$ K and densities so large as to be optically thick to free-free absorption at 1.6 GHz and to dust extinction at $25 \mu\text{m}$. (For this reason we have avoided mid-IR quantities, $\lambda \leq 20 \mu\text{m}$, where $\tau_{\text{dust}} \gtrsim 1$ and where there are also many censored data points.) In either case, the spectral index may be taken as a measure of compactness and the correlations in VLBI power and VLBI fraction with spectral index suggest that compactness on VLA scales is related to the presence of VLBI emission.

With the exception of Mrk 231 there is no evidence for self-absorbed synchrotron components in these sources, but there is certainly ionized gas capable of producing free-free absorption. We have made optical depth corrections to the appropriate radio quantities following CHYT by assuming a uniform intrinsic spectral index $\alpha_0 = 0.70$ between 1.49 and 8.44 GHz. Because the free-free optical depth is $\tau_{\text{ff}} \propto \lambda^2$, there will not be significant optical depth at 8.44 GHz. In this case:

$$\tau_{\text{ff}} \approx 2.3(\alpha_0 - \alpha_{1.49}^{8.44}). \quad (2)$$

In six cases, most with large uncertainty $\alpha > 0.70$, these sources were not corrected. The inferred optical depths are $0 \leq \tau_{\text{ff}} \leq 1.36$, excluding Mrk 231, a “consensus monster,”

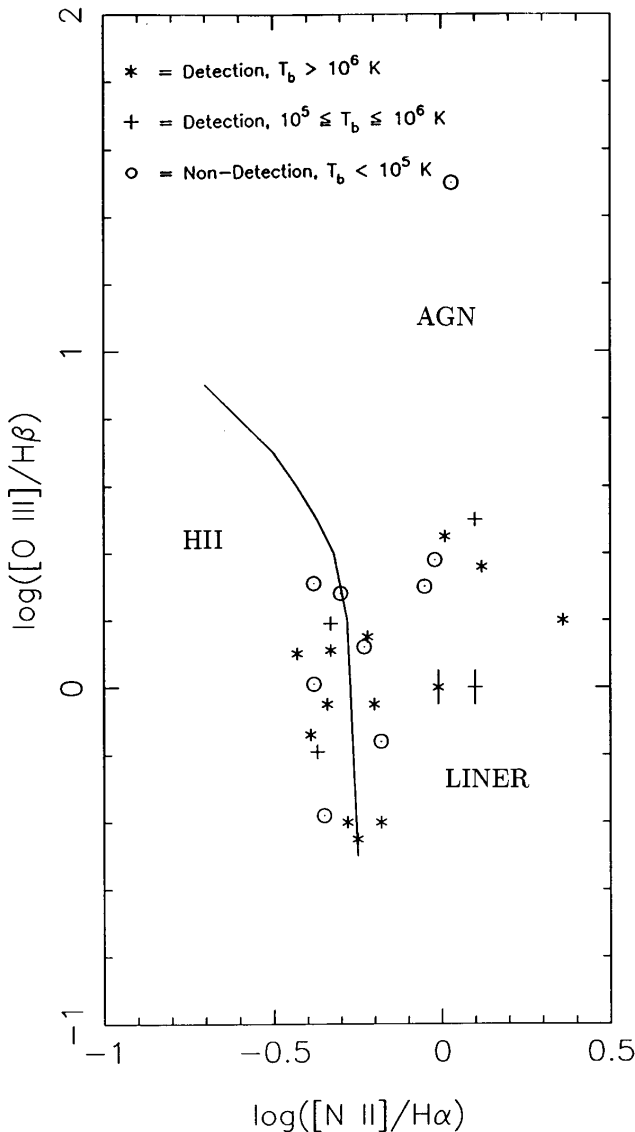


FIG. 4.—Excitation diagram for the LIG sample. The solid line represents the boundary between thermal and nonthermal excitation (Veilleux & Osterbrock 1987). Two broad-line objects with positive detections, Mrk 231 and NGC 7469, have been omitted. VLBI detections with high brightness temperature are plotted with an asterisk; detections with $T_b \sim 10^5\text{--}10^6$ K are plotted as a plus; nondetections are open circles. While most galaxies with AGN-like optical spectra show compact high- T_b emission, excitation is not a good indication of the presence of compact VLBI emission.

TABLE 4
COX-HAZARD CORRELATION TESTS FOR THE LFIRG SAMPLE

Independent Variable (1)	Dependent Variable (2)	Number of Data Points (3)	Number of Upper Limits (4)	χ^2 (5)	P (6)		
L_{FIR}	P_{VLBI}	31	14	3.1	0.08		
	P'_{VLBI}			3.8	0.05		
	$P_{\text{VLBI}}/P_{\text{tot}}$			0.10	0.75		
P_{tot}	P_{VLBI}	31	14	6.6	0.01		
	P'_{VLBI}			0.06	0.81		
	$P_{\text{VLBI}}/P_{\text{tot}}$			0.24	0.62		
[25/60]	P_{VLBI}	31	14	0.00	0.99		
	P'_{VLBI}			0.24	0.62		
	$P_{\text{VLBI}}/P_{\text{tot}}$			0.06	0.80		
[60/100]	P_{VLBI}	31	14	0.05	0.82		
	P'_{VLBI}			0.02	0.90		
	$P_{\text{VLBI}}/P_{\text{tot}}$			0.21	0.65		
C_{60}	P_{VLBI}	31	14	2.7	0.10		
	P'_{VLBI}			4.7	0.03		
	$P_{\text{VLBI}}/P_{\text{tot}}$			2.1	0.15		
$\alpha_{1.49}^{8.44}$	P_{VLBI}	31	14	0.8	0.36		
	P'_{VLBI}			3.8	0.05		
	$P_{\text{VLBI}}/P_{\text{tot}}$			2.4	0.12		
q	P_{VLBI}	27	13	4.0	0.05		
	P'_{VLBI}			3.7	0.05		
	$P_{\text{VLBI}}/P_{\text{tot}}$			0.71	0.40		
q	P_{VLBI}	27	13	0.14	0.71		
	P'_{VLBI}			0.07	0.79		
	$P_{\text{VLBI}}/P_{\text{tot}}$			0.45	0.50		
q'	L_{FIR}	34	0	6.5	0.01		
	P_{tot}			17.6	$< 10^{-4}$		
	P'_{tot}			58.9	$\leq 10^{-4}$		
q'	q	40	0	3.8	0.05		
	q'			1.2	0.28		
	[25/60]			0.5	0.49		
M_{H_2}	[60/100]	40	0	10.8	0.001		
	$\alpha_{1.49}^{8.44}$			37	0	6.2	0.01

with a presumed inherently flat spectrum. This reduces the mean FIR-to-radio ratio from $\langle q \rangle = 2.48$, to $\langle q' \rangle = 2.39$ (again excluding Mrk 231), closer to the well-defined mean value $q = 2.34$, observed for the BGS as a whole. If the inferred *integrated* free-free optical depths are correct, then the 1.6 GHz VLBI power, which likely originates in the innermost obscured regions of the source, must probably be corrected for even larger optical depths. Applying the optical depth correction inferred above does not significantly alter the median VLBI power, because most of the lower luminosity sources have steep spectra and low inferred optical depth, but it raises the upper envelope of VLBI power to in excess of $\log P_{\text{VLBI}} = 23$ (W Hz^{-1}). The corrected quantities, q' , P'_{VLBI} , and $P'_{1.49}$, are listed in Table 5. The correlation tests were also performed with the corrected radio parameters, and the results are listed in Table 4, as well. In many cases there is a small improvement in the significance of correlations with P'_{VLBI} . (Note that the correction is not altered by this correction.) For example, the probability of chance occurrence decreases from 8% to 5% for L_{FIR} versus P'_{VLBI} . Also, there is now an apparently significant (inverse) correlation between corrected radio-infrared parameter, q' , and P'_{VLBI} . If AGNs contribute to the flux density at a measurable level, this may suggest that AGN activity contributes a greater share of the radio than the infrared. This is at variance with the results of LSL95, which indicate that radio-quiet quasars have a *higher* ratio of L_{bol} -to- $P_{1.49}$ than do LIGs.

We have, for comparison, tested relationships between infrared luminosity and the other physical characteristics

listed in Table 1. A number of correlations, found previously for the BGS as a whole, are shown to hold for the complete LIG sample: molecular gas mass and infrared luminosity, FIR color and infrared luminosity, and the well-known radio-infrared correlation. For this sample we also find significant correlations between L_{FIR} and radio spectral index and FIR-to-radio ratio q . These correlations are shown in Figure 6.

The correlation between M_{H_2} and L_{FIR} has been well studied (Sanders et al. 1991; Solomon, Downes, & Radford 1992; Solomon et al. 1997) and strongly suggests that star formation is occurring in these gas-rich systems. However, recent evidence suggests that the geometry of the molecular gas in LIGs has a disklike, rather than a giant molecular cloud (GMC) structure (Scoville, Yun, & Bryant 1997; Bryant & Scoville 1996), and one might expect that the relationship between the star formation rate and gas mass may accordingly be different. Indeed, the best-fit regression lines to the 35 galaxies with $\text{H}_2(\text{CO})$ measures finds a flatter relationship with a luminosity intercept at about $L = 1.5 \times 10^{11} L_{\odot}$, suggesting a lower star-formation rate per unit gas mass plus a possible additional component to the luminosity. Similar results have been obtained by Solomon et al. (1997) and Sanders et al. (1991) with differing interpretations.

Relationships between infrared colors and luminosity have been discussed previously and used to select AGN candidates in the *IRAS* databases (Low, Huchra, & Kleinmann 1988, Low et al. 1989). Very simple models for infrared emission from hot dust surrounding either AGNs or

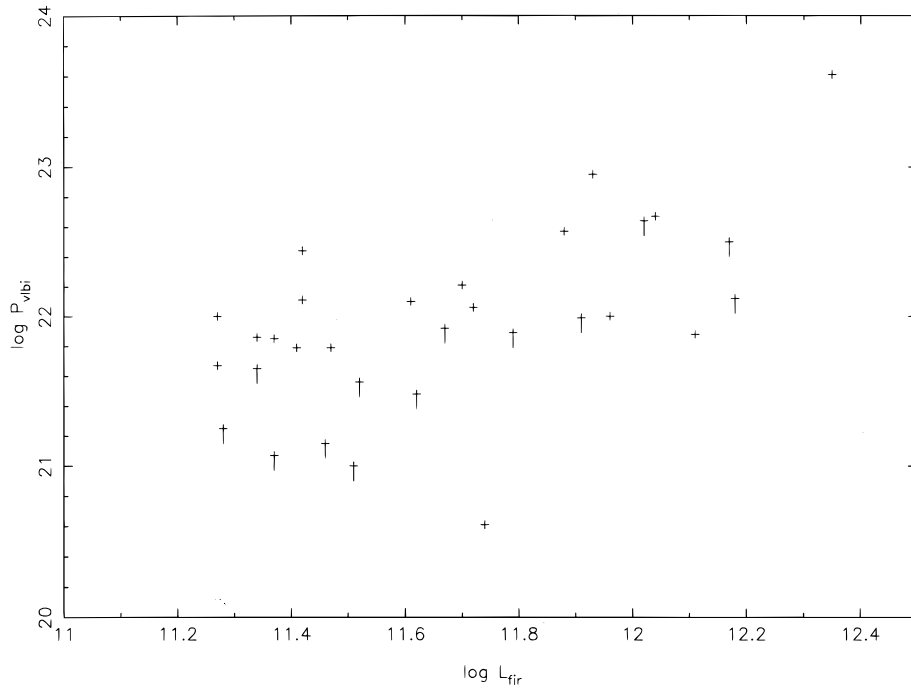


FIG. 5a

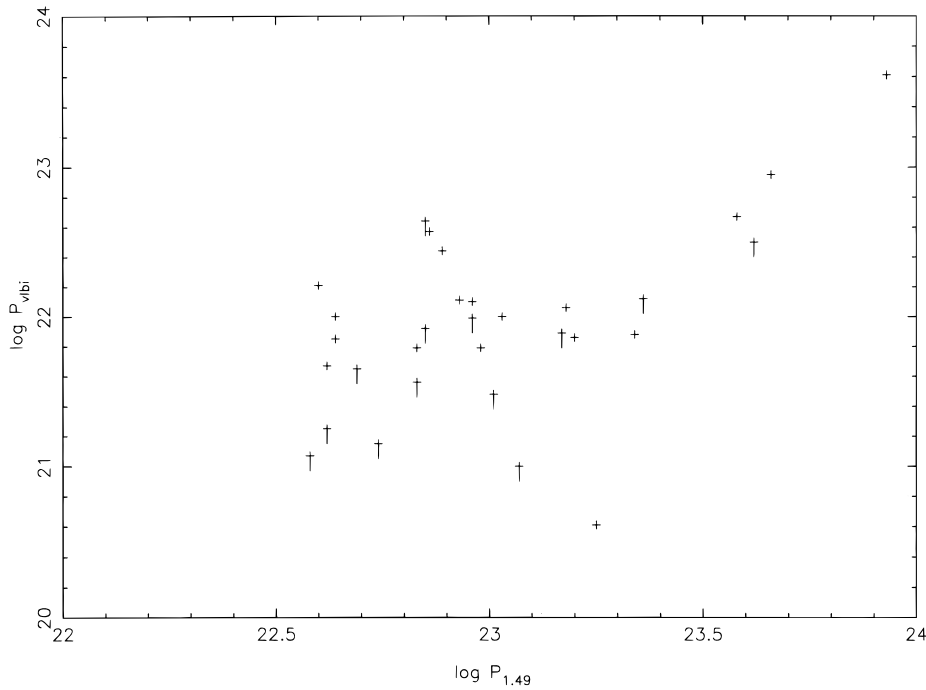


FIG. 5b

FIG. 5.—Correlation diagrams between VLBI and other physical characteristics for the LIG sample. Thirty-one data points are plotted: 17 detections and 14 upper limits. (a) VLBI power vs. infrared luminosity ($P = 8\%$ for chance correlation; the probability for chance occurrence decreases to 5% when VLBI power is corrected for free-free extinction; see text). (b) VLBI power vs. total 1.49 GHz radio power ($P = 1\%$). (c) VLBI power vs. 1.49–8.44 GHz radio spectral index ($P = 10\%$). This correlation is almost entirely produced by Mrk 231 with $\alpha_{1.49}^{8.44} = -0.06$. (d) VLBI fraction ($P_{\text{VLBI}}/P_{1.49}$) vs. radio spectral index ($P = 3\%$). (e) VLBI power vs. molecular gas mass (derived from CO luminosity; $P = 5\%$). (f) Optical depth *corrected* VLBI power vs. *corrected* radio-to-infrared ratio ($P = 5\%$); this correlation is only significant at the 12% level in the uncorrected data.

starbursts can plausibly explain such a relationship. The LIGs are compact as a class, with radio emission typically confined to a region, $\theta \lesssim 0''.25$ (CHYT), thus the correlation between infrared luminosity and spectral index is likely to be a continuation of the trend toward compactness with

increasing luminosity. Given that there is a fairly significant correlation between $\alpha_{1.49}^{8.44}$ and L_{FIR} , and a weak correlation between L_{FIR} and P_{VLBI} , it is not surprising that there is also a weak correlation between $\alpha_{1.49}^{8.44}$ and P_{VLBI} . Furthermore, this correlation completely disappears if Mrk 231 with

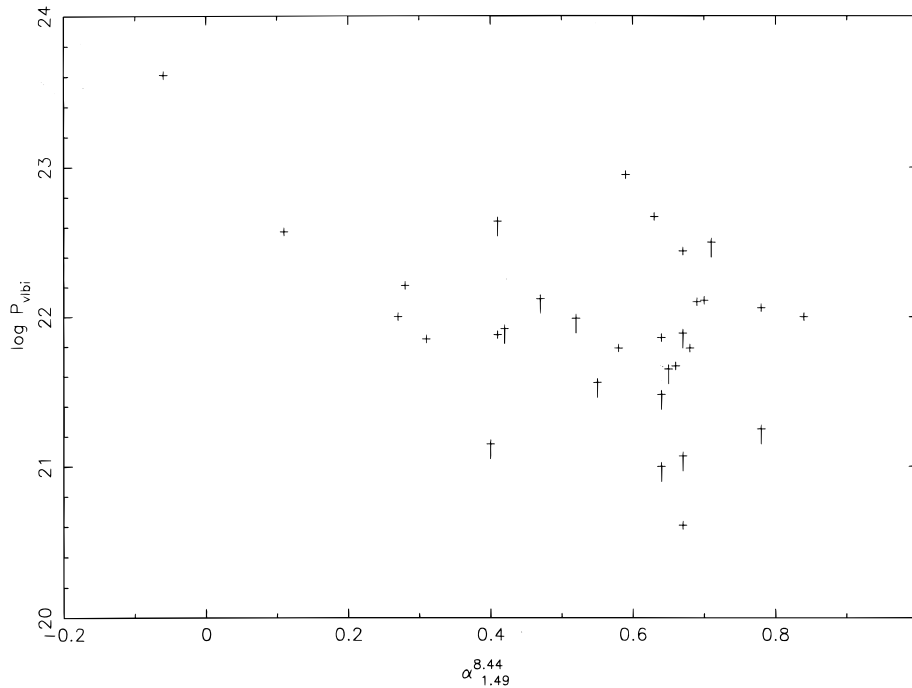


FIG. 5c

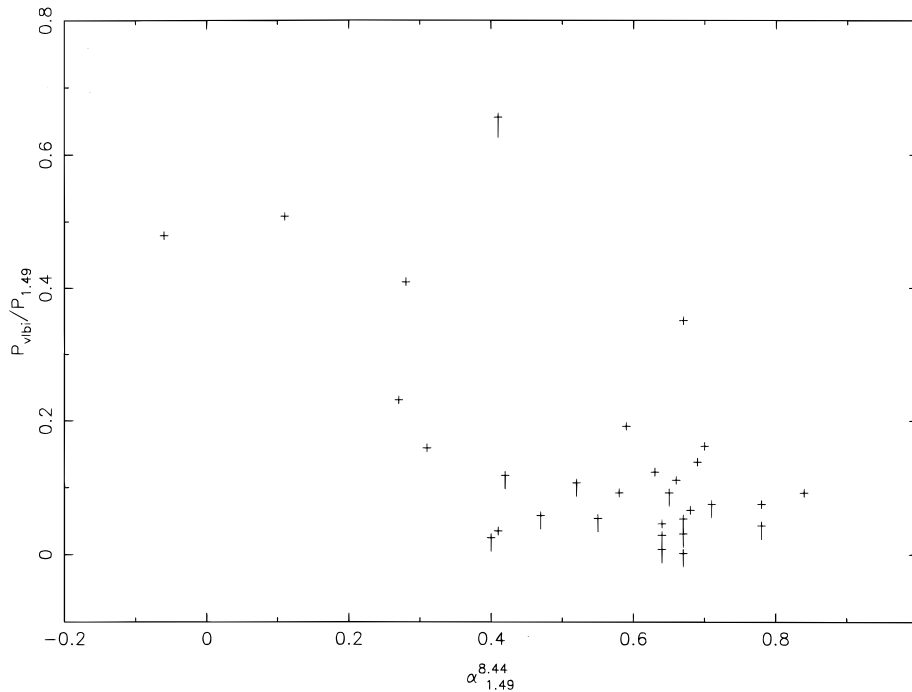


FIG. 5d

$\alpha = -0.06$ is omitted from the sample. The only highly significant ($P \ll 1\%$) correlation among these characteristics is the radio-infrared correlation. As noted by CHYT, correction for free-free optical depth not only reduces the infrared-radio parameter q to a value closer to the mean for starburst galaxies, but strengthens the correlation (Mrk 231 is included in the correlation test, but not corrected for free-free extinction).

Taken as a whole, these statistical relationships strongly suggest that there is a continuity between the LIGs and

lower luminosity starbursts in physical characteristics. Furthermore, the molecular gas emission, infrared luminosity and radio power on VLA-VLBI scales appear to be physically related. Active star formation is certainly occurring in the majority of these LIGs and our statistical analysis is consistent with a starburst origin for the radio, millimeter, and infrared emission. This analysis does also admit for the possibility of a hybrid or dual nature (e.g., starburst and AGN) for the LIGs. Although the relationships between VLBI and other characteristics are suggestive, they neither

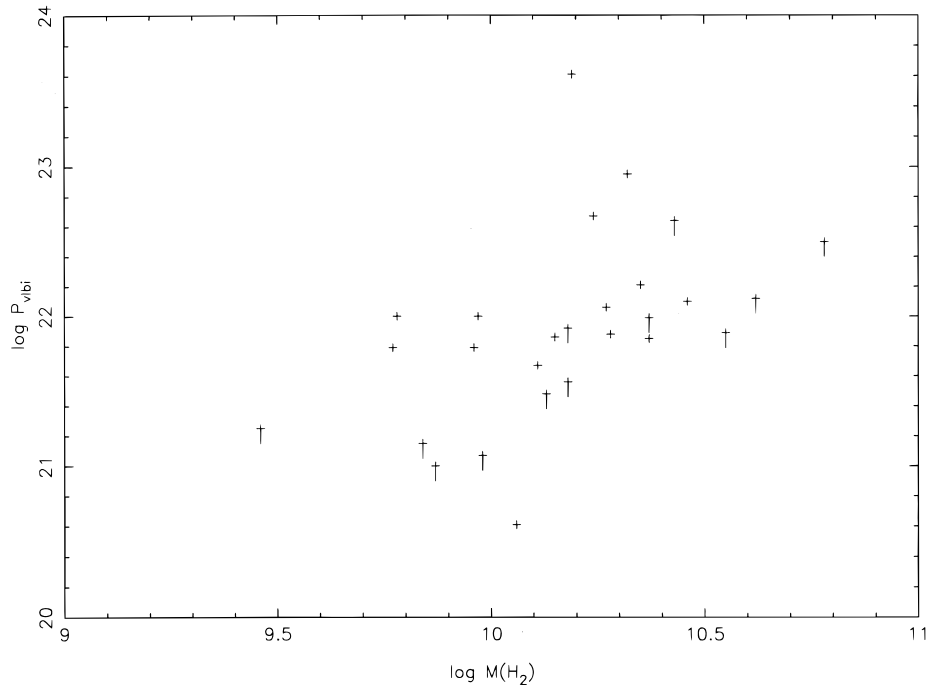


FIG. 5e

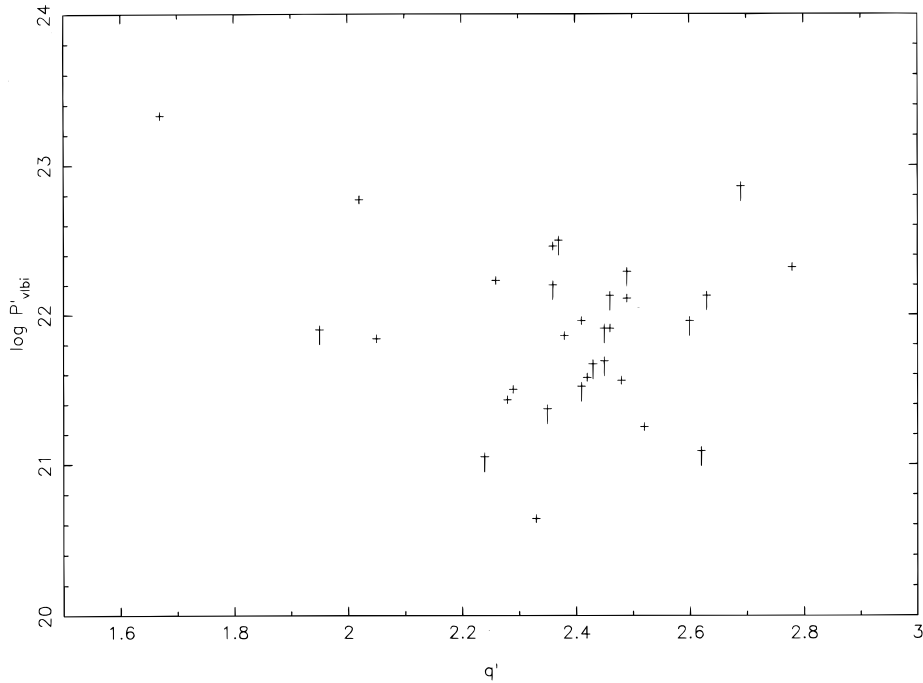


FIG. 5f

provide a statistical framework for interpretation of the VLBI emission in terms of either starbursts or AGNs, nor suggest an evolutionary path.

5. STARBURST MODELS

As described above, LSL95 showed that it is plausible that the LIGs are powered by AGNs with radio core properties comparable to those of radio-quiet QSOs. Now we ask the complementary question: Is it plausible that the LIGs are powered by starbursts? We examine simple starburst models for the LIGs in order to examine whether such

models lead us to fundamental physical difficulties and to estimate the star formation rate, supernova frequency, and other parameters that may be used for interpretation of our results.

For a power-law initial mass function (IMF), $\psi(m) \propto m^{-\gamma}$ (e.g., $\gamma = -2.5$, $m > 1 M_{\odot}$, following Miller & Scalo 1979) one may create heuristic scaling-law models for observable features of a starburst in terms of the star formation rate, \dot{m} , and m_l and m_u , the lower mass cutoff and upper mass cutoff for star formation. Here we follow Scoville & Soifer (1991) who employ a modified Miller & Scalo IMF to derive the

TABLE 5

LUMINOUS FIR GALAXY STARBURST MODELS

SYSTEM (1)	OBSERVED					CORRECTED					MODEL				
	L_{FIR} (2)	P_{VLBI} (3)	$P_{1.49}$ (4)	q (5)	τ_{fr} (6)	P'_{VLBI} (7)	$P'_{1.49}$ (8)	q' (9)	L_{Hz} (10)	SFR (11)	P_{out} (12)	v_{in} (13)	L_{Hz} (14)	t_{gas} (15)	
	Model 1: $m_1 = 1 M_{\odot}$; $m_n = 45 M_{\odot}$; $t_{\text{*}} = 10^{8.0}$ yr; $m_{\text{in}} = 8 M_{\odot}$; $\langle P_{\text{nl}}/P_{\text{fr}} \rangle = 25$ @ 1.5 GHz; $q = 2.35$; $\log(M/L) = -2.59 (M_{\odot}/L_{\odot})$														
Mrk 938	11.28	<21.25	22.62	2.52	0.00	<21.25	22.62	2.52	42.93	16.14	22.80	0.26	42.01	8.25	
IC 1623	11.39	<21.45	23.11	2.14	0.00	<21.45	23.11	2.14	41.90	20.80	22.91	0.33	42.12	9.12	
01076-1707	11.42	<21.39	22.93	2.35	0.00	<21.39	22.93	2.35	42.48	22.28	22.94	0.36	42.15	8.95	
01173+1405	11.54	22.11	22.90	2.46	0.00	22.11	22.90	2.46	42.02	29.38	23.06	0.47	42.27	...	
01364-1042	11.67	<21.92	22.85	2.67	0.49	<22.13	23.06	2.46	41.22	39.63	23.19	0.63	42.40	8.58	
III Zw 35	11.46	<21.15	22.74	2.57	0.52	<21.37	22.97	2.34	41.45	24.43	22.98	0.39	42.19	8.45	
NGC 695	11.51	<21.38	23.13	2.22	0.00	<21.38	23.13	2.22	41.88	27.42	23.03	0.44	42.24	8.90	
UGC 2369	11.42	22.44	22.89	2.38	0.05	22.46	22.91	2.36	42.26	22.28	22.94	0.36	42.15	...	
03359+1523	11.37	21.85	22.64	2.58	0.68	22.14	22.94	2.29	41.97	19.86	22.89	0.32	42.10	9.07	
04191-1855	11.34	<21.65	22.69	2.49	0.09	<21.69	22.73	2.45	41.80	18.54	22.86	0.30	42.07	...	
NGC 1614	11.39	...	22.67	2.58	0.00	...	22.67	2.58	42.67	20.80	22.91	0.33	42.12	8.71	
05189-2524	11.91	<21.99	22.96	2.76	0.31	<22.13	23.10	2.62	42.94	68.87	23.43	1.10	42.64	8.53	
NGC 2623	11.47	21.79	22.83	2.50	0.21	21.88	22.92	2.41	...	25.00	22.99	0.40	42.20	8.37	
08572+3915	11.96	<22.00	22.63	3.10	0.75	<22.32	22.96	2.78	...	77.27	23.48	1.24	42.69	7.89	
UGC 4881	11.61	22.10	22.96	2.49	0.02	22.11	22.97	2.48	42.70	34.51	23.13	0.55	42.34	8.92	
UGC 5101	11.93	22.95	23.67	2.10	0.19	23.04	23.75	2.02	43.10	72.11	23.45	1.15	42.66	8.46	
10173+0828	11.70	22.21	22.59	2.91	0.73	22.52	22.91	2.59	...	42.46	23.22	0.68	42.43	8.72	
10566+2448	11.90	<22.43	23.20	2.55	0.03	<22.44	23.22	2.53	43.05	67.30	23.42	1.08	42.63	8.51	
11010+4107	11.52	<21.56	22.83	2.54	0.26	<21.67	22.94	2.43	...	28.05	23.04	0.45	42.25	8.73	
UGC 6436	11.44	<21.94	22.71	2.57	0.00	<21.94	22.71	2.57	42.97	23.33	22.96	0.37	42.17	8.89	
Mrk 171	11.74	20.61	23.26	2.34	0.05	20.64	23.28	2.32	...	46.56	23.26	0.75	42.47	8.39	
12112+0305	12.18	<22.12	23.36	2.66	0.40	<22.29	23.53	2.49	...	128.23	23.70	2.05	42.91	8.51	
Mrk 231	12.55	23.61	23.93	2.23	...	23.61	23.93	2.23	42.30	189.67	23.87	3.04	43.08	7.91	
Arp 238	11.62	<21.48	23.01	2.45	0.10	<21.52	23.06	2.40	42.42	35.32	23.14	0.57	42.35	8.58	
13183+3424	11.51	<21.00	23.07	2.28	0.10	<21.05	23.12	2.23	41.82	27.42	23.03	0.44	42.24	8.43	
Mrk 266	11.34	21.86	23.20	1.99	0.10	21.90	23.24	1.94	41.94	18.54	22.86	0.30	42.07	8.88	

TABLE 5—Continued

SYSTEM (1)	OBSERVED					CORRECTED					MODEL				
	L_{FIR} (2)	P_{VLBI} (3)	$P_{1.49}$ (4)	q (5)	τ_{fr} (6)	P_{VLBI} (7)	$P_{1.49}$ (8)	q' (9)	L_{Hz} (10)	SFR (11)	P_{out} (12)	v_{sn} (13)	L_{Hz} (14)	t_{max} (15)	
NGC 5257/8	11.37	<21.11	22.71	2.51	0.00	<21.11	22.71	2.51	40.65	19.86	22.89	0.32	42.10	...	
Mrk 273	12.04	22.67	23.58	2.31	0.12	22.73	23.64	2.26	42.37	92.90	23.56	1.49	42.77	8.27	
14348–1447	12.17	<22.50	23.62	2.37	0.00	<22.50	23.62	2.37	42.80	125.31	23.69	2.01	42.90	8.68	
UGC 9618	11.58	<21.64	23.20	2.19	0.17	<21.72	23.28	2.11	40.94	32.21	23.10	0.52	42.31	...	
Mrk 848	11.72	22.06	23.19	2.38	0.00	22.06	23.19	2.38	42.69	44.46	23.24	0.71	42.45	8.62	
15250+3608	11.88	22.57	22.86	2.80	1.02	23.01	23.31	2.36	41.82	64.27	23.40	1.03	42.61	...	
Arp 220	12.11	21.88	23.34	2.62	0.50	22.10	23.56	2.40	42.30	109.14	23.63	1.75	42.84	8.24	
NGC 6090	11.33	<21.33	22.93	2.25	0.00	<21.33	22.93	2.25	42.40	18.11	22.85	0.29	42.06	8.89	
NGC 6286	11.27	22.00	23.04	2.05	0.00	22.00	23.04	2.05	40.91	15.78	22.79	0.25	42.00	8.77	
17132+5313	11.79	<21.89	23.16	2.46	0.05	<21.91	23.19	2.44	41.59	52.24	23.31	0.84	42.52	8.83	
22491–1808	12.02	<22.64	22.82	2.90	0.50	<22.86	23.04	2.68	42.29	88.72	23.54	1.42	42.75	8.48	
NGC 7469	11.41	21.79	22.98	2.29	0.03	21.81	23.00	2.27	42.17	21.78	22.93	0.35	42.14	8.62	
Zw 475.056	11.37	<21.07	22.58	2.64	0.05	<21.09	22.60	2.62	42.02	19.86	22.89	0.32	42.10	8.68	
Mrk 331	11.27	21.67	22.62	2.51	0.07	21.70	22.65	2.48	42.15	15.78	22.79	0.25	42.00	8.91	
n	40	17	40	40	39	17	40	39	35	40	40	40	35	35	
<1>	11.63	22.13	23.00	2.47	0.20	22.22	23.08	2.39	42.12	36.35	23.15	0.58	42.35	8.61	
Model 2: $m_1 = 8 M_{\odot}$; $m_u = 45 M_{\odot}$; $t_{*b} = 10^{8.0}$ yr; $m_{\text{sn}} = 8 M_{\odot}$; $\langle P_{\text{nl}}/P_{\text{fr}} \rangle = 25$ at 1.5 GHz; $q = 2.35$; $\log(M/L) = -2.59 (M_{\odot}/L_{\odot})$															
<2>	11.58 23.15 0.77 42.35 9.13														
Model 3: $m_1 = 0.1 M_{\odot}$; $m_u = 60 M_{\odot}$; $t_{*b} = 10^{8.0}$ yr; $m_{\text{sn}} = 8 M_{\odot}$; $\langle P_{\text{nl}}/P_{\text{fr}} \rangle = 16$ at 1.5 GHz; $q = 2.33$; $\log(M/L) = -1.91 (M_{\odot}/L_{\odot})$															
<3>	55.50 23.16 0.50 42.55 8.45														
LH Model: $m_1 = 1 M_{\odot}$; $m_u = 100 M_{\odot}$; $t_{*b} = 10^{8.0}$ yr; $m_{\text{sn}} = 8 M_{\odot}$; $\langle P_{\text{nl}}/P_{\text{fr}} \rangle = 12.5$ at 1.5 GHz; $q = 2.34$; $\log(M/L) = -1.91 (M_{\odot}/L_{\odot})$															
<LH>	23.67 23.15 0.47 43.055 8.81														

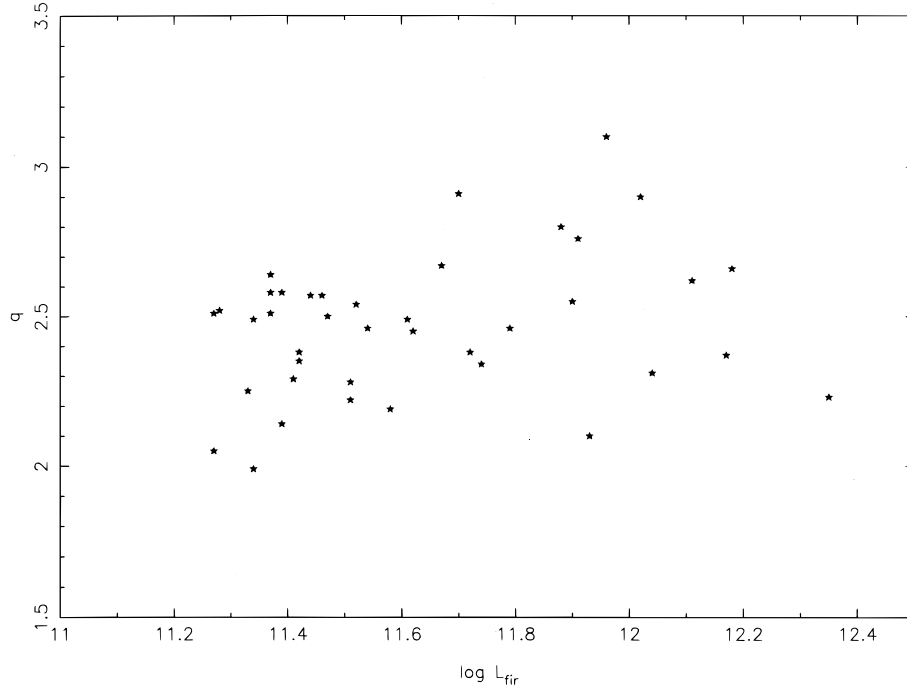


FIG. 6a

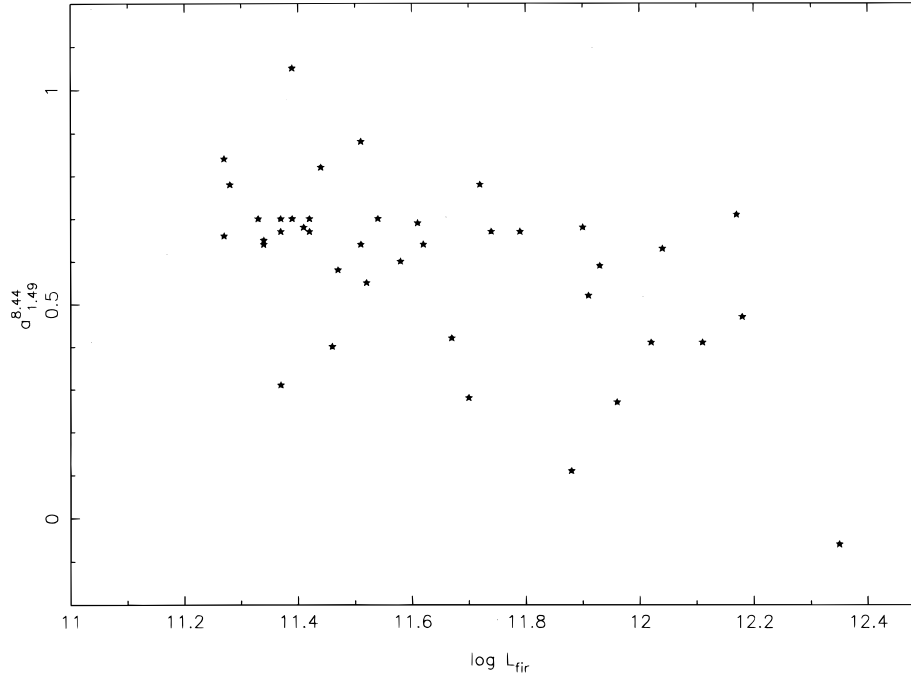


FIG. 6b

FIG. 6.—(a) Correlation between radio-infrared parameter q and infrared luminosity ($P = 5\%$). (b) Correlation between radio spectral index $\alpha_{8.44}^{1.49}$ and infrared luminosity ($P = 5\%$).

bolometric (in this case far-infrared) luminosity for a constant star formation rate starburst

$$L_{\text{FIR}} = 1.2 \times 10^{10} L_{\odot} \left(\frac{m_l}{1 M_{\odot}} \right)^{\alpha} \left(\frac{m_u}{45 M_{\odot}} \right)^{0.37} \times \left(\frac{\Delta t_{*b}}{10^8 \text{ yr}} \right)^{0.67} \dot{m} (M_{\odot} \text{ yr}^{-1}), \quad (3)$$

for values of m_l , m_u , and Δt_{*b} near the fiducial values. Here Δt_{*b} is the starburst lifetime, and $\alpha = 0.23$ for $m_l < 1 M_{\odot}$. Unfortunately the parameters m_l , m_u , and Δt_{*b} are poorly constrained. There is strong evidence that $10^7 \text{ yr} \lesssim \Delta t_{*b} \lesssim 10^9 \text{ yr}$; for interaction triggered starbursts one would expect the duration to be of the order of the dynamical time, $\Delta t_d \sim 10^8 \text{ yr}$. A number of considerations suggest that the IMF is truncated at lower initial mass and does not extend below

about $1 M_{\odot}$ (Scalo 1986), but the actual value of the lower mass cutoff is controversial and may vary from system to system; m_u , which determines the heating rate and the flux of ionizing photons, is virtually unknown from independent arguments. For the remaining discussion we will adopt $m_l = 1 M_{\odot}$, $m_u = 45 M_{\odot}$, and $\Delta t_{*b} = 10^8$ yr. If we consider a “typical LIG” with $\log L_{\text{FIR}} = 11.5$, the implied star formation rate (SFR) is $\dot{m} = 27 M_{\odot} \text{ yr}^{-1}$.

The Lyman continuum photon flux is given by

$$N(\nu > \nu_0) = 9.85 \times 10^{52} \text{ s}^{-1} \left(\frac{m_l}{1 M_{\odot}} \right)^{\alpha} \times \left(\frac{m_u}{45 M_{\odot}} \right)^{\beta} \dot{m} (M_{\odot} \text{ yr}^{-1}), \quad (4)$$

where $\beta = 2.00$ for $m_u < 45 M_{\odot}$ and $\beta = 1.35$ for $m_u > 45 M_{\odot}$. From this we may calculate the radio power from thermal bremsstrahlung,

$$P_{\nu}(f - f) = 2.6 \times 10^{21} \text{ W Hz}^{-1} g_{\text{ff}} \frac{e^{-h\nu/kT}}{T^{1/2}} \times \left(\frac{m_l}{1 M_{\odot}} \right)^{\alpha} \left(\frac{m_u}{45 M_{\odot}} \right)^{\beta} \dot{m} (M_{\odot} \text{ yr}^{-1}), \quad (5)$$

which for $T = 10,000$ K at a frequency $\nu = 1.5$ GHz reduces to

$$P_{1.5 \text{ GHz}}(f - f) = 1.58 \times 10^{-33} \text{ W Hz}^{-1} N(\nu > \nu_0). \quad (6)$$

Condon & Yin (1990) suggest that there is a fairly universal nonthermal-to-thermal ratio of radio emission

$$\left\langle \frac{P_{\text{nt}}}{P_{\text{ff}}} \right\rangle \approx 10 \left(\frac{\nu}{1 \text{ GHz}} \right)^{0.1 - \alpha}, \quad (7)$$

where the nonthermal spectral index is $\alpha \approx 0.7$. We then estimate a total 1.5 GHz power $P \approx 3.2 \times 10^{22} \text{ W Hz}^{-1}$.

However, the radio-to-infrared ratio q , defined in terms of L_{FIR} and $P_{1.5 \text{ GHz}}$, suggests a different nonthermal-to-thermal ratio

$$q = \log \left[\frac{L_{\text{FIR}}(L_{\odot})/3.75 \times 10^{12} L_{\odot}}{P_{1.5 \text{ GHz}}} \right], \quad (8)$$

such that

$$q \approx 3.76 - \log \left(\left\langle \frac{P_{\text{nt}}}{P_{\text{ff}}} \right\rangle + 1 \right) + (0.37 - \beta) \log \left(\frac{m_u}{45 M_{\odot}} \right) + 0.67 \log \left(\frac{\Delta t_{*b}}{10^8 \text{ yr}} \right). \quad (9)$$

For our model, we calculate $q \approx 2.81$, nearly a factor of 3 higher than the canonical value $\langle q \rangle \approx 2.34$ for the BGS (Condon et al. 1991a). Adopting $q = 2.34$ then requires a nonthermal-to-thermal ratio

$$\left\langle \frac{P_{\text{nt}}}{P_{\text{ff}}} \right\rangle \approx 30 \left(\frac{\nu}{1 \text{ GHz}} \right)^{0.1 - \alpha}, \quad (10)$$

which we adopt for the purposes of consistency.

Of particular interest for understanding the origin of LIG radio emission is the supernova rate. For a population with minimum initial mass for supernova detonation, m_{sn} , the supernova rate is

$$\nu_{\text{sn}} = \int_{m_{\text{sn}}}^{m_u} \psi(m) dm \approx \frac{\dot{m}}{3} \frac{(m_{\text{sn}}^{-1.5} - m_u^{-1.5})}{(m_l^{-0.5} - m_u^{-0.5})} \quad (11)$$

for $m_l \geq 1.0 M_{\odot}$. For $m_{\text{sn}} = 8 M_{\odot}$ our typical luminous IR galaxy with $\log L_{\text{FIR}} = 11.5$ would have a supernova rate, $\nu_{\text{sn}} \approx 0.4 \text{ yr}^{-1}$. Provided that the nonthermal radio emission is produced by starburst-related supernovae and remnants, there should exist a direct relationship between P_{nt} and ν_{sn} . Condon & Yin (1990) deduce a relation from the galactic ratio of nonthermal luminosity to production of radio-emitting supernova remnants; scaling their result to 1.5 GHz yields

$$\nu_{\text{sn}}(\text{yr}^{-1}) \approx \frac{P_{\text{nt}}}{10^{23} \text{ W Hz}^{-1}}, \quad (12)$$

within a factor of 2 agreement. The supernova rates in our models are not very sensitive to our assumptions because the supernovae come principally from the middle of the IMF.

Table 5 lists the starburst model parameters for each of our sample galaxies. These were calculated using the above prescription with a star formation rate that reproduces the observed infrared luminosity L_{FIR} according to equation (3). Also listed are results for two other scaling-law models that adopt differing upper and lower mass limits to the IMF: a “high mass” model with $m_l = m_{\text{sn}} = 8 M_{\odot}$, and an extended IMF model with $m_l = 0.1 M_{\odot}$ and $m_u = 60 M_{\odot}$. Note that the star formation rate varies by nearly a factor of 5 among these prescriptions, but the supernova frequency, varying by less than 50%, is much less sensitive.

Such scaling-law models have been superseded by more sophisticated calculations that use stellar population synthesis to calculate detailed starburst characteristics as a function of time. We have employed the models of Leitherer & Heckman (1995) to make comparable calculations for our LIG sample. The results from their fundamental, constant star formation rate (SFR) model ($\gamma = -2.35$; $m_l = 1 M_{\odot}$; $m_u = 100 M_{\odot}$; $Z = 1-2 Z_{\odot}$) are also shown in Table 5. These results are quite comparable to the global characteristics of the simple parameterized models with similar input. While the more sophisticated models are very powerful in modeling the detailed characteristics of individual systems with extensive observational data sets, the simple calculations appear adequate to provide comparative results for our sample, especially considering the uncertainties in the input parameters.

The starburst models are viable, in the sense that they match the gross observational characteristics of our sample galaxies with parameters that are within range of current expectation. For example, $\Delta t_{*b} \approx 10^8$ yr, equal to the dynamical timescale for galaxy interaction/merger, is a modest fraction of the total starburst lifetime, estimated by the time necessary to exhaust the available store of molecular gas at the inferred star formation rate. Similarly, the upper end of the main sequence produces the appropriate flux of ionizing photons to produce the observed dereddened H α luminosities. This apparent agreement may be fortuitous, however, since the H α luminosities allow neither for internal absorption in a dusty ionized medium, nor for absorption of ionizing photons on dust grains. This consistency is minor comfort, given the number of free parameters and our scant knowledge about the IMF. The principal result is that the LIGs may be modeled with similar plausibility under the starburst paradigm as with AGNs (LSL95). Similar conclusions have been reached by other workers (see Scoville & Soifer 1991; Colina & Perez-Olea 1992; Leitherer & Heckman 1995). In individual cases, more

detailed observations have placed more stringent constraints on the models. For example, in Arp 220, an upper limit on the 2.6 mm continuum (Scoville et al. 1991) may constrain the free-free flux density and thus the ionizing photon flux and upper mass limit $m_u \lesssim 30 M_\odot$. Dynamical mass estimates appear to constrain the lower mass limit, $m_l \gtrsim 5 M_\odot$ (Scoville et al. 1997).

Accepting that starburst models are generally plausible, fundamental questions remain: Under starburst models, what is the origin of the compact VLBI emission and its relationship to the starburst event? Might these be luminous radio supernovae (singly or in clumps)? Might they be a compact massive object fundamentally unrelated to the starburst and the galaxy energetics? Under the AGN model, what is the origin of the VLA-scale radio emission, and why does it produce the same radio-to-infrared ratio q as starbursts? Is the intermediate-scale radio emission the product of a starburst that is the mechanism for fueling the central engine?

6. THE ORIGIN OF THE VLBI EMISSION: RSN VERSUS AGN

Our prejudice at the outset of this research was that compact, high- T_b radio emission is a unique indicator of an AGN core. However, it has become clear in recent years that there exists a distinct class of radio supernovae that exhibit very high radio power (Wilkinson & de Bruyn 1990) and that may, in the extreme, compete as candidates for the compact VLBI emission detected in this study. Given the high expected supernova rate for luminous starbursts from Table 5 above, $0.1 \lesssim v_{sn} \lesssim 2$, our sample galaxies will have frequent supernovae, and it is plausible to suspect that such extreme starbursts will give rise to luminous RSNs *if their dominant energy source is from star formation*. The best studied member of this supernova class is SN 1986J in NGC 891 (Weiler, Panagia, & Sramek 1990), which exhibited a maximum radio power, $\log P_{1.5\text{GHz}}^{1986\text{J}} = 21.15$.³ Even more extreme, a compact variable radio source in the starburst galaxy Mrk 297 (Mrk 297A; LLS92; Yin & Heeschen 1991) has been interpreted as the most luminous RSNs observed to date, with a 1.5 GHz power at maximum, $\log P_{1.5\text{GHz}}(\text{max}) = 21.5$ (W Hz^{-1}).

Only one of the VLBI sources in Table 2 has a VLBI power, $\log P_{\text{VLBI}} \lesssim 21.5$ (W Hz^{-1}), the largest value previously attributed to a luminous RSN *at maximum light*. Seven sources are within a factor of 3 of this value, however, and we must ask whether the luminous RSNs may plausibly exhibit such high radio power. Unfortunately, phenomenological models that can provide an excellent fit to RSN light curves do not constrain the energy budget, because they allow the particle/field energy to scale as an arbitrary fraction of SN shock energy (Chevalier 1982). Physical models of shock acceleration of synchrotron electrons in dense nuclear environments that can provide realistic estimates of RSN luminosities have not yet been developed (see Jones & Kang 1993). We note however that a standard synchrotron model for Mrk 297A implies an equipartition particle/field energy $U_{\text{int}} \approx 4 \times 10^{49}$ ergs (LLS92), which is an uncom-

fortable 4% of the available kinetic energy budget, 10^{51} ergs, allocated to Type II supernovae. Unless a physically new, more energetic class of SN explosion is postulated, we believe that it is reasonable to consider $\log P_{\text{VLBI}} = 21.5$ as the maximum value for a single supernova. In this context, it is worth noting that 70% of SN will have progenitor masses within a factor of 2 of the lower mass limit for SN detonation (i.e., 8–16 M_\odot). Appealing to supermassive stars producing a new class of more powerful supernova would have difficulty reproducing the frequency of VLBI-scale emission. Furthermore, the majority of VLBI sources show complex structure that could not be replicated by a single RSN. We conclude that luminous RSNs cannot, as isolated events, produce the observed VLBI emission. We address the possibility that multiple RSNs may produce the compact, high- T_b emission in § 6.2.

6.1. AGN Source Structure

Another approach to the origin of the compact radio emission is to compare the source structure, inferred principally from the observed visibility curves, with structure expected from AGN or starburst sources. The LIG visibility functions displayed in Figure 1 show a variety of characteristics. The slopes of the visibility curves show a large range, frequently without discernible structure indicating a preferred spatial scale. In some cases there is evidence for separate large and small-scale structures, with high flux densities on short baselines and a constant low flux density level on intermediate and long baselines. Occasionally, hints exist of complicated structure, in the form of extreme departures from a monotonic decline with baseline length. Common to all these curves, however, is the tendency for structure to exist on a variety of scales, with no apparent preferred spatial scale. This inference is borne out by the VLA imaging study. Despite the large difference in observing frequencies, which hampers quantitative comparisons, it is clear that substructure is ubiquitous in these objects on the 0".1 scale as well as on the smaller scales accessible to the VLBI survey. This supports a picture in which material is clumped on all scales between a few parsecs and a few hundred parsecs.

For comparison with the structures observed in the LIGs there is a wealth of VLBI data for AGNs available in the literature. The most comprehensive data set is the Caltech-Jodrell Bank VLBI Survey with 18 cm global VLBI observations of in excess of 100 sources (Polatidis et al. 1995; Thakkar et al. 1995) with supporting VLBI/MERLIN observations at 6 cm and VLA observations at 21 cm (Xu et al. 1995). Although the data are not yet fully interpreted, and visibility functions are not presented for direct comparison with our results, the structural models (maps) presented show a large variety of structures within known AGNs. These range from sources with unresolved cores, with or without jets, through multiple components, to fairly diffuse structures. In many cases structures are present on a variety of spatial scales comparable to the scales of interest in our study. Without doubt our observed VLBI visibility functions and VLA images may be accommodated within the varied ensemble of structures associated with AGNs.

6.2. Starburst Models: Synthetic Visibility Functions with RSNs

It appears impossible for a single powerful Type II RSN to provide the necessary VLBI power. However, there is no

³ We adopt a distance $d = 9.5$ Mpc to NGC 891. NGC 891 is a member of the NGC 1023 Group, which includes NGC 925. An *HST*/Cepheid distance to NGC 925, $d = 9.3 \pm 0.7$ Mpc has recently been measured by Silberman et al. (1996). An independent measurement for NGC 891 based on planetary nebulae, $d = 9.9 \pm 0.8$ Mpc, has been made by Ciardullo, Jacoby, & Harris (1991).

conclusive evidence that the compact milliarcsecond power is provided by a single source. Table 5 indicates a typical supernova rate, $\nu_{\text{sn}} \approx \frac{1}{2} \text{ yr}^{-1}$. If all of these supernovae are radio-luminous with a decay time of a few years, typically 5–20 luminous RSNs could, in principle, contribute to compact, unresolved ($\theta \lesssim 0''.001$) structure and thus to the visibility function at the longest baselines. Here we describe model visibility functions, constructed for compact starbursts dominated (in the radio) by radio supernovae, which we attempt to fit to the observed visibility functions of the VLBI sample galaxies with well-sampled visibility data.

We construct Monte Carlo models that fill a volume of dimension equal to the VLA radio source size (CHYT) with randomly distributed or clustered RSNs that detonate at random intervals, then decay following observed RSN light curves. LLS92 discussed RSNs in this context in some detail; the underlying theory, due principally to Chevalier (1982), has been applied to RSNs by Weiler et al. (1986, 1990). The RSN light curve is interpreted as an optically thick, thermal supernova shell expanding into a dense ambient medium, presumed to be the supergiant progenitor's stellar wind

$$S_\nu \propto \nu^\alpha t^\beta e^{-\tau}, \quad (13)$$

where the spectral index is $\alpha \approx -0.7$, t is the time since detonation, and τ is the optical depth of the shell. As the shell expands it becomes optically thin, producing a radio maximum first at higher frequencies. We ignore the rapid premaximum light phase and adopt

$$S_\nu = \frac{P_\nu(\text{max})}{4\pi d^2} \left(\frac{t - t_0}{3 \text{ yr}} \right)^\beta, \quad (14)$$

where $P(\text{max})$ is the power at maximum light, which is taken to be 3 yr after detonation at $t = t_0$ appropriate to $\nu = 1.67 \text{ GHz}$ (Weiler et al. 1986).

We employ two Type II RSN classes:

1. Standard RSNs: Typical radio supernovae have peak radio powers up to $P_{1.5 \text{ GHz}}(\text{max}) \approx 2 \times 10^{20} \text{ W Hz}^{-1}$. They are generally well fitted by the above model with $\langle \beta \rangle \approx -0.7$ (Weiler et al. 1986). We adopt $P_{1.5 \text{ GHz}}(\text{max}) = 10^{20} \text{ W Hz}^{-1}$ and $\beta = -0.7$ for standard RSNs.

2. Luminous RSNs: We adopt SN 1986J, $P_{1.5 \text{ GHz}}(\text{max}) = 1.4 \times 10^{21} \text{ W Hz}^{-1}$, as a prototype of luminous RSNs. In the case of luminous RSNs the light curve is better fitted with expansion into a thermal absorbing medium, presumed to be the ejected supernova shell, and a nonthermal emitting medium, possibly at the shock interface with the ambient medium (Weiler et al. 1990). The shape of the rise to maximum, and the epoch of maximum light as a function of frequency, are somewhat different from those of standard RSNs, but the light curve from maximum is still well fitted by a power-law expression, but with a steeper decline, $\beta = -1.2$ to -1.4 . Mrk 297A has a similar “best-fit” value of the decline rate, $\beta = -1.3$, although in both SN 1986J and Mrk 297A the decline is irregular and not always monotonically decreasing postmaximum. For our modeling we will adopt $\beta = -1.3$ for luminous RSNs, but let $P(\text{max})$ scale in units of P^{1986J} to provide the best fit to the visibility functions.

We consider two spatial distributions of supernovae: (1) centrally concentrated with a spherically symmetric, Gaussian radial probability distribution; the half-power points of

the spatial distribution are set equal to the FWHM of the deconvolved 8.44 GHz maps of CHYT, and (2) centrally concentrated as in (1), but clustered on parsec scales as might be the case, for example, if starbursts form massive clusters of stars. Clearly, the fact that GMC cores and globular clusters have sizes of a few parsecs provides scientific motivation for considering such clustered models, and the form of the visibility functions indicates that there is significant structure on parsec scales. It is not *sufficient*, however, for the RSNs to be produced by clustered distributions of stars; for the RSNs to appear clustered in the visibility functions, a small number of clumps must contain the majority of RSNs active at a given time. We will return to this point that places substantial constraints on physical attributes of clustered models.

6.2.1. Simple Gaussian Models

In the simple Gaussian model the supernovae are “detonated” randomly within the assumed spatial distribution and at random time intervals, characterized by a supernova frequency ν_{sn} , which may be compared with the supernova frequency calculated in our starburst models in § 5. In a given model all RSNs have a uniform power at maximum, $P_{\text{sn}}(\text{max})$. The supernovae then decay according to the prescribed decay function (eq. [14]) and expand with expansion velocity, $v_{\text{sn}} = 10,000 \text{ km s}^{-1}$. The modeled RSNs are effectively point sources because individual RSNs fade from view before they become significantly extended, particularly for the more distant sources and the more luminous, more rapidly decaying RSN models. The process is continued for 10^3 years to create what is effectively a constant distribution of bright supernovae, with a background population of fainter RSNs and remnants that increase with Δt_{sb}^4 .

The radio supernovae are projected onto the sky plane, then the visibility function is sampled on the u -axis only, relying on circular symmetry and avoiding the complication of a full two-dimensional Fourier transform. The entire process is repeated 500 times and averaged to determine a mean visibility curve and rms variation as a function of baseline length. These curves are then compared with our survey observations. Since the size of the star-forming region is set by the VLA radio diameter measured by CHYT, only two parameters are varied in the “Standard RSN” model: S_{VLBI} and ν_{sn} . For luminous RSN models the RSN power at 18 cm is an additional fitted parameter. Although S_{VLBI} is an “observed” quantity, it is only estimated in Table 2 because of the fluctuations in the visibility function on long baselines. In general the value in Table 2 may be considered an upper limit. In the models, S_{VLBI} is the average of a large number of individual calculations, and an acceptable model may have a value of S_{vlbi} that differs from that in Table 2 by as much as a factor of 2.

Figure 7 shows a suite of synthetic visibility functions for RSN models at a distance of 100 Mpc, with supernova rate calculated to produce a VLBI flux density $S_{\text{vlbi}} = 2 \text{ mJy}$.

⁴ We do not model the diffuse background emission for two reasons: (1) We expect that the adopted RSN light curves are accurate until individual RSNs become undetectable (~ 10 – 20 yr), but must fail as the sources evolve into *remnants* and shock-generated cosmic rays. (2) It is clear from previous work on the VLA-scale radio emission and the radio-infrared correlation (Condon et al. 1991a; Bica & Helou 1990) that the relationship between the supernova sources and the relativistic plasma that produces the “extended” emission is a complex one, well beyond the level of the simple models that may explain the VLBI-scale emission.

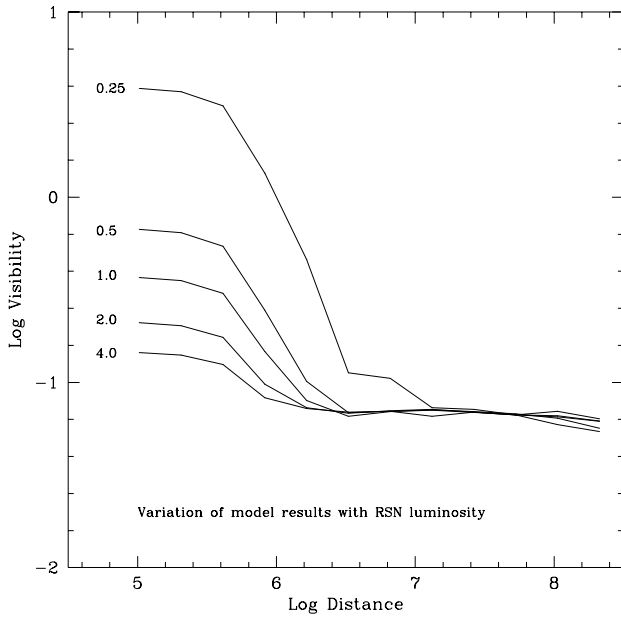


FIG. 7a

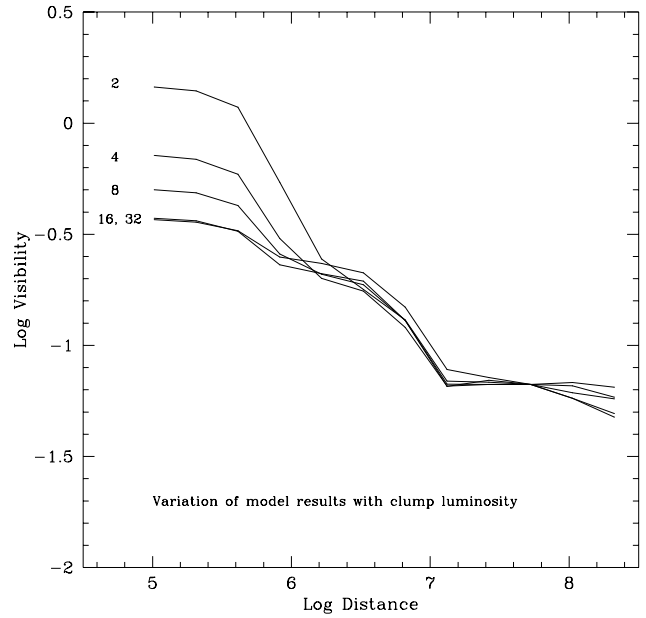


FIG. 7b

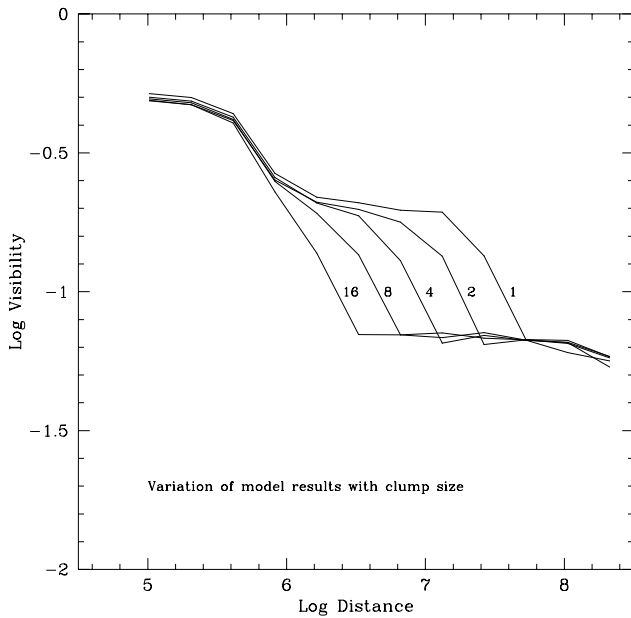


FIG. 7c

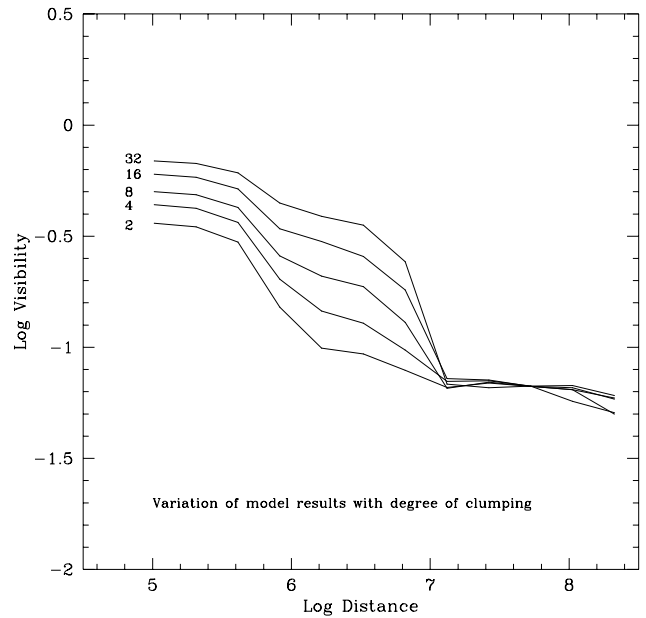


FIG. 7d

FIG. 7.—Synthetic visibility functions for RSN/starburst LIG models. The galaxy is assumed to be at a distance of 100 Mpc, with supernova rate calculated to produce a VLBI flux density $S_{\text{VLBI}} = 2$ mJy and total flux density 30 mJy. (a) Variation of the visibility function with RSN luminosity for a Gaussian (nonclustered) model. In this case the supernova frequency decreases from $\nu_{\text{sn}} = 8 \text{ yr}^{-1}$ at $P_{\text{sn}} = 0.25 \times P^{1986J}$ to 0.09 yr^{-1} at $P_{\text{sn}} = 4.0 \times P^{1986J}$. (b–d) Clustered models. The fiducial model has eight supernovae per clump, $N_{\text{sn}} \text{ cl}^{-1} = 8$, detonated simultaneously with $P_{\text{cl}} = 8 \times P^{1986J}$, hence $P_{\text{sn}} = 1.0 \times P^{1986J}$, in clumps with size $d_{\text{cl}} = 4.0$ pc. (b) Effect of varying clump power P_{cl} . In this case the number of RSNs per clump is kept constant ($N_{\text{sn}} \text{ cl}^{-1} = 8$), thus the individual RSN power scales with clump power. (c) Effect of varying the clump size, $d = 1$ –16 pc with the other parameters kept at their fiducial values and a typical supernova frequency $\nu_{\text{sn}} \approx 0.8 \text{ yr}^{-1}$. (d) Effect of the degree of clumping: clump luminosity increases as number of RSNs per clump increases, maintaining constant RSN luminosity $P_{\text{sn}} = P^{1986J}$. Thus, we have a series of models with similar RSNs that get progressively more clumpy in their spatial distribution. In this case the supernova frequency increases with $N_{\text{sn}} \text{ cl}^{-1}$ and P_{cl} from $\nu_{\text{sn}} = 0.08 \text{ yr}^{-1}$ at $N_{\text{sn}} \text{ cl}^{-1} = 2$ to $\nu_{\text{sn}} = 13 \text{ yr}^{-1}$ at $N_{\text{sn}} \text{ cl}^{-1} = 32$. The implied number of “visible” clumps that have detonated in the last 20 years scales from 0.8 to 8 over this range. The curves are labeled by $N_{\text{sn}} \text{ cl}^{-1} = 2$ –32.

Figure 7a shows five Gaussian (nonclustered) model visibility functions with RSN peak luminosities $P_{\text{sn}}(\text{max}) = 0.25, 0.50, 1.0, 2.0, 4.0 \times P^{1986J}$. The family of curves converges at long baselines owing to the requirement of matching the targeted flux density $S_{\text{VLBI}} = 2$ mJy. S_{VLBI} is determined by the RSN power, $P_{\text{sn}}(\text{max})$, and the number of RSNs contrib-

uting to the visibility function that is set by ν_{sn} . These two parameters scale inversely, so that as the radio power of the supernovae increase, the supernova rate necessary to provide the observed flux density decreases from $\nu_{\text{sn}} = 8 \text{ yr}^{-1}$ at $P_{\text{sn}} = 0.25 \times P^{1986J}$ to 0.09 yr^{-1} at $P_{\text{sn}} = 4.0 \times P^{1986J}$.

At shorter baselines the visibility function is characterized by a shoulder at u - v spacings from 10^5 to $3 \times 10^6 \lambda$, corresponding to spatial scale (10–100 pc at $D = 100$ Mpc) for which multiple RSNs fall within a single interferometer lobe spacing. The visibility then falls off to a level that is determined by the maximum flux density per RSN and the RSN decay rate, which determines the number of individual RSNs that contribute to the flux density.

Because of the power-law nature of the RSN light curve, there is no true “characteristic timescale” for RSN decay. For the luminous RSN prescription, newly detonated supernovae ($t - t_0 < 10$ yr) contribute about 36% of the total flux density, whereas 30% is contributed from supernovae between 10 and 100 years old, and supernovae 100–1000 years old contribute 17%. We can estimate the number of RSNs that are individually visible at a particular time as the number of RSNs with $P \gtrsim 0.1 P_{\max}$. This is the number of sources that a sensitive VLBI imaging experiment with a typical dynamic range of 10 would detect as individual point sources. For luminous RSNs, decay to 10% of maximum occurs in approximately 20 yr, so that the number of “visible” supernovae may be considered to be about 20 times the supernova frequency, i.e., 160 visible RSNs for $P_{\text{sn}} = 0.25 \times P^{1986J}$ decreasing to about 2 at $P_{\text{sn}} = 4.0 \times P^{1986J}$.

The observed visibility functions in Figure 8 do not generally resemble those in Figure 7a. They are more featureless without the characteristic shoulder at longer scales. This suggests that a model with more structure at intermediate scales (1–10 pc) might match the data. We therefore investigate models in which the RSNs and resulting emission are clustered on parsec scales below.

6.2.2. Clustered Models

In the clustered model, clumps of radio power P_{cl} are distributed according to the same Gaussian radial probability distribution, with each clump subdivided into n_{sn} individual supernovae of power, $P_{\text{sn}} = P_{\text{cl}}/n_{\text{sn}}$. Clump sizes d_{cl} were allowed to range between 1 and 10 pc. The clump is treated as a cube, d_{cl} on a side, with one axis along the line of sight. This simplification will provide the desired power at the appropriate u - v distance in the visibility function, but will not reproduce appropriate substructure. Within the limitations of the observed visibility data and the Monte Carlo models, this is a minor effect. The individual supernovae n_{sn} are then distributed randomly within the clump, and all the supernovae in a clump are detonated simultaneously with common power. This will induce greater variance between individual models than a more realistic staggered detonation model might yield. If the presence of clumping is to produce significant structure in the visibility function, the supernovae visible at a given time must be concentrated in a small number of clumps, either by having a large number of clumps, with each lit up only briefly, which is what is actually calculated, or by concentrating all the star formation into a small number of clumps. For example, the limiting case of models with high spatial clustering into a large number of clumps with a single “visible” RSNs per clump will be indistinguishable from the unclustered Gaussian models in their radio emission.

The clustering introduces power on intermediate u - v scales, which, depending upon the clump size, yields a more nearly featureless, power-law visibility function than the Gaussian models. Clustered models are shown in Figure

7b–7d. The fiducial model has eight supernovae per clump, $N_{\text{sn}} \text{ cl}^{-1} = 8$, detonated simultaneously with $P_{\text{sn}} = 1.0 \times P^{1986J}$, hence $P_{\text{cl}} = 8 \times P^{1986J}$, in clumps with size $d_{\text{cl}} = 4.0$ pc. The effect of varying clump power P_{cl} is shown in Figure 7b; in this case the number of RSNs per clump is kept constant ($N_{\text{sn}} \text{ cl}^{-1} = 8$), thus the individual RSN power increases linearly with clump power. Figure 7b shows a similar effect to that in Figure 7a because the RSN power is the key parameter that is changing.

Figure 7c shows the effect of varying the clump size $d = 1$ –16 pc with the other parameters kept at their fiducial values. These models have a supernova frequency $\nu_{\text{sn}} \approx 0.8 \text{ yr}^{-1}$; thus 16 RSNs in two clumps have recently detonated. At largest clump size $d_{\text{cl}} = 16$ pc the clumps are sufficiently large that they show little difference from the Gaussian models. As the clump size decreases, however, power is introduced at longer and longer baselines, and the model curves begin to resemble the observed visibility functions.

Finally, Figure 7d shows the effect of the degree of clustering; clump luminosity is adjusted as number per clump is varied, maintaining constant RSN luminosity $P_{\text{sn}} = P^{1986J}$. The curves are labeled by $N_{\text{sn}} \text{ cl}^{-1} = 2$ –32. Thus, we have a series of models with similar RSNs that get progressively more clumpy in their spatial distribution. In this case the supernova frequency increases with $N_{\text{sn}} \text{ cl}^{-1}$ and P_{cl} from $\nu_{\text{sn}} = 0.08 \text{ yr}^{-1}$ at $N_{\text{sn}} \text{ cl}^{-1} = 2$ to $\nu_{\text{sn}} = 13 \text{ yr}^{-1}$ at $N_{\text{sn}} \text{ cl}^{-1} = 32$. The implied number of “visible” clumps scales from four to 40 over this range.

Because the models represent the average of a large number of individually calculated visibility functions, fluctuations due to constructive and destructive interference of individual components are averaged out, resulting in models that are smoother than the observed visibility functions on the longer baselines. Comparison of individual model runs suggests that an “error bar” of approximately 0.5 dex effectively represents the rms fluctuations for comparison with the observations.

In practice, the models are run to match the characteristics of an individual source. The average correlated flux density on long baselines is specified to the model, either the standard RSN model is specified or a value of $P_{\text{sn}}(\text{max})$ in terms of P^{1986J} is selected. The model then determines an RSN frequency necessary to reproduce the observed correlated flux density at u - v distances in excess of $10^6 \lambda$. No formal goodness of fit is calculated, but the models are tightly constrained. As described in § 5, the supernova rate varies over a very limited range for starburst models. Values of $\nu_{\text{sn}} > 2 \text{ yr}^{-1}$ would appear to be excessive. Furthermore, at large ν_{sn} the models are not a good fit to the observed visibilities because the large number of contributing RSNs approximate a smooth source and underpredict the correlated flux density on the longer baselines.

6.2.3. Results of Model Fits

There are 11 galaxies with adequately sampled visibility functions such that we attempted RSN model fits to the data. Considerable care must be exercised in comparing the models to the observed visibility functions, because the model averages substantially smooth the visibility functions on the longer baselines. Furthermore, the models contain only emission from relatively young RSNs that fade before they become significantly extended. The observed visibility functions may include flux density from extended emission that is not produced in our models. For this reason we do

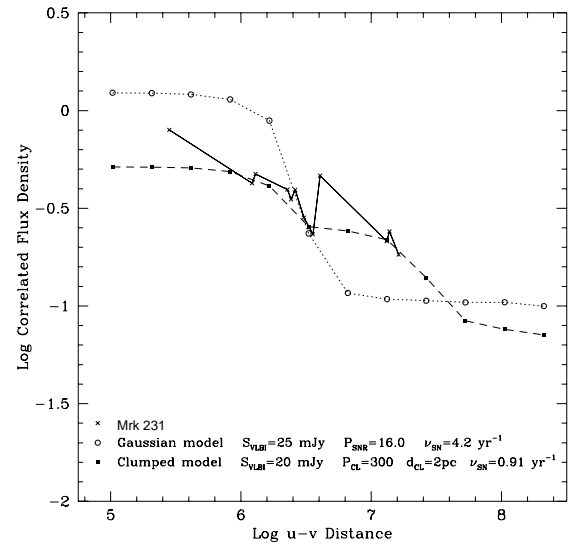
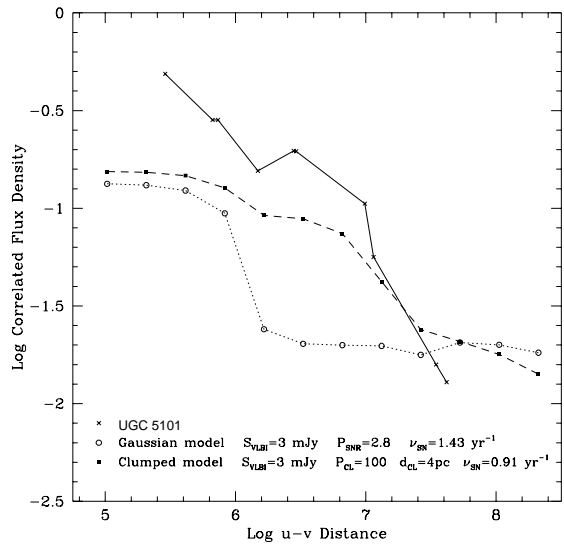
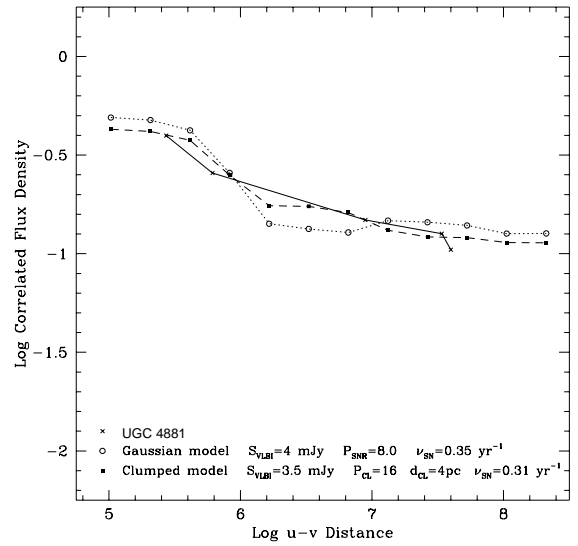
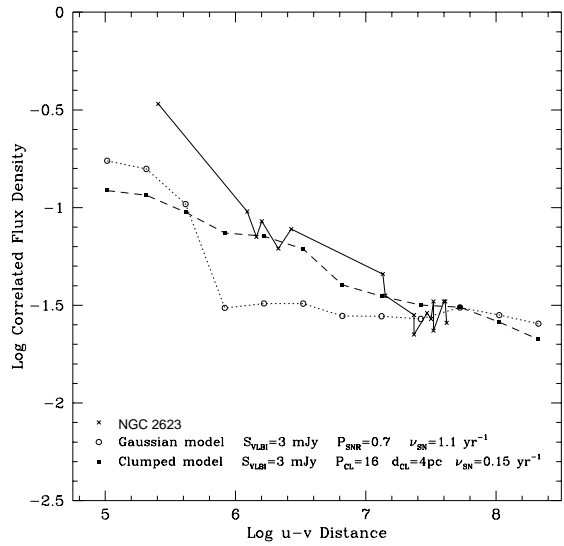
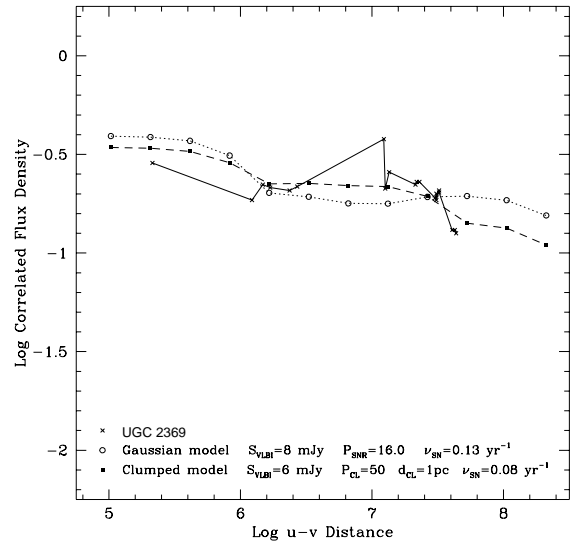
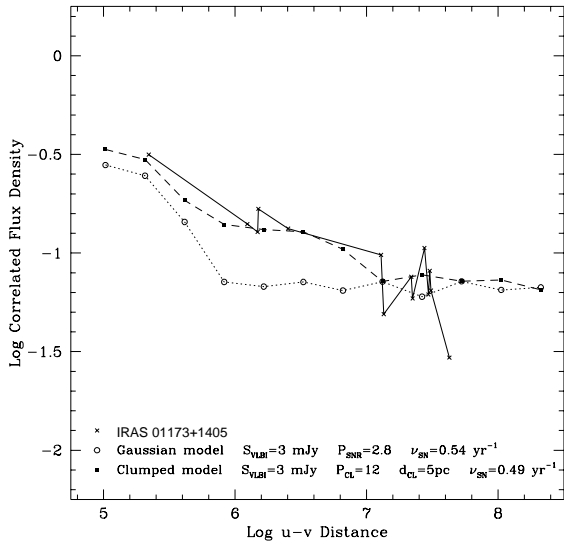


FIG. 8.—Synthetic visibility function fits for 11 LIGs; model parameters are given in Table 6. In each case the observed visibility function is the heavy solid line; the dotted curve is our “best-fit” Gaussian (nonclustered) model; the dashed curve represents the best clustered model. Because many individual visibility functions are averaged to produce the models, the models are smoother on long baselines compared to the actual visibility functions. A typical rms fluctuation of about 0.5 dex is appropriate for comparison of model with observation.

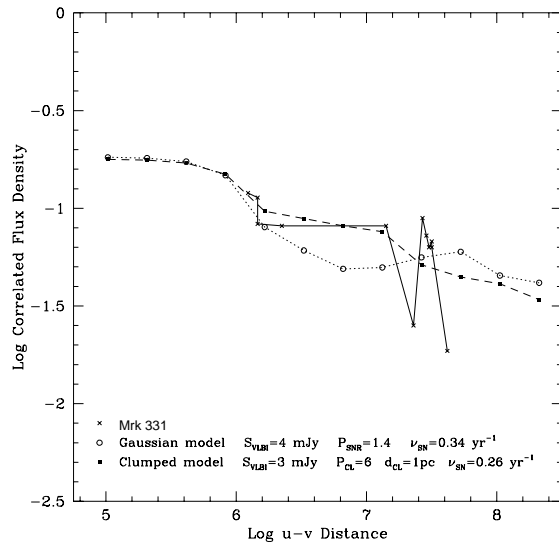
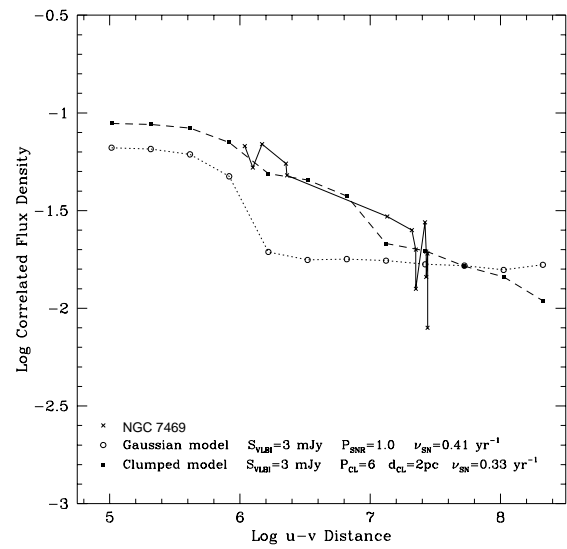
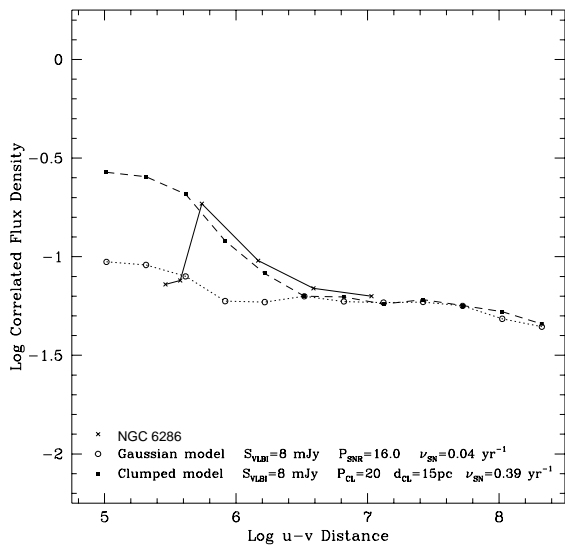
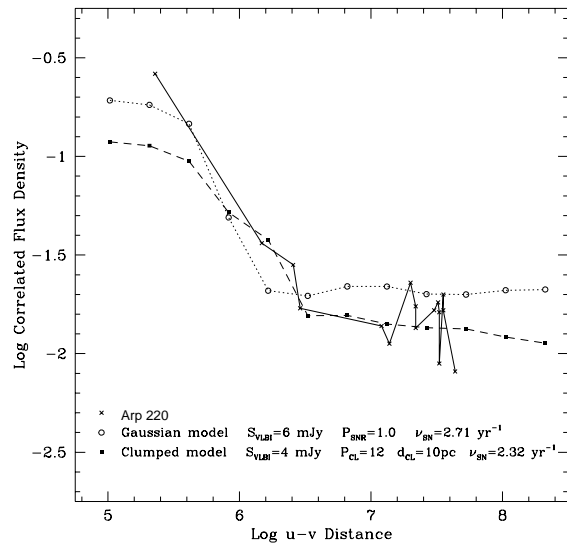
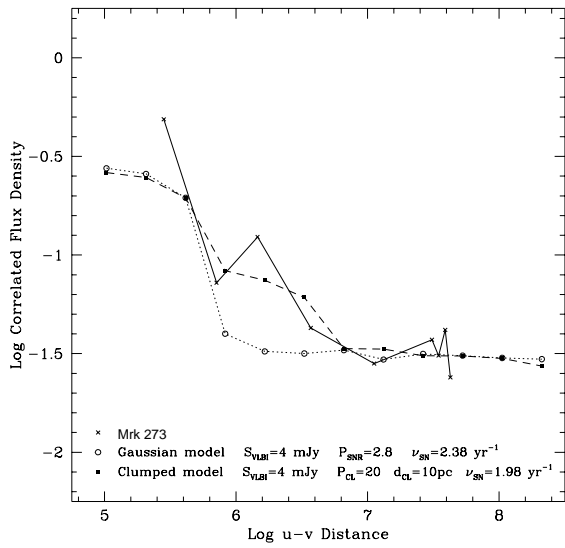


FIG. 8—Continued

not exclude models that underestimate the correlated flux density on short baselines. The best-fit models, overplotted on the observed visibility functions, are shown in Figure 8, and the model numerical results, compared with the “observational” data, are shown in Table 6. As described below, these are all luminous RSN models; in no case does a model with standard RSNs provide an adequate fit.

Table 6, column (2) gives the VLBI flux density from Table 2; this will generally be an upper limit to the model VLBI flux density, which corresponds only to the longest baselines. Column (3) lists the supernova frequency $\nu_{\text{sn}}^{\text{FIR}}$ from Table 5; that is, the supernova frequency estimated by a starburst model that reproduces the observed L_{FIR} . The Gaussian model parameters are given in columns (4)–(7); these are, respectively, the VLBI flux density for the model, S_{VLBI} , as described above, the power of each of the model RSNs in units of RSN 1986J, $P_{\text{sn}}^{1986\text{J}}$, the model supernova frequency ν_{sn} , and the ratio of the supernova frequency in our Gaussian model fit to that calculated in the starburst model. In column (8) we give a subjective estimate of the quality of the model fit, based entirely on the ability of the best-fit model to reproduce the visibility data (and ignoring plausibility of the model parameters). These estimates are coded: a = “acceptable,” m = “fails in the midrange, otherwise acceptable,” l = “fails at low u - v distance, otherwise acceptable,” p = “poor.” As described in § 6.2.1 above, a rough estimate of the number of supernovae visible at a given time may be obtained by multiplying the model ν_{sn} by 20. This is the number of RSNs with flux densities greater than 10% of the flux density at maximum light that, for the adopted decay rate, is the approximately the number of supernovae occurring within the last 20 years.

The results of the clustered fits are shown in columns (9)–(17). Columns (9)–(12) provide the VLBI flux density, the individual RSN power at maximum, the supernova frequency, and the supernova ratio as in the uniform Gaussian models. Column (13) lists the total power of an RSN clump, $P_{\text{cl}}^{1986\text{J}}$, in units of RSN 1986J; column (14) gives N_{cl} , the number of clumps that have detonated in the last 20 years; column (15) lists the number of supernovae per clump, $N_{\text{sn}} \text{cl}^{-1} = n_{\text{sn}} = P_{\text{cl}} P_{\text{sn}}^{-1}$ as described above; column (16) lists the clump diameter in parsecs; column (17) lists our assessment of the quality of fit.

There are no acceptable fits using standard RSNs. The large number of RSNs required in these models to provide the flux density effectively wash out any structure in the

visibility function. Furthermore, the models require supernova frequencies many times the supernova frequency predicted by the starburst models. We conclude that starbursts with standard RSNs are incapable of producing the radio power and structure of the LIGs.

Among the luminous RSN models, none of the non-clustered Gaussian models are fully acceptable representations of the observed visibility functions. Figure 8 and Table 6 show that most Gaussian fits have too little correlated flux density on intermediate baselines (midrange). In one case, Arp 220, the Gaussian model provides a marginally acceptable fit, depending upon the appropriate correlated flux density on longest baselines, where the observed visibility function is particularly variable. The failure of many of the models at baselines corresponding to a few parsecs at the typical LIG distances suggested that introducing clumps on such scales would provide a better fit to the visibility function. As expected, the clustered models are generally a better fit. In all cases, the introduction of clustering improves the visibility function fit and/or relieves other constraints such as RSN luminosity.

In summary:

1. Arp 220 is the only system that may plausibly be explained by a starburst/RSN model without significant clustering. Since making these calculations, we have obtained strong evidence from VLBI imaging observations of Arp 220 that multiple, luminous RSNs supply the compact, milliarcsecond-scale radio emission from that object (Smith et al. 1998). The structural characteristics of the Arp 220 image are a near perfect match to the starburst model calculated in § 5 with radio supernovae having luminosities and decay times comparable to RSN 1986J. This result is consistent with the recent *ISO* spectrophotometric observation that Arp 220 does not exhibit high-excitation midinfrared features expected from a hard ionizing radiation field (Sturm et al. 1996).

2. For eight systems we judge that the clustered RSN models provide a reasonable fit, taking into consideration the overall model fit to the general distribution of visibilities, and also the correlated flux density on long baselines, and the total flux density on scales smaller than 0'25 owing to RSNs. These include Arp 220, plus 01173+1405, NGC 2623, UGC 4881, Mrk 273, NGC 6286, NGC 7469, and Mrk 331. The required luminosities of the RSNs, particularly for UGC 4881 and NGC 6286, are uncomfortably

TABLE 6
STARBURST/RSN VISIBILITY FUNCTION MODELS

SOURCE (1)	GAUSSIAN MODELS							CLUMPED MODELS								
	S_{VLBI} (mJy) (2)	$\nu_{\text{sn}}^{\text{fir}}$ (yr^{-1}) (3)	$S_{\text{VLBI}}^{\text{gauss}}$ (mJy) (4)	$P_{\text{sn}}^{1986\text{J}}$ (5)	$\nu_{\text{sn}}^{\text{gauss}}$ (yr^{-1}) (6)	S/N (7)	Fit (8)	$S_{\text{VLBI}}^{\text{clump}}$ (mJy) (9)	$P_{\text{sn}}^{1986\text{J}}$ (10)	$\nu_{\text{sn}}^{\text{clump}}$ (yr^{-1}) (11)	S/N (12)	$P_{\text{cl}}^{1986\text{J}}$ (13)	N_{cl} (14)	$N_{\text{sn}} \text{cl}^{-1}$ (15)	d_{cl} (pc) (16)	Fit (17)
01173+1405.....	7.0	0.47	3.0	2.8	0.54	1.15	m	3.0	4.0	0.49	1.05	12	3.2	3	5	a
UGC 2369.....	15.0	0.44	8.0	16.0	0.13	0.30	p	6.0	25.0	0.08	0.18	50	0.8	2	1	l
NGC 2623.....	9.0	0.40	3.0	0.7	1.10	2.75	p	3.0	4.0	0.15	0.38	16	0.8	4	4	l
UGC 4881.....	4.0	0.55	4.0	8.0	0.35	0.63	ml	3.5	8.0	0.31	0.56	16	3.0	2	4	a
UGC 5101.....	28.0	1.15	3.0	2.8	1.43	1.24	p	3.0	5.0	0.94	0.82	100	1.0	20	4	p
Mrk 231.....	115	3.04	25.0	16.0	4.20	1.38	p	20.0	30.0	0.91	0.30	300	1.8	10	2	a
Mrk 273.....	16.0	1.49	4.0	2.8	2.38	1.60	p	4.0	3.3	1.98	1.33	20	6.6	6	10	a
Arp 220.....	10.5	1.75	6.0	1.0	2.71	1.55	m	4.0	1.0	2.32	1.33	12	3.8	12	10	a
NGC 6286.....	13.0	0.25	8.0	16.0	0.04	0.16	m	8.0	5.0	0.39	1.57	20	2.0	4	15	l
NGC 7469.....	12.0	0.35	3.0	1.0	0.41	1.16	p	3.0	1.7	0.33	0.94	10	1.0	6	2	a
Mrk 331.....	7.5	0.25	4.0	1.4	0.34	1.34	m	3.0	2.0	0.26	1.04	6	1.8	3	1	a

high. In these cases P_{sn} is a factor of 2 or more greater even than that of Mrk 297A, assuming that this source is indeed a radio supernova.

3. Three systems, UGC 2369, UGC 5101, and Mrk 231, stand out as having extraordinary solutions: very large clump luminosity, small clump size, and high-RSN luminosity. We judge the best RSN model fits to be unreasonable either because the visibility function is not well fitted (UGC 5101) or because the required RSN luminosity is too great by more than an order of magnitude (UGC 2369 and Mrk 231). Furthermore, in the case of UGC 5101 the number of RSNs per clump is excessive. In our estimation, these galaxies *must* harbor AGN radio cores. VLBI imaging of three systems (Lonsdale et al. 1998b) confirms this hypothesis for Mrk 231 and UGC 5101 and suggests that the Seyfert 1.5 galaxy, NGC 7469, also harbors a radio AGN. Mrk 231, UGC 5101, and NGC 7469 are the highest excitation galaxies in the sample and would be the chief AGN candidates based upon other considerations, including emission-line spectrum and radio-infrared characteristics.

4. The uniform characteristic of the good RSN model fits is that they require multiple, luminous RSNs like SN 1986J to fit the LIG visibility functions regardless of the assumed supernova frequency. Even allowing the supernova frequency to exceed our starburst model calculations by large factors, normal RSNs cannot reproduce the observed visibility functions because the number of normal RSNs required to produce the observed flux density cannot reproduce the observed structure.

5. The acceptable solutions suggest that RSNs are likely to be clustered on parsec scales. As described above, the requirement that spatial clustering contribute structure in the visibility function at intermediate scales implies that the supernova-generated radio emission be concentrated in a small number of clumps. This is apparent from Table 6, which shows that the acceptable models typically have 1–4 clumps visible at a given time.

There are a continuum of physical scenarios that satisfy the clustering required by our visibility models, but all are subject to some physical difficulty. At the extremes are models that may have many clumps, but that go through brief periods of activity so that only a few are “visible” at any time, and models in which all of the activity is actually confined to a small number of very massive clumps. In the case actually calculated, the RSNs within a clump detonate within the decay time of the light curve (10–20 yr) with new clumps detonating every few years. For example, IRAS 01173+1405 requires approximately three clumps with typical maximum power $P_{\text{cl}} \approx 12 P^{1986\text{J}}$ to reproduce the midrange visibility function. With supernova frequency $\nu_{\text{sn}} = 0.5 \text{ yr}^{-1}$ this case requires several RSNs to detonate in a 5 pc sized clump over a couple of decades—a sort of a “chain reaction” of supernovae. In this case there may be a large number of star clusters, but only a few clusters visible in the radio at this epoch.

At the other extreme is the case in which a large fraction of the stars with $m \gtrsim 8 M_{\odot}$ that have formed within the last 30 million years are clustered into a small number of clumps that produce, according to our prescription, an asymptotic radio power from RSN

$$P_{\text{cl}}(t \rightarrow \infty) = \int_{t=3 \text{ yr}}^{t=\infty} \frac{\nu_{\text{sn}}}{N_{\text{cl}}} P_{\text{sn}}(t) dt = 10 \frac{\nu_{\text{sn}}}{N_{\text{cl}}} P_{\text{sn}}(\text{max}). \quad (15)$$

In this case, if there are three active “superclusters” in IRAS 01173+1405, each will have a supernova frequency of about 0.16 yr^{-1} with about three “visible” RSNs and power $P_{\text{cl}} \approx 6 P^{1986\text{J}}$. In this scenario about half the observed flux density comes from individually visible RSNs and about half from the background of “old RSNs” ($t - t_0 \gtrsim 20 \text{ yr}$). At the extreme these clusters must be very massive; with a star formation rate of $30 M_{\odot} \text{ yr}^{-1}$, each cluster in IRAS 01173+1405 will have a mass in excess of $10^7 M_{\odot}$.

Whether external influences can trigger chain reactions of supernovae or whether such compact starbursts can be clustered into even more compact clumps with such high masses are challenging theoretical questions. We must regard the extreme models above as implausible, but there is probably some intermediate range of parameters that will provide the requisite clustering without straining plausibility. For example, the constraint on clump mass may be considerably relaxed if only the massive stars are clustered in a version of bimodal star formation.

Since we have concluded that only very luminous RSN models can reproduce the visibility data for 11 galaxies, it is worth asking whether any of the other galaxies in our sample (i.e., those with sparse VLBI detections or upper limits to S_{vibi}) have limits on compact, VLBI-scale flux density ($S_{\text{vibi}}^{\text{max}}$ in Table 1) that would be exceeded by luminous RSNs at the calculated supernova rate. In fact, the rest of our sample is fully consistent with the inference that compact, luminous starbursts are dominated by luminous RSNs on milliarcsecond scales.

7. CONCLUSIONS

To summarize the conclusions of this work:

1. Luminous IR galaxies have radio emission that exhibits structure on a large range of scales, typically a few milliarcseconds to several tenths of an arcsecond.

2. The VLBI power in LIGs is weakly correlated with infrared luminosity, total 1.49 GHz radio power, and molecular gas mass. These correlations suggest physical relationships that may be interpreted in terms of starburst or hybrid (starburst plus AGN) models.

3. Given the wealth of structures associated with compact, nonthermal radio emission in AGNs, the observed radio data are easily accommodated by AGN models. Combined with the analysis of LSL95, a plausible case may be made for LIGs as dust-enshrouded AGNs.

4. Starburst models for LIGs are extreme, with very high star formation rates and luminous energy densities, but plausible in terms of providing the FIR luminosity and other global characteristics of LIGs. Simple modeling infers star formation rates in the range $15\text{--}200 M_{\odot} \text{ yr}^{-1}$ and an associated supernova frequency $\nu_{\text{sn}} \sim \frac{1}{2}\text{--}2 \text{ yr}^{-1}$.

5. Starburst-generated radio supernovae may be responsible for the compact, milliarcsecond-scale radio structures in many, but not all, of our LIG sample galaxies. Notable exceptions are Mrk 231 and UGC 5101. Models that adequately reproduce the 18 cm LIG visibility functions require multiple, highly luminous radio supernovae.

6. In most successful starburst/RSN models the RSNs must detonate in clumps of scale 2–10 pc, and the supernovae active at a given time must be concentrated into a small number of clumps.

The firm conclusion from this work is that, in those

systems dominated by starburst activity, nearly every supernova explosion results in a luminous radio supernova, with power comparable to or greater than RSN 1986J. Evolutionary models of the compact and extended radio emission from LIGs (Perez-Olea & Colina 1995) reach similar conclusions, under the assumption that the extended radio emission is dominated by the remnants of the luminous RSN producing the compact emission. As described above, reasonable choices for the IMF in starburst galaxies will lead to supernovae with intermediate mass progenitors, so it does not appear plausible to appeal to a new supernova mechanism (e.g., from a supermassive star) that provides a greater store of kinetic energy to accelerate particles and amplify magnetic field in the LIGs. The form of the light curves (Weiler et al. 1990) suggests that the external medium into which the plasma expands may be somewhat different in luminous RSNs than that for standard RSNs, in that a dense ambient medium may be combined with a synchrotron-emitting medium. Still, the densities inferred for the compact star formation regions in LIGs are similar to those for GMCs and for the winds postulated to emanate from the RSN progenitor. Recent work suggests that the geometry of the molecular regions may be the most significant environmental difference (Scoville et al. 1997) with the warm molecular material confined to thick disklike structure in the compact LIGs. In this case, it is possible that stronger, more highly ordered magnetic fields may provide the conditions appropriate for such luminous RSNs. Polarization observations would be a useful discriminant.

For some time it has seemed likely that active star formation and AGN activity coexist in luminous IR galaxies; the question is to assess the relative contribution of each form of activity to the energetics, and to determine from the sample systematics whether, as appears likely, there is a physical relationship between the starburst and AGN, or perhaps an evolutionary progression from one to the other. LSL95 used the compact radio-infrared characteristics of our sample to establish plausibility that AGN activity could be responsible for the bulk of the luminosity in our LIG sample. The starburst/RSN models presented here provide a similar case for starburst activity.

Until our imaging observations of Arp 220 (Smith et al. 1998), we had considered the requirement that LIGs exhibit multiple, extremely luminous RSNs at the rate of order 1 yr^{-1} to be sufficiently extreme that the existence of AGN cores remained the most likely interpretation of the VLBI observations. AGN radio cores are almost certainly present in UGC 2369, Mrk 231, UGC 5101, and NGC 7469, but multiple, luminous RSNs are with equal certainty present in Arp 220. Thus, the RSN models for the other systems, most with lower supernova frequency than Arp 220, must be considered quite plausible. With recent evidence that active star formation is occurring via formation of globular clusters or “super star clusters” (Ho 1996) the clumping suggested by our RSN models may possibly be accommodated. The range of clump size, 2–10 pc is well within the range of core radii for Galactic globular clusters, $r_c \sim 0.2\text{--}15 \text{ pc}$ (Peterson & King 1976).

In two systems, Arp 220 and Mrk 231, there is sufficient evidence to point to a dominant overall energy source, starburst for the former, AGN for the latter. Our evidence suggests that NGC 7469 houses an AGN radio core, but this Seyfert 1.5 galaxy also shows a circumnuclear starburst (Wilson et al. 1991; Miles, Houck, & Hayward 1994; Mazzarella et al. 1994) that is likely to dominate at mid-FIR wavelengths (Jones et al. 1997) and thus provide the dominant energy source. If we assume that all LIGs with acceptable starburst fits are indeed starbursts, a supposition that is by no means proven, we have potentially six starburst systems, three possible hybrid/intermediate systems, and one quasar. A starburst-AGN evolutionary interpretation of such a picture would suggest that the starburst phase is relatively long lived and that the radio AGN “turns on” significantly before the AGN dominates at other wavelengths, perhaps as the late-stage starburst begins to fuel the coalescing central compact object (Norman & Scoville 1988) or the supernovae interact with the nascent AGN (Perry & Dyson 1985). Numerical simulations of mergers like those believed to give rise to LIGs suggest that the onset of the starburst occurs relatively late in the merger process (Mihos & Hernquist 1996), $\tau \sim 10^8 \text{ yr}$, and our results suggest that the starburst may carry on for another 10^8 yr as the nuclei merge and an AGN forms. Once the AGN fully turns on, it must shed its shroud of dust relatively quickly, perhaps extinguishing the star formation in the process, as must be the case to account for the large store of molecular gas in Mrk 231, the only true dust-enshrouded quasar in the above picture.

Much work remains to be done to establish the nature of the relationship between the starburst and AGN activity in LIGs. Our statistical analysis of the LIG sample demonstrates that the physical relationship or evolutionary sequence is not straightforwardly evident from the global sample characteristics, but must be elucidated from careful study of individual objects. Further VLBI maser and continuum imaging observations, as well as mid-IR imaging and spectroscopy are planned for this sample.

The authors wish to acknowledge Joe Mazzarella for helpful discussions of optical spectra and for providing tabulated data on our sample galaxies. We have benefited from illuminating discussions with Dave Sanders and Wayne Stein. We are indebted to an anonymous referee for suggesting a number of ways to clarify the discussion. Thanks to Barry Madore for pointing us to distance information for the NGC 1023 Group, to the staff of Lick Observatory for support of optical observations, and to Haystack Observatory for hospitality. H. E. S. wishes to express deep gratitude to IPAC for providing continued support as a home away from home. This project has benefited from the use of the NASA Extragalactic Database (NED) supported at IPAC by NASA. IPAC/JPL is supported by NASA. Haystack is supported by the NSF via NEROC. Support of this project at the University of California at San Diego has been provided by the NSF under grant AST 93-19895.

REFERENCES

- Armus, L., Heckman, T., & Miley, G. 1989, *ApJ*, 347, 727
 Baan, W., & Haschick, A. 1996, *ApJ*, 454, 745
 Baldwin, J. A., Phillips, M. M., & Terlevich, R. 1981, *PASP*, 93, 5
 Bica, M. D., & Helou, G. 1990, *ApJ*, 362, 69
 Bryant, P. M., & Scoville, N. Z. 1996, *ApJ*, 457, 678
 Chevalier, R. A. 1982, *ApJ*, 259, 302
 Chini, R., Krugel, E., & Steppe, H. 1992, *A&A*, 255, 87
 Ciardullo, R., Jacoby, G., & Harris, W. 1991, *ApJ*, 383, 487
 Colina, L., & Perez-Olea, D. 1992, *MNRAS*, 259, 709
 Condon, J. J., Anderson, M. L., & Helou, G. 1991a, *ApJ*, 376, 95

- Condon, J. J., Huang, Z.-P., Yin, Q. F., & Thuan, T. X. 1991b, *ApJ*, 378, 65 (CHYT)
- Condon, J. J., & Yin, Q. F. 1990, *ApJ*, 357, 97
- Diamond, P., Lonsdale, C. J., Lonsdale, C. J., & Smith, H. E. 1998, *ApJ*, submitted
- Diamond, P. J., Norris, R. P., Baan, W. A., & Booth, R. S. 1989, *ApJ*, 340, L49
- Granato, G. L., & Danese, L. 1994, *MNRAS*, 268, 235
- Granato, G. L., Danese, L., & Franceschini, A. 1996, *ApJ*, 460, L11
- Ho, L. C. 1996, in *Starburst Activity in Galaxies*, ed. J. Franco, R. Terlevich, & G. Tenorio-Tagle, *Rev. Mexicana Astron. Astrofis.*, in press
- Isobe, T., Feigelson, E. D., & Nelson P. I. 1986, *ApJ*, 306, 490
- Jones, B., Puetter, R., Smith, H. E., Stein, W., & Wang, M. 1998, in preparation
- Jones, T. W., & Kang, H. 1993, *ApJ*, 402, 560
- Leitherer, C., & Heckman, T. 1995, *ApJS*, 96, 9
- Lonsdale, C. J., Diamond, P., Smith, H. E., & Lonsdale, C. J. 1994, *Nature*, 370, 117
- . 1998, *ApJ* submitted
- Lonsdale, C. J., Lonsdale, C. J., Diamond, P. D., & Smith, H. E. 1998, in preparation
- Lonsdale, C. J., Lonsdale, C. J., & Smith, H. E. 1992, *ApJ*, 391, 629 (LLS92)
- Lonsdale, C. J., Smith, H. E., & Lonsdale, C. J. 1993, *ApJ*, 405, L9 (Paper I)
- . 1995, *ApJ*, 438, 632 (LSL95)
- Low, F. J., Cutri, R., Kleinmann, S., & Huchra, J. 1989, *ApJ*, 340, L1
- Low, F. J., Huchra, J., Kleinmann, S. 1988, *ApJ*, 327, L41
- Mazzarella, J. M., Voit, G. M., Soifer, B. T., Matthews, K., Graham, J., Armus, L., & Shupe, D. 1994, *AJ*, 107, 1274
- Mihos, J. C., & Hernquist, L. 1996, *ApJ*, 464, 641
- Miles, J. W., Houck, J. R., & Hayward, T. L. 1994, *ApJ*, 425, L37
- Miller, J., & Scalo, J. 1979, *ApJS*, 41, 513
- Mirabel, I. F., Booth, R., Garay, G., Johansson, L., & Sanders, D. 1990, *A&A*, 236, 327
- Norman, C., & Scoville, N. 1988, *ApJ*, 332, 124
- Norris, R. P., Allen, D., Sramek, R., Kesteven, M., & Troup, E. 1990, *ApJ*, 359, 291
- Perez-Olea, D., & Colina, L. 1995, *MNRAS*, 277, 857
- Perry, J. J., & Dyson, J. E. 1985, *MNRAS*, 213, 665
- Peterson, C., & King, I. 1976, *AJ*, 80, 427
- Pier, E. A., & Krolik, J. 1992, *ApJ*, 401, 99
- . 1993, *ApJ*, 418, 673
- Polatidis, A. G., Wilkinson, P. N., Xu, W., Readhead, A. C. S., Pearson, T. J., Taylor, G. B., & Vermeulen, R. C. 1995, *ApJS*, 98, 1
- Rowan-Robinson, M. 1995, *MNRAS*, 272, 737
- Sanders, D. B., & Mirabel, I. F. 1996, *ARA&A*, 34, 749
- Sanders, D. B., Scoville, N. Z., & Soifer, B. T. 1991, *ApJ*, 370, 158
- Sanders, D. B., Soifer, B. T., Elias, J. H., Madore, B. F., Matthews, K., Neugebauer, G., & Scoville, N. Z. 1988, *ApJ*, 325, 74
- Savage B., & Mathis, J. 1979, *ARA&A*, 17, 73
- Scalo, J. 1986, *Fundam. Cosmic Phys.*, II, 1
- Schmidt, M., & Green, R. F. 1983, *ApJ*, 269, 352
- Scoville, N. Z., Sargent, A. I., Sanders, D. B., & Soifer, B. T. 1991, *ApJ*, 366, L5
- Scoville, N. Z., & Soifer, B. T. 1991, in *Massive Stars in Starbursts*, ed. C. Leitherer, N. Walborn, T. Heckman, & C. Norman (Cambridge: Cambridge Univ. Press), 233
- Scoville, N. Z., Yun, M. S., & Bryant, P. M. 1997, *ApJ*, 484, 702
- Silberman, N. A., et al. 1996, *ApJ*, 470, 1
- Smith, H. E., Lonsdale, C. J., Lonsdale, C. J., & Diamond, P. D. 1998, *ApJ*, submitted
- Soifer, B. T., Boehmer, L., Neugebauer, G., & Sanders, D. B. 1989, *AJ*, 98, 766
- Solomon, P., Downes, D., & Radford, S. 1992, *ApJ*, 387, L55
- Solomon, P., Downes, D., Radford, S., & Barrett, J. 1997, *ApJ*, 478, 144
- Spinoglio, L., & Malkan, M. 1992, *ApJ*, 399, 504
- Sturm, E., et al. 1996, *A&A*, 315, L133
- Surace, J. A., Mazzarella, J., Soifer, B. T., & Wehrle, A. 1993, *AJ*, 105, 864
- Thakkar, D. D., Xu, W., Readhead, A. C. S., Pearson, T. J., Taylor, G. B., Vermeulen, R. C., Polatidis, A. G., & Wilkinson, P. N. 1995, *ApJS*, 98, 33
- Veilleux, S., Kim, D.-C., Sanders, D. B., Mazzarella, J., & Soifer, B. T. 1995, *ApJS*, 98, 171
- Veilleux, S., & Osterbrock, D. E. 1987, *ApJS*, 63, 295
- Voit, G. M. 1992, *ApJ*, 399, 495
- Weiler, K. W., Panagia, N., & Sramek, R. 1990, *ApJ*, 364, 411
- Weiler, K. W., Sramek, R., Panagia, N., van der Hulst, J., & Salvati, M. 1986, *ApJ*, 301, 790
- Wilkinson, P. N., & de Bruyn, A. G. 1990, *MNRAS*, 242, 529
- Wilson, A. S., Helfer, T. T., Haniff, C. A., & Ward, M. 1991, *ApJ*, 381, 79
- Xu, W., Readhead, A., Pearson, T., Polatidis, A., & Wilkinson, P. 1995, *ApJS*, 99, 297
- Yin, Q. F., & Heeschen, D. S. 1991, *Nature*, 354, 130